

Georg Friedrich Harrer

**On the origin and transport of small ELMs**

**IPP 2021-03  
Januar 2021**



Technische Universität Wien

Fakultät für Physik  
Institute für Angewandte Physik  
Forschungsbereich Atom und Plasmaphysik

DISSERTATION

## On the origin and transport of small ELMs

Georg Friedrich Harrer

*1. Supervisor* Univ. Prof. Dr. Friedrich Aumayr  
Institut für Angewandte Physik  
TU Wien

*2. Supervisor* Dr. Elisabeth Wolfrum  
Max Planck Institut für Plasma Physik

June 22, 2020

**Georg Friedrich Harrer**

*On the origin and transport of small ELMs*

DISSERTATION, June 22, 2020

Supervisors: Univ. Prof. Dr. Friedrich Aumayr and Dr. Elisabeth Wolfrum

**Technische Universität Wien**

*Forschungsbereich Atom und Plasmaphysik*

Institute für Angewandte Physik

Fakultät für Physik

Wiedner Hauptstraße 8-10

1040 Wien

# Kurzfassung

Kernfusionsreaktoren könnten einen wertvollen Beitrag zum Energiesystem der Zukunft liefern. Die momentan vielversprechendste Technologie zur Erzeugung eines brennenden Fusionsplasmas ist der Tokamak. Da die nötigen Temperaturen für die Aufrechterhaltung der Fusionsreaktionen jenseits der Hundert Millionen Kelvin liegen, die Wandmaterialien jedoch unter ihrem Schmelzpunkt bleiben sollten, gibt es in Tokamaks steile Temperatur- und dadurch auch Druckgradienten. Diese Gradienten können zu magneto-hydrodynamischen Instabilitäten führen. Betreibt man Tokamaks in der sogenannten H-Mode, bildet sich am Rand des Plasmas eine Transportbarriere aus, die den Druckgradienten noch höher werden lässt. Dort lokalisierte Instabilitäten, sogenannte ELMs, führen zu einem quasi-periodischen Einbruch der Gradienten und zu großen Wärme- und Teilchenflüssen in Richtung der Gefäßwand. In zukünftigen Fusionsreaktoren könnten besonders große Typ-I ELMs somit zu Schäden an der Reaktorwand führen. Eine vielversprechende Möglichkeit dieses Problem zu umgehen stellt der Plasmabetrieb mit kleinen ELMs dar. Ziel dieser Arbeit ist die Untersuchung des Ursprungs der kleinen ELMs und die Analyse des Transports, der durch sie verursacht wird. Die ersten Kapitel beschäftigen sich mit der genauen Lokalisierung der kleinen ELMs am Fuße der Transportbarriere. Dazu werden am Tokamak ASDEX Upgrade durchgeführte Experimente gezeigt, bei denen Teilchen dem Plasma als gefrorene Deuterium-Pellets, anstatt über Gasventile zugeführt werden. Dadurch kann das Plasma effizienter befüllt und somit die Dichte im Inneren und Äußeren der Transportbarriere entkoppelt werden. Kleine ELMs und große Typ-I ELMs können gleichzeitig im Plasma vorkommen. Durch eine Formänderung des Plasmaquerschnitts kann die magnetische Verscherung des Plasmas manipuliert und die Balance zwischen beiden ELM-Typen beeinflusst werden. Dieses Verhalten deutet darauf hin, dass es sich bei Typ-I ELMs und kleinen ELMs um unterschiedliche physikalische Phänomene handelt und Letztere sich wie sogenannte Ballooning-Moden verhalten, deren Ursprung am Fuß der Transportbarriere liegt. Sie werden vom lokalen Druckgradienten angetrieben und durch die Verscherung des Magnetfelds stabilisiert. Experimente an einem weiteren Tokamak, TCV, zeigen, dass der Plasmabetrieb mit kleinen ELMs in einem weiten Parameterbereich funktioniert und unterstreichen die Wichtigkeit der äußersten Randdichte und der magnetischen Verscherung. Detaillierte Analysen, verschiedener auf den Plasma-

rand stabilisierend wirkender Mechanismen und der Vergleich mit numerischen Ballooning-Stabilitätsanalysen zeigen, dass durch die Veränderung des Plasmaquerschnitts die sogenannte *lokale* magnetische Verscherung stärker beeinflusst wird als die über den Querschnitt gemittelte Verscherung. Die Ballooning-Stabilität kann dadurch geändert und die Balance zwischen kleinen und großen ELMs gesteuert werden. Mit Hilfe fortschrittlicher Plasmadiagnostiken wurde der Fuß der Transportbarriere genau untersucht und eine Oszillation in Zeitfenstern, die von kleinen ELMs dominiert werden, gefunden. Die Frequenz dieser Oszillation ist stark mit der Dichte der Neutralteilchen im Plasmagefäß korreliert, was darauf schließen lässt, dass der Transport normal zum Magnetfeld in Phasen mit kleinen ELMs verstärkt ist. Dieser verstärkte senkrechte Transport manifestiert sich auch in einem breiteren Wärmeflussprofil am Divertor, der Komponente der Plasmawand, die den höchsten Wärme- und Teilchenflüssen ausgesetzt ist. Durch Messung der Fluktuationen in den Strömen im Divertor kann der Wärmefluss, der durch die kleinen ELMs verursacht wird, abgeschätzt werden. Diese Fluktuationsgröße steigt nur wenig wenn das Plasma stärker geheizt wird und sinkt bei höheren Frequenzen der Oszillation am Fuß der Transportbarriere. Dieses Verhalten deutet auf einen erhöhten Transport durch hochfrequente Filamente normal zur Magnetfeldrichtung hin und könnte das breitere Wärmeflussprofil am Divertor erklären. Die in dieser Arbeit erzielten Resultate dienen als Ausgangspunkt, um Plasmaentladungen mit kleinen ELMs als vielversprechendes Szenario mit quasi-kontinuierlicher Leistungsabfuhr (QCE) und gutem Plasmaeinschluss für zukünftige Fusionsreaktoren zu etablieren.

# Abstract

Nuclear fusion reactors are promising contenders for changing the energy system of the future. Currently, the most tested design for generating a burning fusion plasma is the Tokamak. Since the temperatures required to maintain the fusion reactions are beyond one hundred million Kelvin, but the wall materials should remain below their melting point, there are steep temperature and therefore pressure gradients in Tokamaks. These gradients can lead to magneto-hydrodynamic instabilities. If Tokamaks are operated in the so-called H-mode, a transport barrier forms at the edge of the plasma which in turn causes the pressure gradient to become even higher. Instabilities localized there, called ELMs, lead to a quasi-periodic collapse of the gradients and to large heat and particle fluxes in the direction of the vessel wall. In future fusion reactors, large type-I ELMs in particular could thus cause damage to the reactor wall. A promising method of circumventing this problem is plasma operation with small ELMs. The aim of this work is to investigate the origin of small ELMs and to analyze the transport caused by them. The first chapters deal with the exact location of the small ELMs at the foot of the transport barrier. Experiments carried out at the ASDEX Upgrade Tokamak are shown, in which the plasma fueling mechanism was changed from gas valves to frozen deuterium pellets. This allows the plasma to be fueled more efficiently, thus decoupling the density inside and outside the transport barrier. Small ELMs and large type-I ELMs can occur simultaneously in the plasma. Changing the shape of the plasma cross-section can alter the magnetic shear of the plasma and influence the balance between the two types of ELMs. This behavior suggests that type-I ELMs and small ELMs are different physical phenomena and that the latter behave like ballooning modes whose origin is at the foot of the transport barrier. They are driven by the local pressure gradient and stabilized by the shear of the magnetic field. Experiments on a second Tokamak, namely TCV, show that plasma operation with small ELMs works in a wide parameter range and underline the importance of the outermost boundary density and magnetic shear. Detailed analyses of various stabilizing mechanisms of the plasma edge as well as the comparison with numerical ballooning stability calculations show that the variation of the plasma cross section primarily changes the so-called *local* magnetic shear and therefore influences the small ELM ballooning stability. Using advanced plasma diagnostics, the foot of the transport barrier was examined in detail and an oscillation was found in time windows dominated by

small ELMs. The frequency of this oscillation is strongly correlated with the density of the neutral particles in the plasma vessel suggesting that transport perpendicular to the magnetic field is enhanced in phases with small ELMs. This increased vertical transport also manifests itself in a broader heat-flux profile at the divertor, the component of the plasma wall that is exposed to the highest heat and particle fluxes. By measuring the fluctuations of currents in the divertor, the heat-flux caused by the small ELMs can be estimated. This fluctuation increases only slightly when the plasma is heated more and decreases at higher frequencies of oscillation at the foot of the transport barrier. This behavior indicates increased transport through high frequency filaments perpendicular to the magnetic field direction and could explain the wider heat-flux profile at the divertor. The results obtained in this work lay the foundation for small ELMs as a promising scenario with quasi-continuous exhaust (QCE) and good plasma confinement for future fusion reactors.

# Collected Works

*Parts of this thesis have already been published or are in preparation for publication.*

## Publications as first author

- **G.F. Harrer**, E. Wolfrum, M.G. Dunne, P. Manz, M. Cavedon, P.T. Lang, B. Kurzan, T. Eich, B. Labit, J. Stober, H. Meyer, M. Bernert, F.M. Laggner, F. Aumayr, the EUROfusion MST1 Team and the ASDEX Upgrade Team "Parameter dependences of small edge localized modes (ELMs)"; Nuclear Fusion **58**, 112001 (2018):  
<https://doi.org/10.1088/1741-4326/aad757>
- **G.F. Harrer**, E. Wolfrum, M.G. Dunne, P. Manz, M. Cavedon, P.T. Lang, T. Eich, B. Labit, F. Aumayr, the Eurofusion MST1 Team and the ASDEX Upgrade Team "Parameter dependence of small Edge Localized Modes"; 45<sup>th</sup> EPS Conference on Plasma Physics, Prague (2018):  
<http://ocs.ciemat.es/EPS2018PAP/pdf/P4.1030.pdf>
- **G.F. Harrer**, E. Wolfrum, M.G. Dunne, T. Eich, R. Fischer, M. Griener, P. Hennequin, A. Bock, B. Labit, P. Manz, H. Meyer, L. Radovanovic, S. Saarelma, M. Willensdorfer, F. Aumayr, the ASDEX Upgrade Team and the Eurofusion MST1 Team "The ballooning structure of small edge localized modes in AUG and TCV"; 46<sup>th</sup> EPS Conference on Plasma Physics, Milan (2019):  
<http://ocs.ciemat.es/EPS2019PAP/pdf/04.104.pdf>

## Publications as co author

- G. Birkenmeier, J. Galdon-Quiroga, V. Olevskaia, M.G. Dunne, J.F. Rivero-Rodriguez, M. Garcia-Munoz, M. Griener, **G.F. Harrer**, N. Leuthold, E. Wolfrum, and the ASDEX Upgrade Team  
"Requirements for an Imaging Heavy Ion Beam Probe at ASDEX Upgrade";  
45<sup>th</sup> EPS Conference on Plasma Physics, Prague (2018):  
<http://ocs.ciemat.es/EPS2018PAP/pdf/P4.1020.pdf>
- A.F. Mink, E. Wolfrum, M. Hoelzl, M.G. Dunne, M. Maraschek, M. Cavedon, E. Trier, **G.F. Harrer**, B. Vanovac, A. Cathey, U. Stroth and the ASDEX Upgrade Team  
"Scaling of ELM Crash Parameters";  
45<sup>th</sup> EPS Conference on Plasma Physics, Prague (2018):  
<https://matthias-hoelzl.org/2018-07-EPS-Mink-paper.pdf>
- E. Trier, P. Hennequin, J.R. Pinzón, M. Hoelzl, G.D. Conway, T. Happel, **G.F. Harrer**, F. Mink, F. Orain, E. Wolfrum, the ASDEX Upgrade Team and the EUROfusion MST1 Team  
"Studying ELM filaments with Doppler reflectometry in ASDEX Upgrade";  
45<sup>th</sup> EPS Conference on Plasma Physics, Prague (2018):  
<http://ocs.ciemat.es/EPS2018PAP/pdf/P1.1023.pdf>
- B. Vanovac, E. Wolfrum, M. Willensdorfer, M. Griener, A.F. Mink, **G.F. Harrer**, M. Hoelzl, and the ASDEX Upgrade Team  
"Parameter space of low frequency inter-ELM modes";  
45<sup>th</sup> EPS Conference on Plasma Physics, Prague (2018):  
<https://matthias-hoelzl.org/2018-07-EPS-Vanovac-paper.pdf>
- B. Vanovac, E. Wolfrum, M. Hoelzl, M. Willensdorfer, M. Cavedon, **G.F. Harrer**, F. Mink, S.S. Denk, S. Freethy, M.G. Dunne, P. Manz, N.C. Luhmann Jr. and the ASDEX Upgrade Team  
"Characterization of low frequency inter-ELM modes at the pedestal top of H-mode discharges at ASDEX Upgrade";  
Nuclear Fusion **58**, 112011 (2018):  
<https://iopscience.iop.org/article/10.1088/1741-4326/aada20/pdf>

- A.F. Mink, E. Wolfrum, M.G. Dunne, M. Hoelzl, M. Maraschek, R. Fischer, M. Cavedon, **G.F. Harrer**, U. Stroth and the ASDEX Upgrade Team  
"Scaling of the toroidal structure and nonlinear dynamics of ELMs on ASDEX Upgrade";  
Plasma Physics and Controlled Fusion **60**, 125011 (2018):  
<https://iopscience.iop.org/article/10.1088/1361-6587/aae33a/pdf>
- B. Labit, H. De Olivera, R. Maurizio, A. Merle, U. Sheikh, P. Molina Cabrera, T. Eich, E. Wolfrum, M. Bernert, J. Stober, M.G. Dunne, **G.F. Harrer**, H. Meyer, L. Frassinetti, P. Hennequin, S. Saarelma, the TCV Team, the AUG Team and the MST1 EUROfusion Team  
"Plasma shape and fueling dependence on the small ELMs regime in TCV and AUG";  
27<sup>th</sup> IAEA Fusion Energy Conference, Gandhinagar (2018):  
<https://bit.ly/31331p5>
- F.M. Laggner, E. Kolemen, A. Diallo, R.J. Groebner, E. Wolfrum, K.K. Barada, M. Cavedon, B.A. Grierson, **G.F. Harrer**, F. Mink, T.H. Osborne, P.B. Snyder, the ASDEX Upgrade Team and the DIII-D Team  
"The Universality of Inter-ELM Pedestal Fluctuations in AUG and DIII-D: Impacting the Edge Profile Structure by Clamping of the Gradients";  
27<sup>th</sup> IAEA Fusion Energy Conference, Gandhinagar (2018):  
<https://bit.ly/312G86q>
- E. Viezzer, M. Cavedon, E. Fable, F.M. Laggner, R.M. McDermott, A. Kappatou, C. Angioni, P. Cano-Megias, D. Cruz-Zabala, R. Dux, **G.F. Harrer**, U. Plank, T. Pütterich, F. Ryter, E. Wolfrum, the ASDEX Upgrade Team and the EUROfusion MST1 Team  
"ELM-Induced Energy and Momentum Transport in ASDEX-Upgrade";  
27<sup>th</sup> IAEA Fusion Energy Conference, Gandhinagar (2018):  
<https://bit.ly/3hQjPXX>
- B. Labit for the EUROfusion MST1 Team including **G.F. Harrer**  
"Dependence on plasma shape and plasma fueling for small ELM regimes in TCV and ASDEX Upgrade";  
Nuclear Fusion **59**, 086020 (2019):  
<https://iopscience.iop.org/article/10.1088/1741-4326/ab2211>

- H. Meyer for the ASDEX Upgrade Team including **G.F. Harrer**  
"Overview of physics studies on ASDEX Upgrade";  
Nuclear Fusion **59**, 112014 (2019):  
<https://iopscience.iop.org/article/10.1088/1741-4326/ab18b8/meta>
- S. Coda for the TCV Team including **G.F. Harrer**  
"Physics research on the TCV tokamak facility: from conventional to alternative scenarios and beyond";  
Nuclear Fusion **59**, 112023 (2019):  
<https://iopscience.iop.org/article/10.1088/1741-4326/ab25cb/meta>
- M. Cavedon, R. Dux, T. Pütterich, E. Viezzer, E. Wolfrum, M.G. Dunne, E. Fable, R. Fischer, **G.F. Harrer**, F.M. Laggner, A.F. Mink, U. Plank, U. Stroth, M. Willensdorfer, ASDEX Upgrade Team  
"On the ion and electron temperature recovery after the ELM-crash at ASDEX Upgrade";  
Nuclear Materials and Energy **18**, 275-280 (2019):  
<https://www.sciencedirect.com/science/article/pii/S2352179118302114>
- E. Viezzer, M. Cavedon, P. Cano-Megias, E. Fable, E. Wolfrum, D.J. Cruz-Zabala, P. David, R. Dux, R. Fischer, **G.F. Harrer**, F.M. Laggner, R.M. McDermott, U. Plank, T. Pütterich, M. Willensdorfer  
"Dynamics of the pedestal transport during edge localized mode cycles at ASDEX Upgrade";  
Plasma Physics and Controlled Fusion **62**, 024009 (2019):  
<https://iopscience.iop.org/article/10.1088/1361-6587/ab5b1d/pdf>

## Conference, workshop and public outreach contributions

### Oral contributions

- **G.F. Harrer**, E. Wolfrum, F. Aumayr, the ASDEX Upgrade Team and the EURO-fusion MST1 Team  
"Origin and Transport of small Edge Localized Modes";  
HEPP Seminar, Garching (2017)

- **G.F. Harrer**  
"Herausforderungen in der Kernfusionsforschung";  
Physik im Beisl - Österreichs Physik Nachwuchs erklärt die Welt, Wien (2018)
- **G.F. Harrer**, M. Werl, E. Wolfrum, L. Giannone, K.H. Schuhbeck, T. Lunt  
"Scaling of divertor current signals for type-I ELMs";  
E2M - Programme Seminar, Kreuth (2018)
- **G.F. Harrer**  
"Stars Inside Donuts";  
2<sup>nd</sup> Munich Science Slam, Munich (2018):  
<https://youtu.be/8vZ5TnzMcYo?t=17>
- **G.F. Harrer**, E. Wolfrum, M.G. Dunne, M. Werl, F. Aumayr  
"Small Edge Localized Modes, a ballooning description";  
AUG - Programme Seminar, Kreuth (2018)
- **G.F. Harrer**, E. Wolfrum, M.G. Dunne, M. Werl, L. Radovanovic, F. Aumayr  
"Small Edge Localized Modes, a ballooning description";  
HEPP Seminar, Remote Talk, Wien / Garching (2019)
- **G.F. Harrer**, E. Wolfrum, M.G. Dunne, T. Eich, M. Griener, P. Hennequin, B. Labit, P. Manz, L. Radovanovic, F. Aumayr, the ASDEX Upgrade Team and the EUROfusion MST1 Team  
"A ballooning mode description of small ELMs";  
DPG-Frühjahrstagung der Sektion Materie und Kosmos (SMuK), Munich (2019)
- **G.F. Harrer**, E. Wolfrum, M.G. Dunne, R. Fischer, A. Bock, T. Eich, F. Aumayr, the ASDEX Upgrade Team and the EUROfusion MST1 Team  
"Access to small ELM regimes";  
E2M Program Seminar, Kreuth (2019)
- **G.F. Harrer**, E. Wolfrum, M.G. Dunne, T. Eich, R. Fischer, M. Griener, P. Hennequin, A. Bock, B. Labit, P. Manz, H. Meyer, L. Radovanovic, S. Saarelma, M. Willensdorfer, F. Aumayr, the ASDEX Upgrade Team and the Eurofusion MST1 Team  
"The ballooning structure of small edge localized modes in AUG and TCV";  
46<sup>th</sup> EPS Conference on Plasma Physics, Milan (2019)

- **G.F. Harrer**, E. Wolfrum, M. Griener, M. Faitsch, M.G. Dunne, P. David, T. Eich, R. Fischer, P. Hennequin, A. Bock, B. Labit, P. Manz, L. Radovanovic, F. Aumayr, the ASDEX Upgrade Team and the EUROfusion MST1 Team  
"On the effect of heating and fuelling on small ELM regimes";  
17<sup>th</sup> International Workshop on H-mode Physics and Transport Barriers, Shanghai (2019)
- **G.F. Harrer**, E. Wolfrum, M.G. Dunne, T. Eich, M. Griener, P. Hennequin, B. Labit, P. Manz, L. Radovanovic, F. Aumayr, the ASDEX Upgrade Team and the EUROfusion MST1 Team  
"Small ELMs – a promising reactor scenario";  
Seminar for Applied Physics, Wien (2019)
- **G.F. Harrer**, E. Wolfrum, M. Griener, M. Faitsch, M.G. Dunne, P. David, T. Eich, R. Fischer, P. Hennequin, A. Bock, B. Labit, P. Manz, L. Radovanovic, F. Aumayr, the ASDEX Upgrade Team, and the EUROfusion MST1 Team  
"Small ELM scenarios at AUG and TCV";  
Fusionstag OEAW, Salzburg (2019)
- **G.F. Harrer** and M. Faitsch, for the MST1 HLT-05 Team  
"Validation of high-density small ELM regimes for ITER & DEMO";  
MST1 Review and Planning Meeting, Garching (2020)

## Posters

- **G.F. Harrer**, E. Wolfrum, P. Manz, F. Mink, F.M. Laggner, F. Aumayr and the ASDEX Upgrade Team  
"Search for experimental evidence of mode coupling during the ELM cycle from magnetic measurements in ASDEX Upgrade";  
DPG-Frühjahrstagung der Sektion Materie und Kosmos (SMuK), Bremen (2017)
- **G.F. Harrer**, E. Wolfrum, J. Stober, O. Sauter, P. Lang, G. Birkenmeier, B. Kurzan, R. Fischer, H. Meyer, F.M. Laggner, F. Mink, F. Aumayr, the ASDEX Upgrade Team and the EUROfusion MST1 Team  
"Dependence of small Edge Localized Modes on Plasma Parameters";  
16<sup>th</sup> International Workshop on H-mode Physics and Transport Barriers, St. Petersburg (2017)

- **G.F. Harrer**, E. Wolfrum, T. Eich, M.G. Dunne, P. Manz, P.T. Lang, B. Kurzan, H. Meyer, M. Bernert, B. Labit, G. Birkenmeier, J. Stober, F. Aumayr, the ASDEX Upgrade Team and the EUROfusion MST1 Team  
"Dependence of small Edge Localized Modes (ELMs) on Plasma Parameters"; DPG-Frühjahrstagung der Sektion Atome, Moleküle, Quantenoptik und Plasmen (SAMOP), Erlangen (2018)
- **G.F. Harrer**, E. Wolfrum, M.G. Dunne, P. Manz, M. Cavedon, P.T. Lang, B. Kurzan, T. Eich, B. Labit, F. Aumayr, the ASDEX Upgrade Team and the EUROfusion MST1 Team  
"Parameter dependence of small ELMs"; 45<sup>th</sup> EPS Conference on Plasma Physics, Prague (2018)
- **G.F. Harrer**, E. Wolfrum, M.G. Dunne, P. Manz, M. Cavedon, P.T. Lang, B. Kurzan, T. Eich, B. Labit, F. Aumayr, the ASDEX Upgrade Team and the EUROfusion MST1 Team  
"Parameter dependence of small ELMs"; FuseNet PHD Event, Cadarache (2018)
- **G.F. Harrer**, E. Wolfrum, M. Griener, M. Faitsch, M.G. Dunne, P. David, T. Eich, R. Fischer, P. Hennequin, A. Bock, B. Labit, P. Manz, L. Radovanovic, F. Aumayr, the ASDEX Upgrade Team and the EUROfusion MST1 Team  
"On the effect of heating and fuelling on small ELM regimes"; 17<sup>th</sup> International Workshop on H-mode Physics and Transport Barriers, Shanghai (2019)

## Co-supervised Student Theses

- M. Werl  
"Correlating outer divertor current Ipolsola to energy loss during ELMs in ASDEX Upgrade"; TU Wien Project Thesis, (2018)
- S. Haberfellner  
"Statistical analysis of midplane measurements and divertor current signals"; TU Wien Project Thesis, (2018)
- L. Radovanovic  
"Local ballooning stability analysis with the code HELENA"; TU Wien Project Thesis, (2019)

- L. Radovanovic  
"Ballooning stability of small ELM regimes";  
TU Wien Master Thesis, (2020) *in writing*

# Contents

<b>1</b>	<b>Introduction</b>	<b>1</b>
1.1	Energy . . . . .	1
1.1.1	World Energy Supply and Consumption . . . . .	1
1.1.2	CO2 and Climate Change . . . . .	3
1.1.3	Renewable Energies and Storage . . . . .	4
1.2	Nuclear Fusion . . . . .	6
1.2.1	Magnetic Confinement . . . . .	7
1.2.2	H-mode and ELMs . . . . .	9
1.2.3	Power Exhaust and small ELM Scenarios . . . . .	10
1.3	Thesis Objectives and Structure . . . . .	14
<b>2</b>	<b>Basic Experimental Tokamak Physics</b>	<b>17</b>
2.1	AUG and TCV . . . . .	17
2.1.1	ASDEX Upgrade . . . . .	18
2.1.2	Tokamak à Configuration Variable . . . . .	19
2.2	Heating . . . . .	19
2.3	Fueling and Seeding . . . . .	22
2.4	Plasma Shaping . . . . .	24
2.5	Advanced Plasma Diagnostics . . . . .	26
2.5.1	Kinetic Profiles . . . . .	26
2.5.2	ELM Monitors . . . . .	32
2.5.3	Heat and Particle Loads . . . . .	34
2.5.4	Burst and Filament Characteristics . . . . .	36
2.5.5	Plasma Equilibrium Reconstruction . . . . .	37
2.6	MHD Modes and ELM Modelling . . . . .	40
2.6.1	Pressure Gradient driven Instabilities . . . . .	41
2.6.2	Ballooning Modes . . . . .	42
2.6.3	Current driven Instabilities . . . . .	44
2.6.4	Peeling-Ballooning Modes . . . . .	44
2.6.5	Linear Stability Analysis . . . . .	46
2.6.6	Nonlinear Modeling with JOREK . . . . .	47

<b>3</b>	<b>Significance of the Separatrix</b>	<b>49</b>
3.1	Introduction . . . . .	49
3.2	Experiments and Simulations . . . . .	51
3.2.1	Influencing the Separatrix Density . . . . .	51
3.2.2	Predictive Modeling . . . . .	55
3.3	Chapter Summary . . . . .	57
<b>4</b>	<b>Ballooning Model</b>	<b>59</b>
4.1	Plasma Shape Changes: The $z$ -shift . . . . .	59
4.2	Peeling-Ballooning Stability in small ELM Regimes . . . . .	62
4.3	Influence of the magnetic Shear close to the Separatrix . . . . .	63
4.4	Schematic small ELM Model . . . . .	64
4.5	Chapter Summary . . . . .	67
<b>5</b>	<b>Small ELM Studies in TCV</b>	<b>69</b>
5.1	The ITER Baseline Scenario and small ELMs . . . . .	69
5.2	Gas Fueling Scan in ELMy H-mode . . . . .	71
5.3	The high Triangularity small ELM Regime at TCV . . . . .	73
5.4	Physical Interpretation . . . . .	76
5.5	Chapter Summary . . . . .	78
<b>6</b>	<b>Stabilizing Effects in small ELM Scenarios</b>	<b>81</b>
6.1	Modulation of the Plasma Current . . . . .	81
6.2	The $z$ -shift at different Safety Factors . . . . .	84
6.3	The stabilizing Effect of the Local magnetic Shear . . . . .	89
6.4	The Role of the Electric Field . . . . .	92
6.5	The Connection between HFS and LFS . . . . .	95
6.6	Chapter Summary . . . . .	95
<b>7</b>	<b>Small ELM Bursts and Filaments</b>	<b>99</b>
7.1	Burst Determination and Location . . . . .	99
7.2	Parameter Dependence of the Burst Frequency . . . . .	102
7.3	Impact on the Divertor . . . . .	104
7.4	Parameter Dependence of the small ELM Size . . . . .	107
7.5	Chapter Summary . . . . .	109
<b>8</b>	<b>Summary and Conclusion</b>	<b>111</b>
8.1	Summary . . . . .	111
8.2	Small ELMs as a Reactor Scenario . . . . .	113
8.3	Ideas for Future Research . . . . .	114

<b>Bibliography</b>	<b>119</b>
<b>Declaration</b>	<b>133</b>



” *Energy is like oxygen for life.*

— **Bernard Bigot**

ITER Organization Director-General

This chapter will give a brief overview of the world energy system and some insights on climate change and energy storage as a motivation for the reader to learn about nuclear fusion as an additional energy source. The chapter will conclude with some open challenges in fusion research and will give an outlook on the chapters to come, providing a scope for this work.

## 1.1 Energy

Human development is strongly correlated with the access to energy<sup>1</sup>. With a growing population and an increase in the quality of life worldwide, humanity’s consumption of energy is ever-increasing. Additionally, to fight climate change, virtually all the world’s countries have agreed to reduce greenhouse gas emissions by a substantial amount [1]. To meet the high energy demand while decreasing emissions, the whole energy sector needs to transition to net carbon-free or renewable sources.

### 1.1.1 World Energy Supply and Consumption

Humanity’s increasing energy consumption has historically always been satisfied by the exploitation of new energy sources. Figure 1.1(a) shows the world’s primary energy consumption categorized in different energy sources, from 1850 to 2018, measured in TWh per year. Primary energy is every energy form found in nature that has not been subjected to any humanly engineered conversion process. It is energy contained in raw fuels and other forms of energy received as input to

---

<sup>1</sup>Energy is the ability to do work or produce heat.

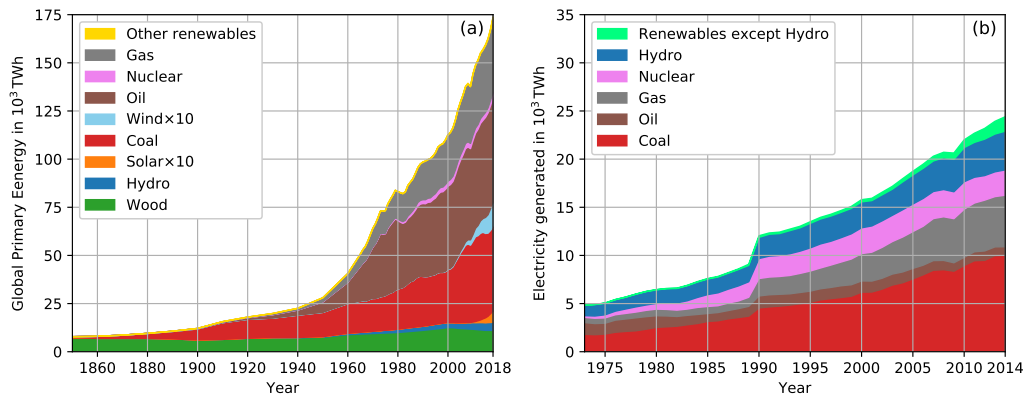


**Fig. 1.1:** Energy Production: (a) global primary energy production by source (data from [2]),(b) electrical energy production (data from [3]).

a system. Dominated by traditional bio-fuels (mostly firewood, green) [2018: 7%] in the 19th century, the biggest players rapidly became the fossil fuels: coal (red)[27.9%] oil (brown)[34.5%] and gas (grey)[24.5%]. A small part of world energy consumption nowadays is also met by hydro-power (blue)[2.7%] and nuclear fission (violet)[1.7%]. The rest is split up into the so-called modern renewables wind (light blue)[0.8%], solar (orange)[0.4%]<sup>2</sup> and other renewable sources such as geothermal or tidal power (yellow)[0.4%].

This total primary energy consumption can be compared with the electricity produced worldwide, figure 1.1(b). Here the major part is still fossil fuel based, but the share of hydro and nuclear power increases, as these two sources are mostly used for electricity production. In total, the electrical energy produced, only accounts for around 1/7<sup>th</sup> of world energy consumption. Where does the rest of the energy go?

The international energy agency categorizes consumed primary energy in different sectors [4] from largest to smallest: Industry [2017:29%], Transport [29%], Residential (mostly heating)[29%], Electricity [19%], Non-energy use [9%]<sup>3</sup>, Commercial and public services [8%], Agriculture and forestry[2%] and unspecified[2%].

All of these sectors rely strongly on burning fossil fuels with a high carbon content. Industry, for example, is dominated by furnaces for steel production using enormous amounts of coal. The transport sector relies mostly on crude oil that is refined into diesel, petrol or kerosene and the majority of home heating worldwide is still done by burning natural gas, coal and oil.

<sup>2</sup>Wind and solar are enhanced in the graph by a factor of 10 for better visibility

<sup>3</sup>Non-energy use covers use of other petroleum products such as white spirit, paraffin waxes, lubricants, bitumen and other products.

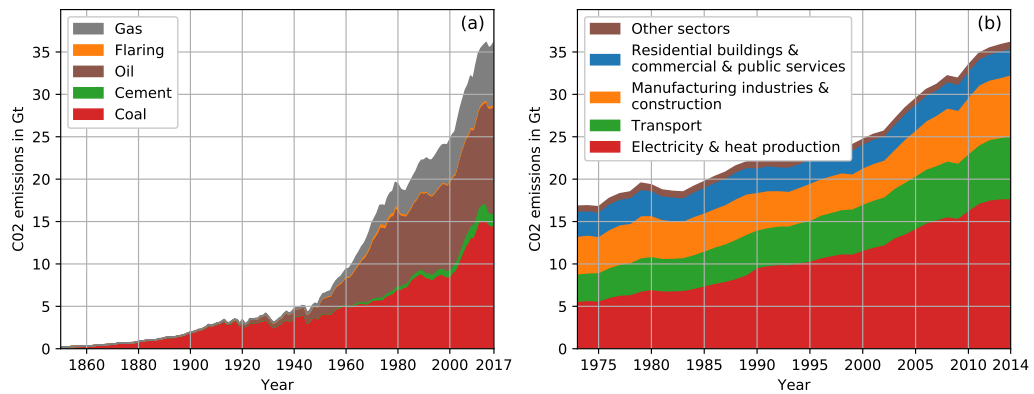


**Fig. 1.2:** Global CO<sub>2</sub> emission in Gt grouped by (a) source (data from [5]) and (b) sector (data from [3]).

### 1.1.2 CO<sub>2</sub> and Climate Change

Using all this carbon stored in the earth's crust over millennia and releasing larger and larger amounts of it in the form CO<sub>2</sub> into the atmosphere has been leading to an ever increasing atmospheric concentration of this gas. CO<sub>2</sub> in the atmosphere acts as a so-called greenhouse gas, reflecting the thermal radiation coming from the earth's surface, therefore leading to a higher temperature of the surface of the earth.

The increasing global emissions are shown in figure 1.2 in two different ways. Figure 1.2 (a) shows the source of the emissions, again from 1850 to recent times. The main players were already identified in the previous section. A small contribution to the emissions also comes from the cement industry [2017: 4%] and the controlled burning of residual natural gas in the oil extraction process called flaring [1%]. It is remarkable how similar the historical trend of the CO<sub>2</sub> emissions (1.2 (a)) is to global primary energy consumption (1.1 (a)). The CO<sub>2</sub> emissions divided into the energy sectors are shown in figure 1.2 (b). Here the largest part, electricity and heat, also includes industrial heat production e.g. blast furnaces for iron and steel production. The rest splits up into the oil dominated transport industry, manufacturing and construction and residential and commercial services.

The similarity of figures 1.2 (a) and 1.1 (a) is a clear indication that the increasing consumption of energy leads to higher CO<sub>2</sub> emissions. In turn, this led to an anthropological<sup>4</sup> increase of the CO<sub>2</sub> concentration in the atmosphere (over 30% in the last 60 years where before it had only changed by about 5% in the last 10,000

<sup>4</sup>caused by humans

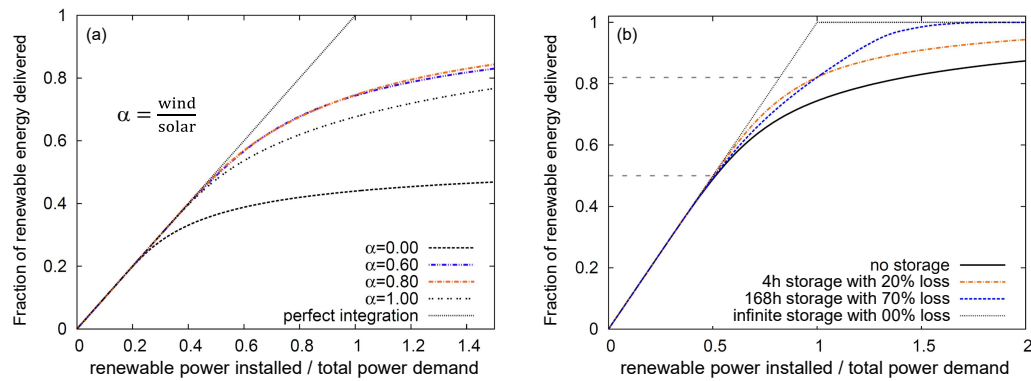


**Fig. 1.3:** Renewable energy integration to the power grid: (a) variation of the wind to solar ratio and (b) combination of 60 % wind to solar ratio with energy storage of different sizes and efficiencies [7].

years [6]). Due to the greenhouse effect, this causes a higher temperature and changes to the global climate system.

To mitigate the effects of this climate change, 194 countries have joined forces and agreed on a common goal to keep the global temperature increase well below 2°C [1] each country following its national plan. The EU, for example, has agreed to reduce its greenhouse gas emissions by at least 40 % by 2030 (compared to 1990).

What this means for the energy sector is a need to switch to net carbon free renewable sources wherever possible. The main strategy is to increase the photovoltaic and wind energy capacity exponentially as the potential for hydro-power is limited. The feasibility of this idea is discussed in the next section.

### 1.1.3 Renewable Energies and Storage

Figure 1.3 shows the results of a study [7] investigating modern renewable energy (wind + solar) integration into the German electricity grid without (a) and with storage (b). This was done by looking at meteorological data and the temporal evolution of German electricity consumption in order to study intermittency and curtailment of renewables. In an electrical power grid, supply and demand always have to match. That means that if the installed renewable energy is high and there is low demand, solar plants or wind turbines have to be switched off. This is called "curtailment due to overproduction" and is not desirable. Both plots of figure 1.3 show the fraction of electricity delivered by modern renewables in relation to the renewable integration factor, i.e., how much renewable power is installed in the grid normalized to the power demand. For perfect integration, this graph is a straight

line from (0,0) to (1,1). The wind does not always blow at the desired speed and the sun does not shine 24 h a day. This makes wind and solar power very intermittent. Figure 1.3 (a) shows a variation of the factor of wind to photovoltaic energy. Here the best results are achieved with a mix of wind and solar power, where both 60 % and 80 % wind give similar results. The two extreme cases, wind and solar only, show lower renewable coverage. It is worth noting that even the best cases can only deliver 80 % of the electricity from renewables with 140 % renewable power installed. To counteract the intermittency, figure 1.3 (b) shows the same plot for a wind to solar ratio of 60 % with the addition of different energy storage solutions. Infinite storage with 0 % loss is equivalent to the perfect integration line in figure 1.3 (a). The other two cases are taken as examples of faster storage with fewer losses such as pumped storage or batteries (orange) and bigger capacity higher loss solutions such as power to gas. The capacities of the storages considered here are quite optimistic, with one being able to cover the average demand for 4 h (200 GWh) and the other for 168 h, i.e., one week (9100 GWh). As a comparison, the study mentions the capacity for pumped storage in Germany to be 39 GWh. Even with such enormous storage solutions, 100 % renewable energy coverage is only possible when installing 160 % of the power demand for the seasonal storage (blue) while 200 % of installed renewables is needed with the 4 h storage to achieve approx. 95 % renewable fraction.

The transition to a carbon free electricity system is far from solved. In the above cited study additional effects e.g. the electricity sector taking over massive parts of other energy sectors, or the area usage that would be needed to install so much renewable capacity, are not considered. A net carbon free energy system using only wind and solar power is therefore very unlikely to materialize and traditional power plants up to very high renewable integration factors of 1.5 would still be needed to deliver base load.

From a physics point of view, the highest potential for energy generation<sup>5</sup> lies in the binding energy of atomic nuclei. Nuclear reactions release energies on the order of millions of eV compared to only several eV in chemical reactions e.g. the burning of traditional fuels. This can be understood by looking at the binding energy of the most common isotopes in figure 1.4. The most tightly bound atomic nuclides exist at mass numbers of 55 – 65. Considering the mass energy equivalent, energy can be gained by fusing light nuclei such as hydrogen or by the fission of heavy nuclei such as uranium.

---

<sup>5</sup>omitting matter-antimatter annihilation

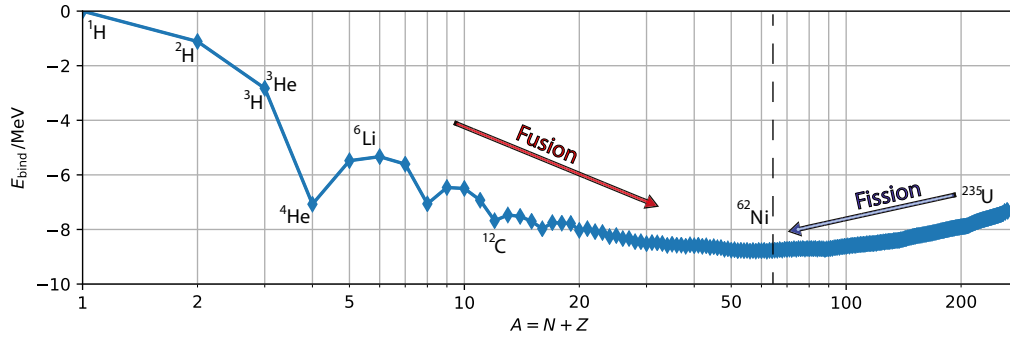


**Fig. 1.4:** Binding Energy per nucleon over atomic mass number reproduced from [8]. Energy can be gained by the fusion of light or the splitting of heavy nuclei.

Nuclear fission reactors are an already proven technology that could deliver carbon free base load. Their main disadvantages are that they are built on controlling a run-away chain reaction and they produce highly radioactive waste. Due to several serious accidents, nuclear fission has lost its popular appeal. A detailed discussion of the feasibility of nuclear fission has been omitted here as it would go beyond the scope of this work.

This leads us to the main topic of this thesis.

## 1.2 Nuclear Fusion

Nuclear fusion is the process that powers the sun and the stars. In the case of stars, fusion takes place in the so-called proton-proton chain reaction where in total four protons, via several reactions, fuse to one He nucleus while releasing energy in the form of photons. For these reactions, very high pressures and temperatures on the order of  $\sim 100 \times 10^6$  K or energies in the keV range are necessary. This high pressure is achieved in the core of stars by gravitational forces due to their very high mass. These high gravitational forces fortunately do not exist on earth and therefore other concepts are necessary in order to confine the reactants for fusion to occur.

There are two main concepts used to reproduce nuclear fusion on earth: inertial confinement fusion, where hydrogen fuel pellets are compressed with extremely powerful lasers and magnetic confinement fusion where the goal is to trap the high energetic reactants with magnetic fields. This thesis will focus on the latter technique.

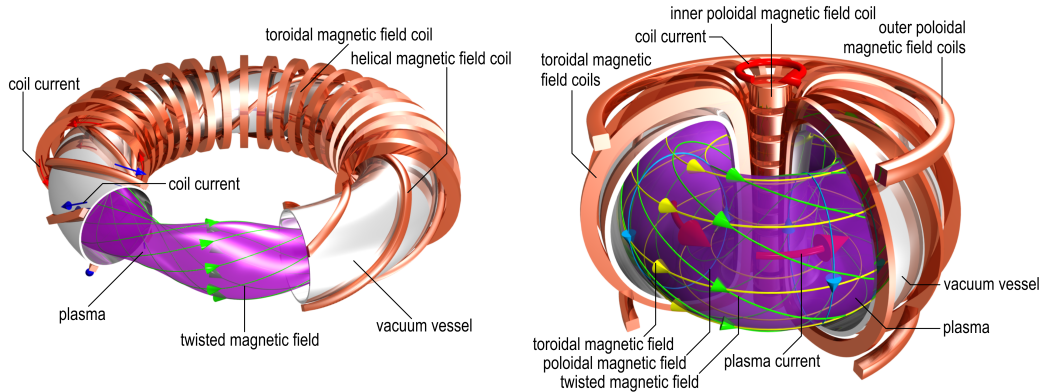


**Fig. 1.5:** Main components of stellarators and tokamaks. The helical field is produced via external coils in the stellarator and via a plasma current induced by the central solenoid in the tokamak. Figure from Christian Brandt, IPP Greifswald.

## 1.2.1 Magnetic Confinement

At the temperatures needed to achieve fusion reactions, the kinetic energy of the reactants is so high that the fuel is in a plasma state and therefore consists of separated ions and electrons. These charged particles can be trapped to gyrate around magnetic field lines according to the Lorentz force. To avoid end losses it is suitable to bend these field lines to a circle. This explains the toroidal shape of most recent magnetic confinement machines. To achieve particle confinement a toroidal magnetic field  $B_\phi$  alone is not enough as the field strength decreases radially outward. This would, via charge separation of electrons and ions, create electric fields which in turn would push the particles to the outside wall. To counteract this effect, the field lines need to be bent around the torus to a helical shape.

That can be done either by using external coils or by inducing a current in the plasma that then creates an extra poloidal field  $B_\theta$ . These two different concepts are the main areas of magnetic confinement research and are called the stellarator and the tokamak. The main components of these machines are displayed in figure 1.5.

The p-p reaction chain as it occurs in the sun is not the most efficient fusion reaction by a long way. Figure 1.6 (a) shows the cross sections of four different fusion reactions. At 20 keV ion temperature the deuterium-tritium reaction is 50 times more likely to happen than the deuterium-deuterium reaction and 1000 times more likely than the deuterium- $^3\text{He}$  reaction. Only at temperatures above 200 keV does the  $^3\text{He}$  reaction become interesting.

The rate of fusion energy produced by the plasma can be estimated by multiplying the densities of the two reactants with the energy per reaction and the reactivity i.e.,

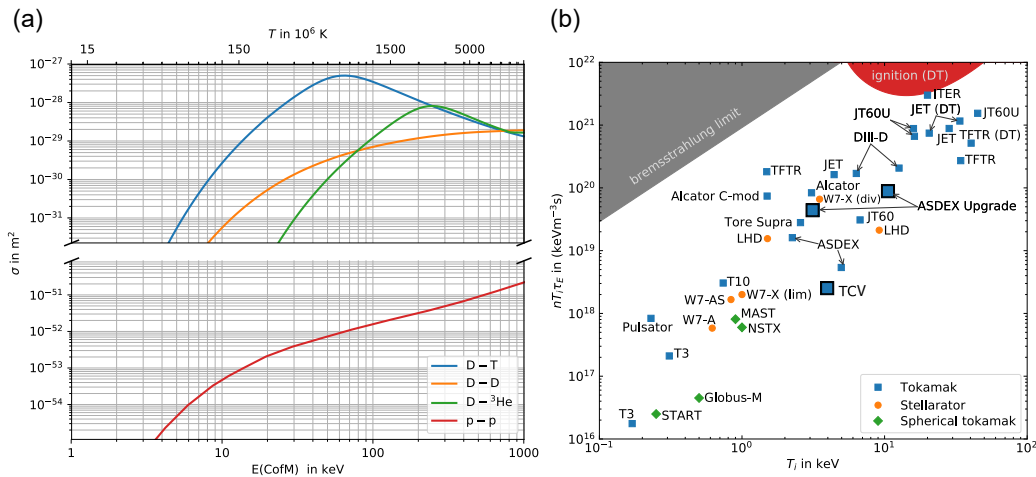


**Fig. 1.6:** (a) Cross section of fusion reactions over center of mass energy of the reactants (b) the fusion triple product density, ion temperature and energy confinement time is plotted for various fusion tokamaks and stellarators, over the respective ion temperature [10, 11].

the average over the distributions of reaction cross section times relative reactant velocity. The point of ignition<sup>6</sup> can be derived by including radiative and conductive losses via the so-called energy confinement time  $\tau_E$ <sup>7</sup>. The "burning plasma" is then self sustaining and only needs to be refueled, in a similar way to a combustion oven. This estimation was first done by John D. Lawson [9] and is therefore known as the Lawson criterion. It can be extended to the so-called fusion triple-product of density  $n$ , ion temperature  $T$  and energy confinement time  $\tau_E$ ,  $n \times T \times \tau_E$  which is a more useful figure of merit, as most machines can achieve high density at low temperatures and high temperature at low densities and are actually limited by the achievable pressure  $p = n \times T$ . Figure 1.6 (b) shows this triple product for multiple magnetic confinement machines. Stellarators are represented by orange dots, tokamaks by blue squares and spherical tokamaks, which are tokamaks with a very low aspect ratio<sup>8</sup>, by green diamonds. Tokamaks have up to now reached higher ion temperatures and triple products and ITER, the largest tokamak under construction, is designed very close to the ignition point. The new numerically optimized stellarator Wendelstein 7-X of IPP is already reaching the values of medium sized tokamaks. For too high densities (top left), the energy the plasma loses via bremsstrahlung is too high for reaching ignition. The two tokamaks treated in this thesis, ASDEX Upgrade and TCV, are emphasized by black borders.

<sup>6</sup>the point at which density and confinement time of the plasma are high enough so that the plasma heats itself through the energy of its charged fusion products

<sup>7</sup> $\tau_E = \frac{W}{P_{\text{loss}}}$  is the time the plasma takes to cool down when external heating is stopped.

<sup>8</sup>The ratio of major to minor radius  $A = R/a$ .

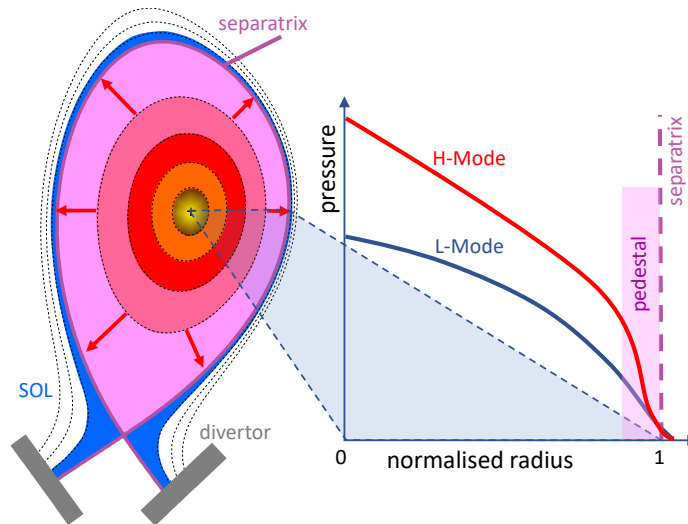


**Fig. 1.7:** Poloidal cross section of the nested flux surfaces of a divertor plasma including a comparison of radial L and H-mode pressure profiles. Definition of scrape-off layer (SOL), separatrix, divertor and pedestal.

## 1.2.2 H-mode and ELMs

Plasma densities and ion temperatures necessary for ignition have already been reached in existing devices. The only missing element is the energy confinement time. As  $\tau_E$  increases with the machine radius<sup>9</sup> future machines such as ITER, CFETR and DEMO are planned with larger radii than present day devices.

An unexpected improvement in confinement was first recognised at ASDEX in 1982 [12], where passing an input heating power threshold, the confinement times increased by a factor of two. This operational regime was called high confinement or H-mode while the operation below the power threshold was then dubbed low confinement or L-mode. Figure 1.7 shows pressure profiles of both L- and H-mode next to a cross section of an ASDEX Upgrade plasma. From the inside out one can see the nested flux surfaces visible as ellipses, with the last closed one called the separatrix. The area outside this flux surface is called the scrape-off layer (SOL) as the field lines there are no longer closed and end at the so called divertor. The divertor is designed to withstand the highest heat and particle loads of the machine. The main difference between the radial pressure profiles of the two regimes is located in a small region inside the separatrix where the H-mode pressure profile is elevated onto a so called pedestal. This pedestal forms due to an edge transport barrier which suppresses turbulent transport and leads to very high pressure gradients at

<sup>9</sup>a bigger plasma takes longer to cool off

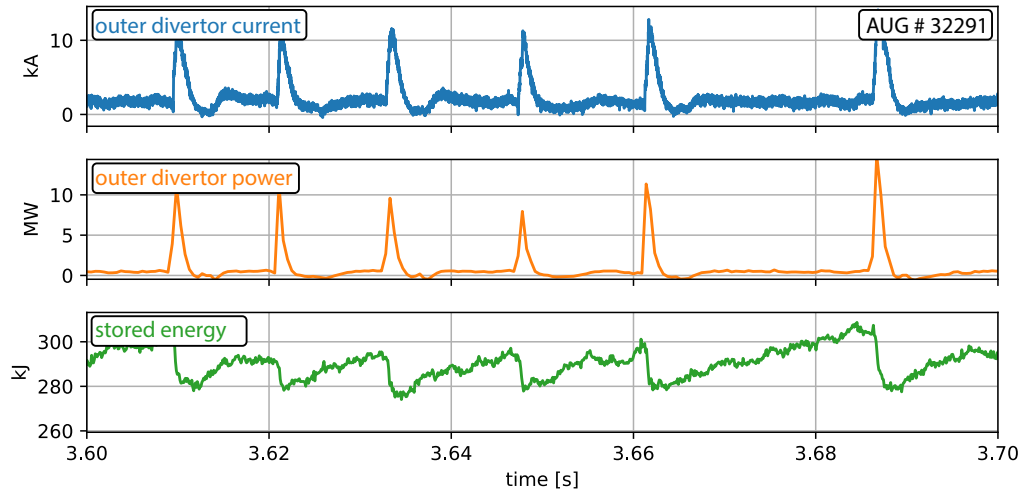


**Fig. 1.8:** Time traces of AUG H-mode discharge #32291 the divertor current from shunt measurements (blue), the total power reaching the outer divertor (orange), the total amount of energy confined in the plasma (green).

the plasma edge. These high gradients give rise to plasma instabilities which are fittingly called Edge Localised Modes short ELMs.

They crash the temperature and density pedestal and lead to a flush out of energy and particles from the plasma to the divertor and wall. Figure 1.8 shows time traces of the divertor current, which is often used as an ELM monitor on metal wall machines such as AUG, the total power reaching the outer divertor target and the plasma stored energy of a fully developed H-mode of ASDEX Upgrade. With every ELM a power of over 5 MW reaches the outer divertor and the stored energy of the plasma drops by 5 – 10 % and is successively restored after the ELM. The study of ELM physics is an important field in tokamak research and ELMs have been observed in all tokamaks that can achieve H-mode.

### 1.2.3 Power Exhaust and small ELM Scenarios

A crucial aspect for a future reactor is how to handle the power balance. To keep the fusion plasma in equilibrium, it needs to be constantly reheated and refueled in order to balance particle and energy losses due to different transport mechanisms. In steady state all energy that goes into the plasma has to come out again. This is depicted in figure 1.9(a) where the input power  $P_{\text{HEAT}}$  in addition to the power coming from fusion reactions is in balance with the power crossing the separatrix  $P_{\text{sep}}$ . This power (without neutrons and radiation) is deposited in a narrow region

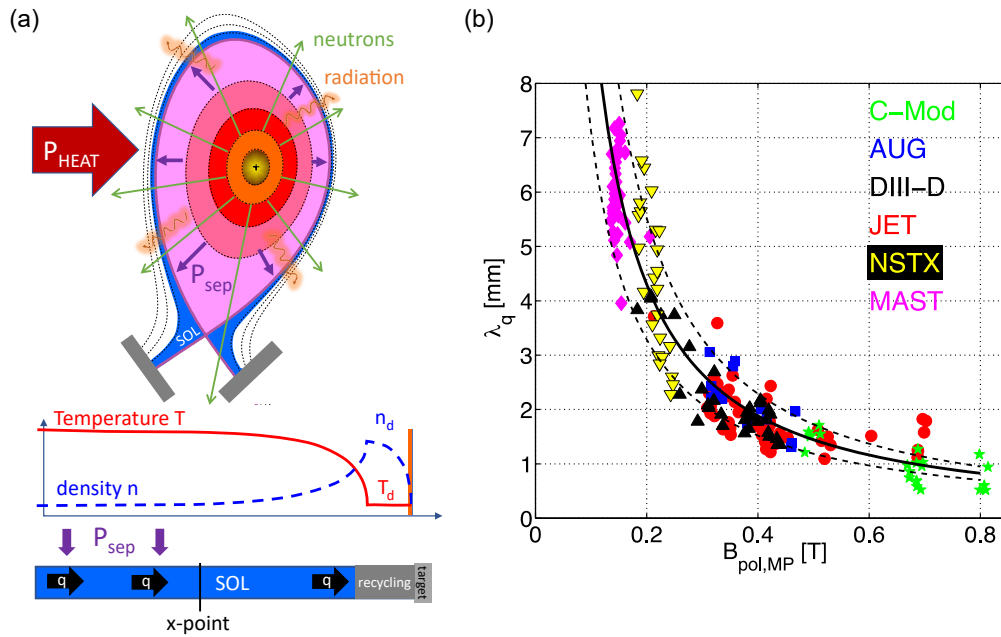


**Fig. 1.9:** (a) Power balance of a tokamak. The power crossing the separatrix  $P_{sep}$  has to be dissipated in the scrape off layer. This happens predominantly in a small area with width  $\lambda_q$ . (b) Power fall-off length versus poloidal magnetic field. Machines with larger plasma current / poloidal field show a smaller heat-flux footprint [13].

in the scrape off layer and is transported along the field lines to the divertor. At the divertor target the high heat ( $q$ ) and particle fluxes ( $\Gamma$ ) lead to recycling of neutral particles from the plasma facing components. This causes a local increase in density and a decrease in temperature in front of the target. In future machines the high fluxes can degrade the material due to sputtering, erosion and the introduction of displacements into the material. The magnitude of the fluxes depends not only on the amount of power and particles but also on the area to which it is distributed. Figure 1.9(b) shows the power fall-off-length<sup>10</sup> as a measure of this area, from different tokamaks, plotted over the respective poloidal magnetic field [13]. If this scaling is extrapolated to ITER, with an expected plasma current of 15 MA and a minor radius of 2 m, leading to a poloidal field on the order of 1.5 T, the power fall off length will be in the sub-mm range. In other words, if no counter measures are taken, the steady state power will be deposited in a very narrow area leading to extremely high heat flux exceeding material limits of  $5 - 10 \text{ MWm}^{-2}$  in future machines [14, 15].

In addition to the steady state flux the additional transient heat loads due to ELMs have to be considered when extrapolating an H-mode scenario to a reactor. The

<sup>10</sup>the length where the deposited power at the target has decreased by a factor of e

transient material limits are mainly determined by the surface temperature increase due to the short time scale (about one ms) of the individual events and are reported to be around  $0.15 - 0.5 \text{ MJ/m}^2$  to avoid the melting of material edges [16, 17]. In a first approximation, the power that is lost due to an ELM depends on the energy loss  $\Delta W_{\text{ELM}}$  and the ELM frequency  $f_{\text{ELM}}$ . It has been reported to be [18, 19]

$$P_{\text{ELM}} = \Delta W_{\text{ELM}} * f_{\text{ELM}} \approx 0.2 - 0.3 P_{\text{HEAT}}. \quad (1.1)$$

A useful measure for the ELM impact is the so-called plasma collisionality

$$\nu_e^* = 6.9 \times 10^{-18} \frac{R q_{95} n_e Z_{\text{eff}} \ln \Lambda_e}{\epsilon^{3/2} T_e^2} \quad (1.2)$$

that depends on the major plasma radius  $R$  the safety factor<sup>11</sup> at 95 % flux  $q_{95}$  the plasma density  $n_e$ , the effective ionic charge  $Z_{\text{eff}}$  and the Coulomb logarithm  $\ln \Lambda_e$ <sup>12</sup>. It is inversely proportional to the electron temperature squared  $T_e^2$  and the inverse aspect ratio  $\epsilon$ .

Figure 1.10(a) shows the relative loss per ELM plotted over this neoclassically derived collisionality evaluated at the pedestal top for ELM scenarios on different machines. For higher temperatures and therefore lower collisionalities, the relative energy loss increases and for the ITER collisionalities reached in JET the values are around 15 – 20 %.

The exhaust arguments above all consider large so-called type-I ELM scenarios, but historically ELMs have been categorised into different types, depending on their relative energy loss on different machines. Figure 1.10(b) shows a sketch of the relative energy loss, again plotted over the pedestal collisionality to create an operational space of different ELM types. The different regimes are described in the following section:

- **Type-I ELMs** [22]: Also called large or sometimes giant ELMs, are the big crashes first discovered when the H-mode was first reached. Their frequency increases with the increase of input power [23, 24]. Relative energy losses  $\Delta W_{\text{ELM}}/W_{\text{ped}}$  of up to 20 % are reported. Their stability can be described in a linear magneto-hydrodynamical (MHD) formalism by coupled pressure gradient driven ballooning modes and current driven peeling modes [25, 26]. As discussed above, these ELMs have the most severe consequences for future

<sup>11</sup>a measure for the slope of a field line  $q = \frac{r B_\phi}{R B_\theta}$

<sup>12</sup>the factor by which small-angle collisions are more effective than large-angle collisions

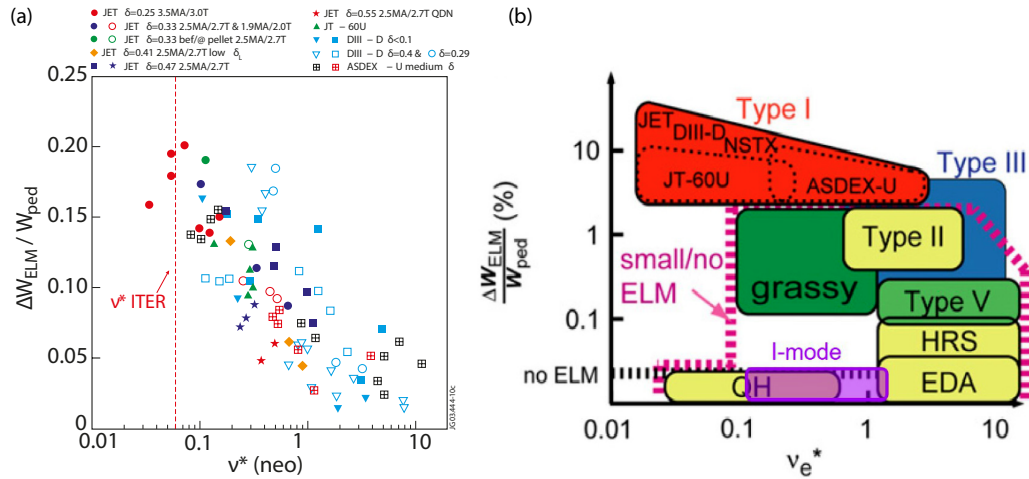


**Fig. 1.10:** Relative ELM energy loss,  $\Delta W_{\text{ELM}}/W_{\text{ped}}$ , versus pedestal electron collisionality (a) measured in various type I ELM phases of different tokamaks [20] and (b) sketched for various small-ELM and no-ELM regimes [21].

machines. Different techniques have been tried in order to reduce their impact either by increasing their frequency with ELM triggering via pellets [27] or by vertical kicks to the plasma [28, 29, 30, 31]. Large type-I ELMs have also been shown to be suppressed by external magnetic perturbations. [32, 33, 34, 35].

- **Type-II ELMs** [36, 37]: Originally also called grassy or small ELMs [38, 39], appear at higher plasma densities, longer elongated and also highly triangular plasmas. They are smaller in amplitude and higher in frequency than type-I and have been observed on several machines [40, 41, 42, 43]. They have no strict input power to frequency dependence and cause a much lower relative energy loss  $< 5\%$ .
- **Type-III ELMs:** Following the definitions in [23, 24] a reverse heating power to ELM frequency behaviour compared to type-I ELMs is observed. They occur close to the L-H power threshold and sometimes precursors in magnetic measurements are reported [44]. Two different kinds of type-III ELMs have been found at AUG: ones close to the L-H transition with similarities to limit cycle oscillations or sometimes called I-Phase [45, 46] and ones in high radiation scenarios at high densities [47].
- **Type-IV ELMs:** Discovered at DIII-D, these ELMs appear at low confinement and low densities [40]. They are now generally included in the type III ELM definition.
- **Type-V ELMs:** were found and named at the spherical tokamak NSTX [48]. They appear with gas fueling from the mid-plane and show relative drops in

the plasma stored energy smaller than 1 %. They can appear simultaneously with type I ELMs and similarities to the high recycling steady H-mode on JFT-2M [49] are reported.

- It is also worth mentioning that several operational scenarios without type-I ELMs have been found and recently dubbed **naturally ELM free regimes** in contrast to ELM suppression using external magnetic perturbations. These include the so-called improved energy confinement mode or I-mode which is characterized by a temperature pedestal but no density pedestal [50], the quiescent H-mode, with its main characteristics being an edge harmonic oscillation that increases particle transport [51] and the enhanced D-alpha regime that was found on Alcator C-Mod [52] and was recently further explored on AUG [53].

The main part of this thesis focuses on what was formerly called type-II ELMs on AUG and an additional regime termed grassy ELMs on TCV. If not otherwise stated, all scenarios without type-I ELMs discussed in this thesis are called small-ELM regimes as the similarities of the regimes outweigh their differences.

## 1.3 Thesis Objectives and Structure

The aim of this thesis is to explore the small ELM regime on ASDEX Upgrade and also on TCV, with special emphasis on the origin of small ELMs and their transport. As small ELMs are an edge instability their origin must be somewhere in the pedestal region. However in order to extrapolate their possible appearance to future larger machines, it is of utmost importance to determine, whether they originate from an instability close to the separatrix or further inside from the pedestal top. The transport of small ELMs influences mainly two important quantities: the perpendicular fluxes in the scrape-off layer and therefore the power fall-off length and the shape of the pedestal and therefore both the energy confinement via the pedestal top and its stability threshold against type-I ELMs.

The thesis is structured as follows:

### In Chapter 2

the main parameters of experimental tokamak physics are introduced, starting with the control room parameters of the two utilized tokamaks. This is followed by an overview of the diagnostics that were used to obtain all the data in this thesis and concludes with the tools to analyse and model the experimental results.

### **Chapter 3**

shows the results of a study with the aim of finding out the importance of the pedestal, the separatrix and the scrape-off layer density on the small ELM regime. This was achieved by switching between gas and pellet fueling.

### **Chapter 4**

explores a ballooning model to describe the small ELMs. This originated from experiments showing the dominant ELM types' dependence on slight changes in the plasma shape and therefore the magnetic shear very close to the separatrix.

### **Chapter 5**

reaffirms the ballooning model with further experiments on a second tokamak, namely TCV and shows some first filamentary and heat-flux data measured in the regime.

### **Chapter 6**

extends the ballooning model by comparing three different stabilization mechanisms, namely the local magnetic shear, the diamagnetic  $E \times B$  shear and the connection length between stabilizing high field side (HFS) and the ballooned low field side (LFS).

### **In Chapter 7**

the properties of small ELMs bursts inside the separatrix are investigated and first results on the effect that the scenario has on heat loads and therefore power exhaust are presented.

### **Chapter 8**

Summarizes all the findings and concludes with some ideas for future studies.



# Basic Experimental Tokamak Physics

” *An experiment is a question which science poses to Nature and a measurement is the recording of Nature’s answer.*

— **Max Planck**  
Physicist

This chapter introduces the two tokamaks that were exploited to obtain the data (section 2.1). The main actuators that are available to an experimental tokamak physicist in the control room are heating (section 2.2), fueling and seeding (section 2.3) and plasma shaping (section 2.4). The plasma diagnostics of both tokamaks are then explained (section 2.5) and the chapter concludes with ELM analysis and explanations of the modelling tools used in this work (section 2.6).

## 2.1 AUG and TCV

The experiments conducted for this thesis were carried out at the two medium sized tokamaks, ASDEX Upgrade and TCV. The distinctive features of these machines are discussed in this section. The design parameters of both machines are listed in table 2.1. Figure 2.1 shows the vessel structures including the plasma-facing components of AUG (orange) and TCV (blue). The major plasma radius  $R_0$  is defined as the distance between the torus axis and the magnetic axis and the minor radius

**Tab. 2.1:** Summary of the machine parameters of AUG and TCV.

	$R_0$ m	$a$ m	$V$ $\text{m}^3$	$P_{\text{aux,max}}$ MW	$B_{\text{T,max}}$ T	$I_{\text{P,max}}$ MA	$t_{\text{pulse,max}}$ s
AUG	1.65	0.50	14	30	3.90	1.6	10
TCV	0.89	0.25	8	5.5	1.54	1.2	4

$a$  is defined as the radial difference of the magnetic axis and the separatrix<sup>1</sup>. For illustrative purposes the TCV major radius was shifted by 0.76 m in the figure.

### 2.1.1 ASDEX Upgrade

The Axial Symmetrisches Divertor Experiment Upgrade (ASDEX Upgrade, AUG) has been in operation since 1991 and is currently the largest tokamak fusion experiment within the EU [54]. It is operated by the Max Planck Institute for Plasma Physics (IPP) and located in Garching near Munich, Germany. Besides the exploration of the diverted plasma configuration, the research nowadays focuses on the support of ITER and preparation of DEMO.

ASDEX Upgrade was the first tokamak to demonstrate operation with all tungsten plasma-facing components [55]. It is approximately a factor of two smaller in minor plasma radius  $a$  and major plasma radius  $R_0$  than the UK's Joint European Torus (JET), which is currently the world's largest running tokamak experiment. Moreover, the heating power installed as compared to the machine size is in the range of future machines making ASDEX Upgrade a leading device for power exhaust studies.

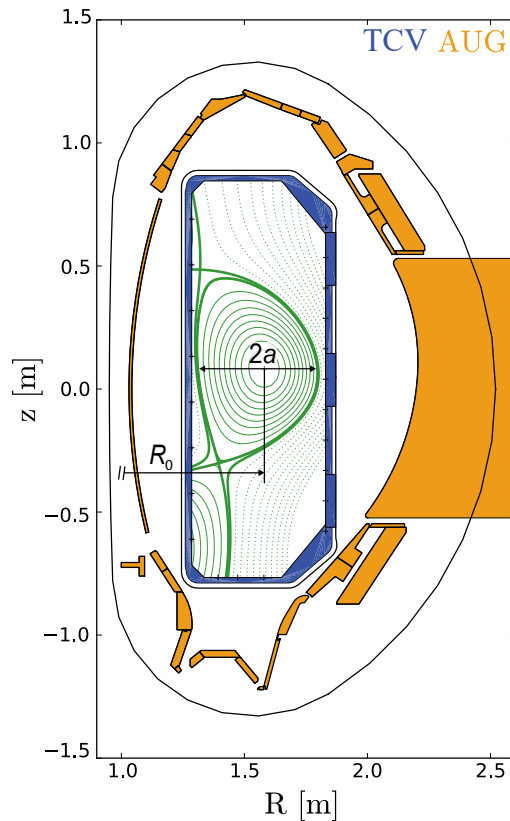


**Fig. 2.1:** AUG and TCV vessel structures with definition of major radius  $R_0$  and minor plasma radius  $a$ . Major radius of TCV is shifted by 0.76 m to fit inside AUG.

<sup>1</sup>more accurately the minor radius is defined as half the distance between the maximum and the minimum radial extent of the separatrix

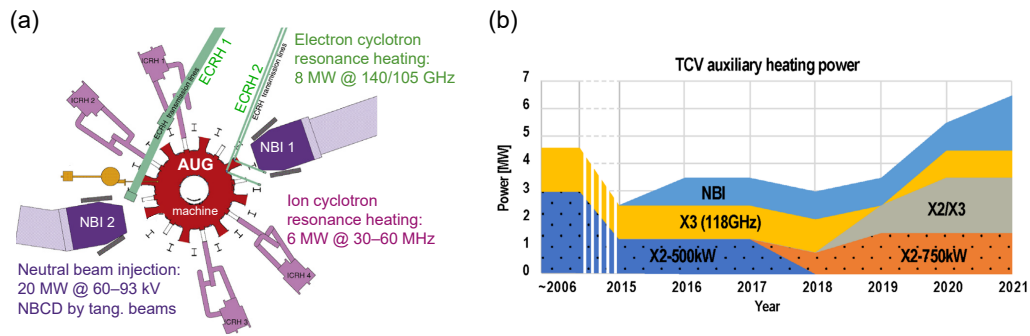


Fig. 2.2: (a) Heating system of AUG in 2020 adapted from [57], (b) Evolution of the installed heating power at TCV [58].

## 2.1.2 Tokamak à Configuration Variable

The Tokamak à Configuration Variable (TCV) [56] has been in operation at the Swiss Plasma Center in Lausanne, Switzerland, since 1992. It has been designed to examine a multitude of plasma shapes. This is made possible by 16 poloidal field coils that are powered independently and by an open vessel geometry. TCV is well suited to investigate the effects of different shapes of the confined region, e.g. closeness to double-null or changes in plasma triangularity or elongation (definitions are given in chapter 2.4). The plasma-facing components of TCV are made of carbon, and in the 2019 campaign baffles have been included to examine divertor recycling.

## 2.2 Heating

As described in chapter 1.2.3, a fusion plasma needs to be heated and fueled using external sources to balance outward energy and particle transport. In the following section the heating systems used at AUG and TCV are explored while the different fueling systems are explained in section 2.3.

### Neutral Beam Injection

The neutral beam injection (NBI) is the most commonly used heating system on both machines and provides up to 20 MW of power on AUG and 1 MW at TCV.

**Working principle:** A high energy neutral beam is produced in four steps:

- ion production in a low temperature plasma
- extraction and acceleration of said ions with high voltages
- neutralisation of this ion beam via charge exchange in a neutral gas cloud
- removal of the remaining non-neutral particles with deflection fields into an ion dump

The neutral particles with high kinetic energy that are injected into the plasma transfer their energy to the plasma particles through collisions and subsequently heat them.

As depicted in figure 2.2, the AUG NBI system consists of two beam boxes with two pairs of sources each that can produce 60 – 90 keV neutral deuterium or hydrogen. Some of these eight sources are aligned almost radially and others more tangentially. With the different beam angles the NBI system cannot only heat the plasma at different positions but it can also be used to influence the plasma momentum (plasma rotation) and as a current drive system. On TCV the 27.8 keV NBI system was expanding its capabilities during the course of this work. In 2017 a maximum input energy of 1 MJ (1 MW for 1 s) was possible, while the system capabilities were increased and it has been able to do 1.3 MW for 1 s since the end of 2019. An additional NBI source is planned to be installed in 2021.

## Wave Heating

Plasmas can also be heated by injecting waves at the gyrofrequency of the plasma particles into the plasma. This gyrofrequency

$$\omega_c = \frac{ZeB}{m} \quad (2.1)$$

depends on the charge  $Ze$  and the magnetic field strength  $B$  and it is inversely proportional to the particle mass  $m$ . In fusion relevant plasmas it is, therefore, in the 100 GHz range for electrons and in the 100 MHz range for ions.

The frequency and/or the wavelength of the inserted waves must be chosen to satisfy the plasma dispersion relation, that is, the condition for the wave to exist and propagate in the plasma and allow the wave to deposit its energy in a layer that corresponds to a plasma resonance, typically in the plasma core.

**ECRH:**

For electron cyclotron resonance heating (ECRH), gyrotrons are used which produce electromagnetic radiation in the GHz range through the maser effect. This radiation can then be directed into the torus with the help of mirrors. In this way, most components of the heating system can be placed outside the torus hall. Depending on the polarization of the waves, ECRH can be used in O-mode ( $E \parallel B$ ) or the X-mode ( $E \perp B$ ). On AUG the geometry and the magnetic field strength make the second harmonic of the X-mode (X-2) the most efficient way of heating the plasma. On TCV there are two different ECRH systems. One is used for low to medium density plasmas using the X-2 mode, similar to AUG, and the other one for higher density plasmas using the third harmonic X-3 mode.

On AUG the system has recently been upgraded and now consists of eight gyrotrons being able to deliver 1 MW each for a total of 8 MW. All gyrotrons can emit waves at 105 GHz for plasma discharges with lower fields (e.g. 1.9 T) and 140 GHz for the normal 2.5 T operation [59].

The TCV ECRH system has also been upgraded (see figure 2.2(b)). The nominal power of each of the six X-2 82.7 GHz gyrotrons is 465 kW resulting in a total of 2.79 MW of heating power with 2 s of maximum pulse length. For the X-3 system each 118 GHz gyrotron provides 480 kW and in total 1.44 MW of heating power also with maximum pulse length of 2 s [60].

#### **ICRF with radio frequency antennas:**

Due to the difference in electron and ion mass the ion gyrofrequency is around  $10^3$  times smaller than the electron gyrofrequency. This translates to wavelengths on the order of meters. From radio frequency engineering it is known that best coupling is reached when the antenna size is in the same order of magnitude as the wavelength. Therefore, for ion cyclotron radio frequency (ICRF) heating, large antennas are implemented into the vessel structure. To avoid the oscillation of ions directly in front of the antennas they are always shielded using Faraday screens in order to reduce the local electric fields. Different ICRF absorption schemes are available to determine whether the resonant ions will predominantly transfer their energy to the bulk ions or to the electrons. As for all waves transmitted by antennas, best coupling is reached when the impedance of the antenna is matched to the receiver. For an evolving fusion plasma this is a non-trivial problem that requires complex wave physics.

The AUG ICRF system consists of four antennas that can put 6 MW at frequencies of 30 – 60 MHz into the plasma.

The heating mix in the small ELM scenarios mostly comprised a base load of NBI with some additional wave heating for impurity control. Later chapters also explore the dependence of the small ELMs on the different heating levels and composition.

## 2.3 Fueling and Seeding

This section describes how the particle content of the plasma can be kept in equilibrium using gas and pellet fueling. Additionally, the systems described can also be used to seed the plasma with different gases in order to turn the heat-flux aiming at the target plates into radiation and therefore cool the plasma at different locations.

### Gas Valves

Neutral particle dynamics play a big role in plasma stability and exhaust. It is therefore of great interest in which quantity, at what speed and from which location these particles come from. The standard approach for particle input into a tokamak is using gas valves. Figure 2.3 gives an overview of the gas inlet systems of AUG and TCV. A toroidal/poloidal cross section of AUG can be seen in figure 2.3(a)/(b). All the colored clouds depict gas valves and their color represents the poloidal location. Blue and green clouds display upper divertor and midplane valves while yellow and red ones show lower divertor valves. The gas valves are all connected via a matrix to all of the gas bottles to allow high flexibility<sup>2</sup> [61]. In figure 2.3 (c) and (d) the TCV gas valve configuration of the years 2017/18 and 2019/20 is shown. The red and blue valves are predominantly used for fueling the main gas species, while the yellow corner valve is often used for nitrogen seeding. For better control of the neutral particle transport, so-called divertor baffles (green in figure 2.3) have been installed in TCV in summer 2019 and one of the main gas valves changed location to be able to fuel the plasma from the top.

In chapter 7, a study examining the influence of different fueling locations and magnitudes on the small ELM bursts and filaments is presented.

### Pellet Launcher

Another way to fuel the plasma is by injecting pellets of frozen fuel. Figure 2.4 shows the AUG pellet launcher system which works as follows [63]: A frozen fuel rod is

<sup>2</sup>Any gas bottle, e.g. H<sup>2</sup>, D<sup>2</sup>, N<sup>2</sup>, He, Ne, Ar or Kr can be connected to any valve.

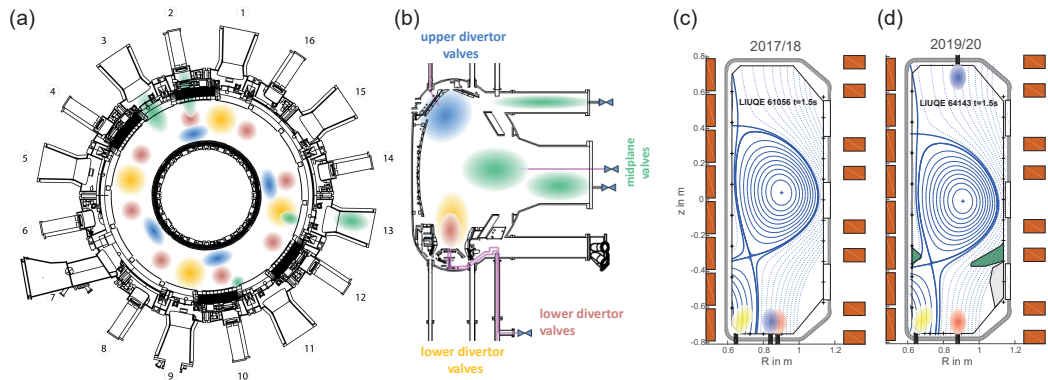


**Fig. 2.3:** Gas Fueling Systems: (a)/(b) show a toroidal/poloidal view of the AUG gas inlet systems. Different colors represent the different valve locations (adapted from [61]). (c) and (d) represent the 2017/18 and 2019/20 TCV gas inlet system. In 2019 a baffle structure was included in TCV to influence neutral particle flux.

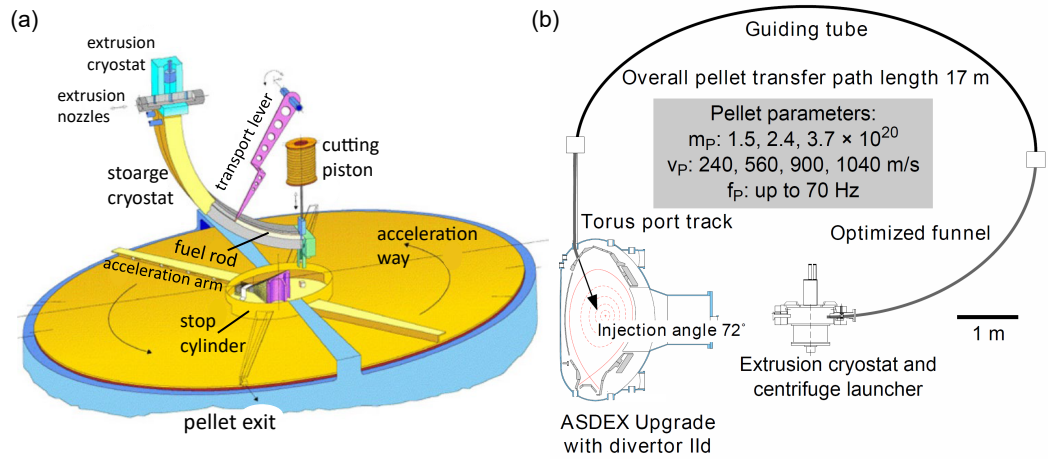


**Fig. 2.4:** AUG Pellet Launcher System: (a) shows the centrifuge with the cryogenic system making and accelerating the pellets (b) shows the guiding system needed to get the pellets to the HFS [62].

created and stored in a cryostat, transported down to the centrifuge and cut with a magnetic piston. The pellet is then accelerated to the desired speed and exits the centrifuge, where it is guided to the plasma. As particle drifts point mostly outward, fueling from the HFS is more efficient. The AUG system therefore has a 17 m bent guiding tube to minimize friction, whereby the pellets travel from the centrifuge to a port on the HFS of the torus where they are injected at a  $72^\circ$  angle. The system can make deuterium and hydrogen pellets and mixtures of the two with three different sizes and insert them at one of four different pellet velocities. The desired fueling rate can then be set via the pellet frequency that can reach 70 Hz.

Using pellet injection, the fueling location can be shifted further inside the plasma compared to gas fueling. This effect is used in chapter 3 to decouple the pedestal top from the separatrix density.

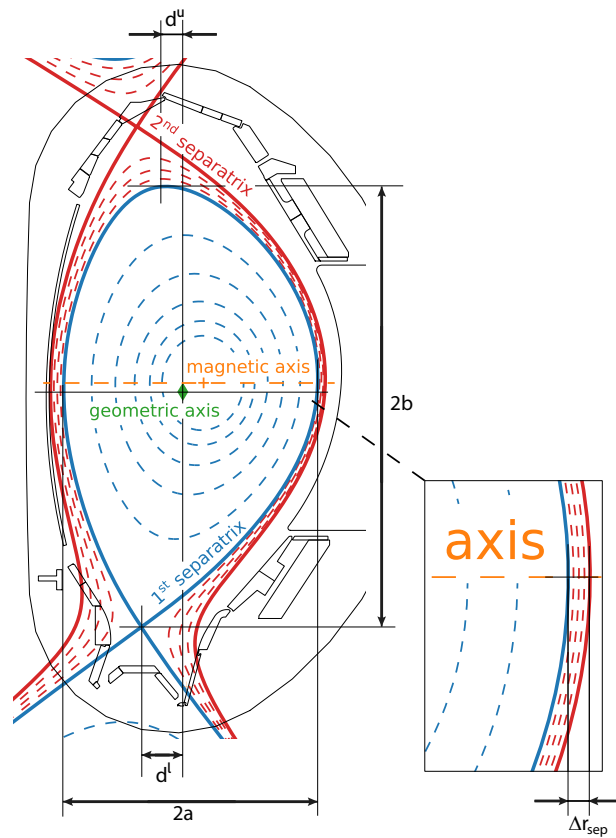
Pellet fueling has been used in the past for ELM pace making [64], where edge localized modes were triggered by high frequency pellets increasing the ELM frequency and reducing their intensity. Effects of different pellet sizes and velocities on type-I ELMs and small ELMs will be discussed in chapter 3.

## 2.4 Plasma Shaping

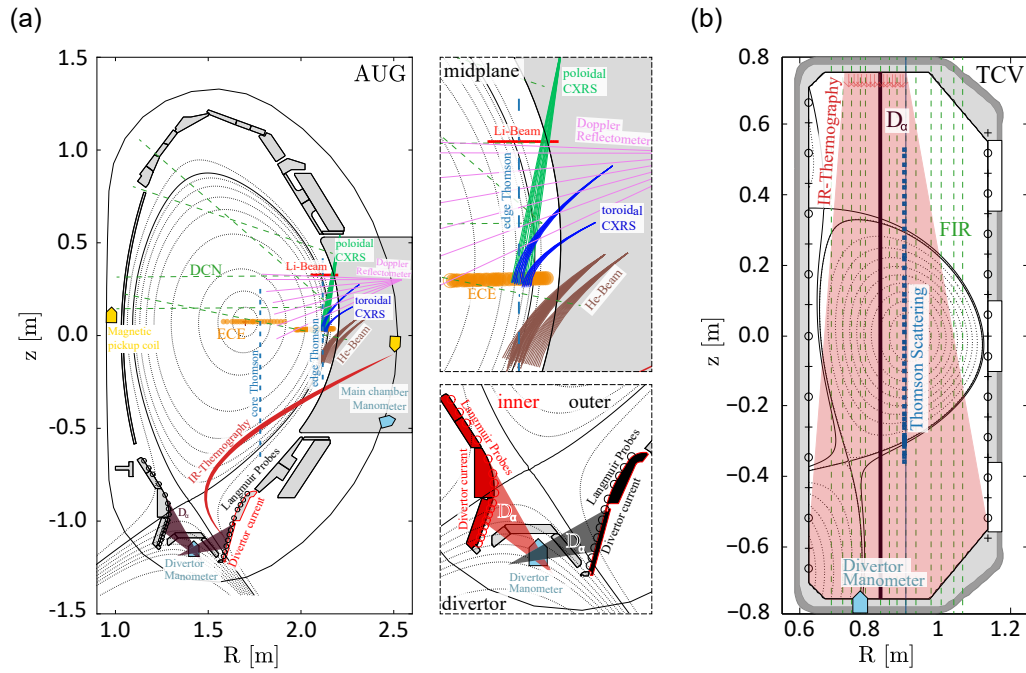
In past tokamak experiments various shapes of the magnetic flux surfaces have been explored. Starting from circular plasmas that were limited by the vessel wall the development moved to diverted plasmas with X-points at the bottom in the so-called lower single null (LSN) configuration. Current machines are also able to produce X-points above the plasma to examine particle drift effects that point in opposite directions in this upper single null (USN) configuration. It is also possible to produce plasmas with two X-points inside the vessel and two separatrices. The configuration where these two separatrices merge is called double-null (DN). TCV, as its name suggests, is uniquely equipped to run various plasma shapes and can even run doublet configurations with an X-point in the middle of the plasma.

Figure 2.5 shows the flux surfaces of AUG discharge #34483 in a configuration close to double-null (CDN). The green diamond denotes the geometric-, and the orange cross the magnetic axis of the plasma. The main plasma shaping quantities of interest in this work are the elongation  $\kappa = b/a$ , the upper and lower triangularity ( $\delta_u = d^u/a$  &  $\delta_l = d^l/a$ )<sup>3</sup> and the distance between the two separatrices  $\Delta r_{\text{sep}}$ . The

<sup>3</sup>Some sources also define the triangularity with respect to the average major radius  $R_{\text{mid}} = (R_{\text{out}} - R_{\text{in}})/2$ , where  $R_{\text{out}}$  and  $R_{\text{in}}$  represent the outermost and innermost radial plasma position.



**Fig. 2.5:** Equilibrium of AUG discharge #34483 defining the magnetic and geometric axis, the elongation  $\kappa = b/a$  the upper and lower triangularity ( $\delta_u = d^u/a$  &  $\delta_l = d^l/a$ ) and the distance between the two separatrices  $\Delta r_{sep}$ .



**Fig. 2.6:** Poloidal positions of plasma diagnostics on (a) AUG and (b) TCV. For better visibility the midplane and divertor region of AUG are shown in magnified zoom plots.

influence of elongation on the ELM characteristics is further explored in chapter 4.1 while chapter 6 focuses on the stabilizing effect of triangularity and closeness to double-null.

## 2.5 Advanced Plasma Diagnostics

In this section the plasma diagnostics of both tokamaks that were used in this thesis are introduced. This is done by a brief introduction to the diagnostic concept and an overview of the respective technical execution. The diagnostics are sorted by the quantities that they measure.

### 2.5.1 Kinetic Profiles

The electron density is measured in the two machines by probing the refractive index using interferometry, and by measuring scattered light from laser pulses. The radial density profile can also be measured with microwave reflectometers, and on AUG also via neutral lithium and helium beam diagnostics.

## Interferometry for $n_e$ :

### Physical principle:

The refractive index of a plasma depends on its density:

$$N = \sqrt{1 - \frac{\omega_{pe}^2}{\omega^2}} \approx 1 - \frac{n_e e^2}{2\epsilon_0 m_e \omega^2}, \quad (2.2)$$

where  $\omega_{pe}$  is the plasma frequency,  $\omega$  the frequency of the light passing through,  $n_e$  the electron density and  $m_e$  the electron mass. The line integrated density of a plasma can therefore be inferred by passing a modulated laser<sup>4</sup> with a certain beat frequency  $\omega$  through it and comparing the phase shift of the light to a reference beam. The phase shift can be calculated by integrating the refractive index along the laser path through the plasma:

$$\Delta\phi = \frac{2\pi}{\lambda} \int (N_{vac} - N(x)) dx = \frac{\lambda e^2}{4\pi c^2 \epsilon_0 m_e} \int n_e dx, \quad (2.3)$$

Due to the periodicity of the beat wave, only the fractional phase difference is directly measurable and the total number of periods in the phase shift must be counted from the beginning of the discharge.

Local changes in the plasma produced by pellets, or interference in the electronics by ICRF heating, can corrupt the counting and lead to errors in the density time trace, called fringe jumps. These can often be corrected by comparing the line integrated density to other diagnostics.

### Technical execution:

On AUG a deuterium cyanide (DCN) laser with a wavelength of  $\lambda_{DCN} = 195 \mu\text{m}$  is passed through the plasma at five different locations shown by the green dashed lines in figure 2.6(a) [65]. AUG also has a vertical  $\text{CO}_2$  laser system with a higher acquisition frequency which was not used during the course of this thesis.

In TCV a 14-channel Mach-Zehnder type interferometer is used to measure along parallel chords in the vertical direction (green dashed lines in figure 2.6(b)). The system consists of a FIR (FarInfraRed with  $\text{CH}_2\text{F}_2$  difluoromethane gas) laser, pumped by a  $\text{CO}_2$  laser, emitting a continuous wave at  $184.3 \mu\text{m}$ , and a multi-element detector unit (InSb hot-electron bolometer). The laser beam is divided into a reference

<sup>4</sup>using the heterodyne principle, a lower beat frequency is produced with a rotating grating, which is easier to diagnose compared to the THz laser frequency

beam, which is frequency shifted by a rotating grating, and 14 probe beams passing the plasma at different radial positions measuring the line integrated density with 20 kHz [66, 67].

### **Thomson Scattering for $n_e$ and $T_e$ :**

#### **Physical principle:**

The scattering of electromagnetic radiation from the plasma electrons enables electron temperature and density to be measured. A short laser pulse (ns) is sent through the plasma which accelerates the electrons in the laser oscillating field while re-emitting radiation. With wavelengths of the laser much smaller than the Debye length, there is no correlation between the emissions from different electrons and the technique is therefore called incoherent Thomson scattering. With this assumption, the electron temperature of the localized scattering volume can be determined from the broadening of the scattered radiation spectra while the density is proportional to the total scattered power.

#### **Technical execution:**

Both AUG and TCV have Nd:YAG lasers emitting at a wavelength of 1.06  $\mu\text{m}$ . Multiple lasers allow for more pulses which increases the time resolution of the profiles. The lasers are guided through the vessel vertically at fixed radial locations. The laser positions and measurement locations can be seen in figure 2.6(a) and (b) as dotted blue lines. An optical system directs the scattered light to polychromators. This way multiple  $z$  positions can be probed corresponding to different  $\rho_{\text{pol}}$ . AUG has an edge and a core system at two different radial locations with one optical system each [68]. In 2018, TCV had one laser feed-through with three optical systems with 89 observation positions [69]. In 2019, a fourth optical system with 20 more lines of sight (not shown in the figure) was added to the TCV system leading to better coverage of the divertor region. The new system was not used in this work. The TCV system can measure temperature and density profiles with up to 60 Hz.

The AUG system has a spatial resolution of 3 mm and normally measures at 120 Hz (20 Hz for each of the six lasers). It has the capability of measuring in the so-called sequential mode, where the timing of the laser pulses can be changed leading to a higher temporal resolution for short time periods.

## Electron Cyclotron Emission for $T_e$ :

### Physical principle:

Electrons gyrating in the magnetic field emit radiation at the electron cyclotron frequency (see equation 2.1). When the electron density and the corresponding absorption is high enough and the plasma is called optically thick. The resulting radiation intensity corresponds to that of a black body. In this case the intensity of the radiation (radiation temperature  $T_{\text{rad}}$ ), at a certain frequency corresponds to the electron temperature  $T_e$  ( $T_e = T_{\text{rad}}$ ) at the location from which the radiation originates. Around the separatrix, the density is often low and the plasma is optically thin, which means that the radiation is not fully reabsorbed. As a result the radiation can be attributed to a wrong radial position ('shine through'). With the use of a forward model of the radiation transport, even the  $T_e$  from an optically thin plasma can be evaluated for most of the cases [70]. Such a model is implemented in the Bayesian framework of the IDA profile reconstruction that will be explained in a following section. At very high density plasmas, the cyclotron radiation is not able to propagate within the plasma leading to reflection ('cut-off').  $T_e$  cannot be modelled under these conditions.

**Technical execution:** The ECE system at ASDEX Upgrade measures the second harmonic X-mode radiation at sixty different frequencies with a sampling rate of 1 MHz using a heterodyne radiometer (see orange circles in figure 2.6(a)). Each frequency corresponds to a different radial position  $R$  depending on the total magnetic field  $B$ . Due to their high temporal resolution the ECE data can also be used to measure and locate MHD modes occurring in the plasma. Due to high densities in small ELM scenarios, the second harmonic X-mode radiation is often in 'cut-off' making a temperature profile reconstruction from ECE data challenging.

TCV has an ECE system as well but as this diagnostic was not exploited in the course of this thesis it is not described here.

## Lithium Beam for $n_e$ :

**Physical principle:** In a process similar to neutral beam heating, a neutral lithium beam (LiB) with 30 – 60 keV is created by first extracting Li ions from a heated  $\beta$ -eucryptite powder coated ceramic emitter, accelerating these ions using high voltages and neutralizing them via charge exchange in a sodium gas cloud. The beam is then injected into the plasma above the LFS midplane (see red line in figure 2.6) and gets excited or ionised by collisions. After the natural lifetime (on the order

of 10 ns), the excited state decays and emits characteristic line radiation. The 2p state is the most populated one for lithium. It emits characteristic Li I line radiation at 670.8 nm when decaying to the 2s state.

#### Technical execution:

On AUG the light is picked up by two different optical systems, one looking at the beam from the top down and one looking at the beam from the side, with 35 and 26 channels respectively. All light signals are digitized at 200 kHz frequency. The signals observed contain active contributions from the LiB and passive emission from the background plasma. To subtract this background signal, the lithium beam is modulated with a high voltage MOSFET switch [71].

The density profile is evaluated using a collisional radiative model. Like the ECE forward model, this collisional radiative model is now implemented in a probabilistic data analysis approach.

#### Integrated Data Analysis for $n_e$ and $T_e$ :

The IDA framework combines data from various diagnostics on AUG using statistical analysis to reconstruct density and temperature profiles [72]. The main principle of IDA is Bayes Theorem

$$P(H|E) = \frac{P(E|H)P(H)}{P(E)}. \quad (2.4)$$

Here the measurements are represented by  $E$ , while  $H$  stands for the hypothesis that supposedly explains the measurements.  $P(H|E)$  is the probability that the hypothesis is correct given the data and is called *posterior*.  $P(H)$ , also called the *prior*, contains the a priori belief in the hypothesis.  $P(E)$ , the model evidence is the probability to measure the data given all possible hypothesis and  $P(E|H)$  is the probability of the experimental quantities being observed given the current hypothesis and is also called the *likelihood*. In practice, the object of desire is the hypothesis that maximises the posterior. The absolute value as well as the model evidence can be discarded as one is independent of the hypothesis and the other is irrelevant. For the computation of  $P(E|H)$ , synthetic measurements are created using forward models. All diagnostics mentioned above can be included in the IDA model to create radial  $n_e$  and  $T_e$  profiles. Each diagnostic has a forward model which is used to maximize the posterior probability leading to the most likely  $n_e$  and  $T_e$  profiles.

As the diagnostics measure at different locations in the plasma, they have to be mapped to a common coordinate system ( $\rho_{\text{pol}}$ ) using the plasma equilibrium (see some sections below).

### Charge Exchange Recombination Spectroscopy for $T_i$ :

All the techniques above are used to derive the kinetic parameters of the electrons. To get a grip on the ion temperature in ASDEX Upgrade, several charge exchange spectroscopy (CXRS) systems are installed. They work as follows:

Omnipresent impurities in the plasma ionise and recombine and emit characteristic line radiation when relaxing back into the ground state. Ionised impurities in the path of the NBI beam, typically carbon, boron, nitrogen and helium, can gain an electron via charge exchange processes with neutral deuterium from the beam. They keep the same energy and velocity as the bulk of the same impurity species and their temperature can therefore be calculated from the Doppler broadening of the line radiation originating from those impurities. In AUG plasmas, the thermalization time between impurity and main ions is smaller than the transport times, and it is assumed that the impurity temperature is equal to the main ion temperature [73]. Additionally, the poloidal  $v_{\theta,\alpha}$  and toroidal  $v_{\phi,\alpha}$  velocity of the ions can be determined by using lines of sight that are distributed in both directions, where  $\alpha$  indicates the different impurity ion species. This data can then be used to calculate the radial electric field  $E_r$  using the radial force balance:

$$E_r = \frac{\nabla_r p_\alpha}{e Z_\alpha n_\alpha} - v_{\theta,\alpha} B_\phi + v_{\phi,\alpha} B_\theta \quad (2.5)$$

where  $Z_\alpha$  denotes the charge number,  $e$  the elementary charge and  $B_\phi / B_\theta$  the toroidal / poloidal magnetic field.

The lines of sight of the poloidal and the toroidal edge CXRS system are shown in figure 2.6(a) as green and blue lines. Two more systems observing the plasma core are installed, but have been left out as the analysis for this thesis focuses on the plasma edge.

Recently a Gaussian process fitting scheme [74, 75] was applied to combine the different charge exchange diagnostics in the so called IDI (Integrated Data analysis for Ion profiles) model. Gaussian profile fits are ideal to fit gradients of profile data including error bars. The technique has also been used in this work to get the

gradient of the  $E_r$  which is the main component of the  $v_{E \times B}$  shear (see chapter 6).

## 2.5.2 ELM Monitors

Due to their bursty nature, ELMs are visible in many signals of different plasma diagnostics. This section focuses on the deuterium alpha spectral line measurements that are used as main ELM monitor on TCV and the divertor shunt current measurements which are used for ELM detection on AUG.

### **D<sub>α</sub> radiation:**

The deuterium alpha spectral line is derived from electron transitions from the  $n = 3$  to  $n = 2$  quantum level of the deuterium atom. The signal is used to monitor the interaction of the hot plasma with neutral particles surrounding the plasma at the edge and in the SOL.

An ELM is typically detected by observing the emission of D<sub>α</sub> light near the divertor target plates. The largest emission cross section results from the interaction of electrons with neutral particles. Thus the intensity of the light is proportional to the electron temperature, electron density and the neutral density but the temperature dependence is non-linear with a maximum at around 10 eV. During the ELM, first a heat-pulse increases the temperature of the electrons at the target and then ions are also emitted which move down to the target plate on a longer time scale. There they also increase the light level of D<sub>α</sub> by releasing more neutral particles from the target plate, which then interact with the electrons. After rapidly reaching a peak, the D<sub>α</sub> light decays more slowly when the ELM event ends.

In machines with metal divertors, the target temperature varies much more than in carbon machines. Due to the lack of carbon radiation, the temperature in low fueling scenarios is often quite high, so that a temperature increase lowers the D<sub>α</sub> radiation [76]. In plasmas with very high fueling, e.g. detachment studies, the temperatures are much lower than in previous carbon machines which also leads to a lower D<sub>α</sub> emission. The D<sub>α</sub> light is, therefore, a less reliable ELM monitor in metallic machines like AUG.

### **Technical execution:**

The D<sub>α</sub> light is typically measured with photo diodes with a D<sub>α</sub> filter. Although there are several systems installed in AUG and TCV, in this thesis only data from the

divertor system was used in AUG (dark red shaded areas in figure 2.6) while at TCV the  $D_\alpha$  light measured by a photo diode pointing vertically top down through the torus was utilized (dark red line in figure 2.6).

### **Divertor Shunt Currents:**

As some drifts in the plasma ( $\nabla B$ -drift<sup>5</sup>, curvature-drift<sup>6</sup>) are charge-dependent, they lead to a separation of ions and electrons and therefore electric fields. These are compensated by electrical currents flowing along the field lines dampening this charge separation. Named after the people who discovered them, these are called Pfirsch-Schlüter (PS) currents. As long as the flux surfaces are closed, PS currents flow only parallel to the magnetic field line. But as those currents also form in the SOL, they cause transport to the divertor.

Additionally, when the plasma temperature in front of two grounded target tiles that are connected by a field line are different, the floating potentials are different. This leads to the flow of a so-called thermocurrent to compensate this potential difference.

These are the main components of currents in the scrape-off layer [77].

### **Technical execution:**

The scrape-off layer currents are measured at multiple toroidal and poloidal locations in AUG by shunt resistors that are included in the divertor tiles. The currents of different poloidal locations are added up to estimate the total current that is flushed out by an ELM. During type-I ELMs total currents can reach up to 30 kA. DIII-D also reports currents up to 25 kA [78]. For small ELMs the currents are below 10 kA and the signals often show an offset to the 0 kA line. The divertor currents are the main ELM monitor signal used for the AUG analysis of this work.

---

<sup>5</sup>induced by the non-uniformity of the magnetic field

<sup>6</sup>induced by the curvature of the particle trajectories

## 2.5.3 Heat and Particle Loads

### Infrared (IR) Thermography:

#### Physical principle:

IR thermography is used for the contactless measurement of the surface temperature of objects. The radiation emitted from a surface is proportional to its temperature and the photon flux  $\Gamma_\lambda$  at wavelength  $\lambda$  can be estimated by the spectral radiance of a black body that is described by Planck's law:

$$\Gamma_\lambda(T) = c_0 \epsilon \frac{2\pi c}{\lambda^4} \frac{1}{\exp(\frac{hc}{\lambda k_B T}) - 1} \quad (2.6)$$

Here  $\epsilon$  is the surface emissivity that is used to compensate for the fact that the material observed is not a black body.  $c$  is the speed of light,  $h$  Planck's constant and  $k_B$  Boltzmann's constant.  $c_0$  is a calibration factor and contains information about the spectral bandwidth and the viewing angle of the camera that is used to observe the thermal radiation.

#### Technical execution:

For the discharges performed in the course of this thesis, the AUG IR camera was pointed at a tile of the outer divertor because this is found to be the more challenging one as it is subjected to higher heat flux compared to the inner target [79]. The camera can collect data in the spectral range of around  $4.7 \pm 0.15 \mu\text{m}$  with a frequency of up to 2100 Hz and a spatial resolution of 0.6 mm/px. The measurement cone is depicted in red in figure 2.6(a) and appears bent because it's tilted to the poloidal plane.

The TCV infrared system used for this thesis is shown as the red shaded area in figure 2.6(b) and observes the floor of the vessel on which the outer strike line<sup>7</sup> intersects the wall. It measures with up to 10 kHz frequency<sup>8</sup> in the spectral range from 3.7 – 4.8  $\mu\text{m}$  with a resolution of  $320 \times 256 \text{ px}$  which can be reduced to a sub-frame of  $64 \times 16 \text{ px}$  when faster acquisition times are needed, e.g. to resolve ELMs.

The photon data measured by the IR system can be used as input for codes, e.g. THEODOR [81] to evaluate the heat flux profiles along the divertor.

<sup>7</sup>the line where the separatrix hits the outer divertor

<sup>8</sup>a readout time has to be taken into account, which reduces the frequency depending on the image size [80]

The peak heat flux reaching the target can also be estimated using the divertor current signals, see chapter 7.1.

### **Ionisation Pressure Gauges and Baratrons:**

Two different types of devices are used to measure the neutral particle density or pressure in magnetic confinement devices.

Linear hot cathode ionization manometers, also called ionization pressure gauges, use a hot cathode that emits electrons which accelerate in an electric field and ionize neutral gas particles inside the measurement head. An individual electrode collects the ions. The measured ion and electron currents are used to calculate the present neutral gas density. Additional information on the working principle is provided in [82]. In AUG several such manometers are distributed toroidally and poloidally. The two manometers used in this work are shown as light blue peaked squares in figure 2.6(a).

TCV uses baratron capacitance manometers for neutral pressure measurements (see light blue peaked square at the bottom of 2.6(b)), where a diaphragm is exposed to the neutral pressure and moves accordingly. The diaphragm is used as one plate of a capacitor and therefore the capacitance changes according to the neutral particle pressure.

A disadvantage of baratron manometers is that their electronics cannot withstand strong magnetic fields and therefore must be moved away from the torus. As the measurement in the baratron is capacitive, long wires leading to the device can cause stray capacitance which can compromise the measurement. On smaller machines like TCV this poses no problem. On AUG the use of baratrons is also still possible, but ITER will only use ionisation manometers to determine the neutral pressure.

## 2.5.4 Burst and Filament Characteristics

### Helium Beam:

The thermal helium beam diagnostic is implemented at the plasma edge slightly below the midplane of AUG (see brown lines in figure 2.6(a)). Its main objective is to measure the electron density  $n_e$  and temperature  $T_e$  simultaneously with high spatial and temporal resolution in order to investigate steady-state as well as fast transport processes in the plasma edge region. Therefore neutral helium is locally injected into the plasma at thermal velocities by an in vessel piezo valve [83]. This enables the measurement of line resolved emission intensities of four He I lines using an advanced polychromator setup. A collisional radiative model is used to reconstruct  $n_e$  and  $T_e$  profiles from the measured line intensity ratios. Ratios from the same spin species are used for the electron density reconstruction, whereas spin mixed ratios are used to infer electron temperature changes [84].

The system has a very high data acquisition frequency of 900 kHz and a high spatial resolution of up to 3 mm. Thus even the raw data of the spectral lines can be used for studies of high frequency plasma modes and to detect plasma bursts and track filaments in the SOL.

### Doppler Reflectometer:

As discussed for wave heating and the ECE diagnostic, waves in a plasma are reflected at a so called cut-off frequency. For O-mode waves this frequency is given by the plasma frequency

$$\omega_P = \sqrt{\frac{n_e e^2}{\epsilon_0 m_e}}, \quad (2.7)$$

where  $e$  denotes the elementary charge,  $\epsilon_0$  the vacuum permeability and  $m_e$  the electron mass.

The backscattering of an injected microwave beam can be used to measure the intensity and the velocity of electron density fluctuations, so-called turbulent eddies. The fluctuation velocity can be calculated from the Doppler shift in the spectrum of the backscattered beam. The probing beam propagates in the plane perpendicular to the magnetic field and is injected obliquely with respect to the normal of the magnetic flux surface to measure the perpendicular velocity of the fluctuations  $v_{\perp}$ . The velocity measured then consists of the intrinsic phase velocity of the fluctuations ( $v_{ph}$ ) and the  $E \times B$  velocity of the background plasma. In most cases the phase

velocity is negligible compared to the  $E \times B$  drift velocity [85]. Therefore,  $v_{\perp}$  can be used to calculate the radial electric field  $E_r$  when the local magnetic field is known. Furthermore, the intensity of the Doppler shifted component provides a measure of the relative turbulence level.

The reflectometry system used in the course of this thesis [86] is able to use a microwave beam in the W-band (75 – 110 GHz) or V-band (50 – 75 GHz) and the receivers can be optimized for O-mode or X-mode polarization depending on the expected plasma density. All of the small ELM discharges performed exhibited a high density, therefore the system was operated in W-band either O-mode for high current (very high density discharges) or X-mode for lower current (high density discharges). The system includes a steerable mirror that can redirect the beam to measure the turbulence level and  $v_{\perp}$  at different poloidal positions. The possible beam angles of the system can be seen in figure 2.6(a) as magenta lines. The system operates at 25 MHz acquisition rate and is therefore the optimal diagnostic to measure turbulent eddies, bursts or filaments.

## 2.5.5 Plasma Equilibrium Reconstruction

Magnetised plasmas can theoretically be described by magnetohydrodynamics (MHD) including macroscopic quantities such as density, velocity, temperature or pressure, similar to hydrodynamics. In this description, the plasma is most commonly treated as a single fluid. The MHD equations can be derived by coupling Navier-Stokes' and Maxwell's equations. Detailed derivations can be found in the literature [87, 88].

These MHD equations make it possible to infer how the current, magnetic field and pressure gradient can be arranged in order to achieve a stationary configuration, i.e. an equilibrium. Such a magnetic equilibrium is reached when the forces of the plasma pressure ( $\propto \vec{\nabla}p$ ) are in balance with the forces of the magnetic field ( $\propto \vec{j} \times \vec{B}$ ).

$$\vec{\nabla}p = \vec{j} \times \vec{B} \quad (2.8)$$

This implies that the magnetic field lines ( $\vec{B} \cdot \nabla p = 0$ ) and the direction of current flow ( $\vec{j} \cdot \vec{\nabla}p = 0$ ) lie on surfaces of constant pressure. The magnetic flux inside each of these surfaces is denoted by  $\psi$  and since it is constant on a flux surface, this also implies  $\vec{B} \cdot \vec{\nabla}\psi = 0$ .

In cylindrical coordinates with the z-axis denoting the axis of symmetry of a toroidal configuration, an equation can be derived that can be used to calculate the flux surface topology of an axisymmetric plasma. This equation, known as the Grad-Shafranov (GS) equation, takes the form

$$R \frac{\partial}{\partial R} \left( \frac{1}{R} \frac{\partial \psi}{\partial R} \right) + \frac{\partial^2 \psi}{\partial z^2} = -\mu_0 R^2 \frac{dp}{d\psi} - RB_\phi \frac{d(RB_\phi)}{d\psi} \quad (2.9)$$

which can be rewritten as

$$-\Delta^* \psi = \mu_0 R^2 \frac{dp}{d\psi} + f \frac{df}{d\psi} = \mu_0 R j_\phi \quad (2.10)$$

with the introduction of the flux function  $f = RB_\phi$  which is proportional to the poloidal current.  $-\Delta^*$  denotes Stoke's operator from hydrodynamics and the toroidal current density is defined as

$$j_\phi = R \frac{dp}{d\psi} + \frac{1}{\mu_0 R} f \frac{df}{d\psi}. \quad (2.11)$$

The goal of equilibrium reconstruction is to solve this partial differential equation for  $\psi$  and reconstruct the magnetic flux on a (2D) grid, describing the poloidal cross section of the plasma.

In practice, equilibrium reconstructions can be done predictively when the  $p$  and  $f$  profiles are known, or interpretatively by inferring  $\psi$  via measurements of the magnetic field at several locations outside the plasma.

### Free Boundary Solvers CLISTE, LIUQE, IDE

For AUG data, interpretative equilibrium reconstruction is most commonly performed using the CLISTE equilibrium solver [89, 90].

CLISTE reconstructs the magnetic flux from the field coil currents, several flux loops and poloidal and radial magnetic field measurements. The accuracy of the magnetic reconstruction can be improved by further constraints using several other measurements such as the knowledge of the safety factor  $q$  at a given location, the measured pressure profile or the currents in the divertor.

At TCV a similar working code called LIUQE is used that has been numerically optimized to do real time equilibrium reconstruction during plasma discharges [91].

The above mentioned equilibrium solvers calculate the magnetic flux separately for each point in time, which can lead to non-physical behavior, such as jumps in the current distribution of the plasma. In an effort to connect the individual solutions and create continuous reconstructed equilibria, temporal smoothing constraints can be used. Since such constraints are not based on physical processes it is preferable to substitute them by physically motivated constraints. One way of doing this is to solve the current diffusion equation (CDE)

$$\sigma_{\parallel} \frac{\partial \psi}{\partial t} = \frac{RJ^2}{\mu_0 \rho} \left( \frac{G_2}{J} \frac{\partial \psi}{\partial \rho} \right) - \frac{1}{2\pi \rho} \frac{\partial V}{\partial \rho} (j_{BS} + j_{CD}). \quad (2.12)$$

$\sigma_{\parallel}$  is the parallel conductivity composed of the Spitzer conductivity and a neoclassical correction term considering trapped particles.  $\rho^9$  denotes the normalized poloidal plasma radius that is defined to be 0 at the magnetic axis  $\psi_0$  and 1 at the separatrix  $\psi_{sep}$

$$\rho = \sqrt{\frac{\psi - \psi_0}{\psi_{sep} - \psi_0}}. \quad (2.13)$$

$J$  is the current density integrated over the poloidal cross section,  $V$  the plasma volume enclosed by a flux surface and  $G_2$  is a parameter proportional to the plasma current and the safety factor and it decreases radially with  $1/\rho$ .  $j_{BS}$  is the bootstrap current density (described in the next section) and  $j_{CD}$  is the current density driven by external sources such as NBCD or ECCD.

A coupling of the Grad-Shafranov equation and the current diffusion equation has been established in the Integrated Data analysis Equilibrium (IDE) code [92]. In principle this works as follows: the Grad-Shafranov equation solver provides an equilibrium at a time step. The current diffusion solver uses this equilibrium as a boundary constraint and calculates the current distribution of the next time step. The current distribution with included uncertainties is then provided to the Grad-Shafranov equation solver to calculate the equilibrium of the next time step. IDE equilibria can include similar constraints to CLISTE including magnetic measurements, scrape-off layer currents and pressure constraints that are obtained from IDA profiles.

---

<sup>9</sup>sometimes also denoted as  $\rho_{pol}$

## Fixed Boundary Solver HELENA

Stability codes (as discussed in the next section) require a high degree of numerical accuracy. It is, therefore, necessary to re-calculate the equilibrium with a higher resolution using a predictive equilibrium solver. On AUG this is predominantly done using the HELENA code [93] which, in addition to the equilibrium profiles  $p'$  and  $ff'$ , takes the plasma boundary as an input. The Grad-Shafranov equation is solved using so-called iso-parametric cubic Hermite finite elements which yield an accurate and continuous solution for the flux and the magnetic field. HELENA can calculate the metric coefficients of a straight field line coordinate system (chapter 2.2.1.4 in [87]). This implies that it cannot resolve the separatrix at which the safety factor  $q$  reaches infinity and the coordinate system breaks down. HELENA can also evaluate the ballooning stability of equilibria using the Suydam method and the Mercier criterion. This is explained in more detail in the following section.

The input boundary for HELENA calculations can be evaluated analytically by providing shape parameters such as triangularity and elongation, or, as it was done for this work taken from the solutions of interpretative solvers such as CLISTE and IDE.

## 2.6 MHD Modes and ELM Modelling

This section gives a brief overview of the common factors that determine ELM stability. Most tools are developed for the study of large type-I ELMs. The study of such tools is also worthwhile exploring for small ELM scenarios as the occurrence of one type can influence the other. This will be further explored in chapter 4.

As discussed in the previous section, the Grad-Shafranov equation can be used to calculate plasma equilibria. Like a pencil balanced on its tip, an equilibrium state can still be unstable to small or larger perturbations. The stability of MHD equilibria can be best described using the so-called energy principle. It follows from the application of the Ritz' variational principle to the energy of a linearized<sup>10</sup> ideal MHD system (derivations are given in chapter 3 of [87]) and yields the intuitive form of the energy variation of the fluid part of the system  $\delta W_F$  when a small perturbation  $\vec{\xi}$  is applied:

<sup>10</sup>All quantities are described by an equilibrium part plus a small perturbation  $X = X_0 + X_1$ .

$$\delta W_F = \frac{1}{2} \int_F \frac{|B_{1\perp}|^2}{2\mu_0} + \frac{B_{0\perp}^2}{2\mu_0} |\nabla \cdot \vec{\xi}_\perp + 2\vec{\xi}_\perp \cdot \vec{\kappa}|^2 + \gamma_a p_0 |\vec{\nabla} \cdot \vec{\xi}|^2 - \underbrace{2(\vec{\xi}_\perp \cdot \vec{\nabla} p_0)(\vec{\kappa} \cdot \vec{\xi}_\perp)}_{\text{pressure}} - \underbrace{\frac{j_{0\parallel}}{B_0} (\vec{\xi}_\perp \times \vec{B}_0) \cdot (\vec{\nabla} \times (\vec{\xi} \times \vec{B}_0))}_{\text{current}} dV. \quad (2.14)$$

The curvature of the magnetic field  $\vec{\kappa}$  is defined as  $\vec{\kappa} = (\frac{\vec{B}}{B} \cdot \vec{\nabla}) \frac{\vec{B}}{B}$  and '||' and '⊥' denote the parallel and perpendicular direction with respect to the magnetic field.

As the system's energy tends to a minimum, the positive terms of  $\delta W$  are stabilizing while the negative terms describe the system's instabilities.

The system's energy can also change by variations of the surface and vacuum term  $\delta W = \delta W_F + \delta W_V + \delta W_S$  which are omitted but can also play a role in plasma stability, especially for current driven modes. The terms in the first line of equation 2.14 are all positive and therefore stabilizing. They describe the propagation of Alfvén and sound waves through the plasma. The bottom two terms can both be positive and negative depending on the respective directions of the vector fields involved. These two terms can be used to describe the main kind of MHD instabilities:

### 2.6.1 Pressure Gradient driven Instabilities

The pressure term of 2.14 becomes negative when the pressure gradient  $\vec{\nabla} p$  and curvature  $\vec{\kappa}$  are parallel and positive when they are anti-parallel. As the plasma pressure increases towards the magnetic axis, the gradient points in this direction. The curvature of the toroidal field points to the torus center. The vectors are parallel, and therefore stabilizing on the HFS and anti-parallel / destabilizing on the LFS. Thus these regions are called good and bad curvature sides, respectively. One type of pressure driven instability at unfavourable curvature is the so called **interchange instability**. The plasma tends to a lower energy state when plasma and magnetic flux tubes interchange their position, meaning that the plasma expands when field lines get shorter and flux tubes that lie on different surfaces are interchanged. A sheared magnetic field can stabilize interchange instabilities because it would require a finite amount of field line bending to interchange two flux tubes. In a tokamak, this stabilization is described by the Mercier criterion [94]

$$-8 \frac{\mu_0 p'}{B_0^2} (1 - q^2) < r \left( \frac{q'}{q} \right)^2. \quad (2.15)$$

Here  $B_0$  is the toroidal field at the magnetic axis and the derivatives denoted with the prime are taken with respect to the minor radius  $r$ . The radial gradient length of the  $q$  profile is called the global magnetic shear

$$s = r \frac{q'}{q}. \quad (2.16)$$

If  $q > 1$  interchange instabilities are always stabilized in a tokamak, as the pressure gradient is negative. In other words for large enough  $q$ , the stabilizing contribution from the toroidal curvature on the high field side of the tokamak can dominate the destabilizing contributions from the low field side leading to unconditional stability against localized interchange instabilities. The Mercier criterion is derived for instabilities localized on rational surfaces with constant phase. This means that when a perturbation is decomposed into its toroidal ( $n$ ) and poloidal ( $m$ ) harmonics also called modes,

$$\vec{\xi}(r, \theta, \phi) = \sum_{m,n} \vec{\xi}_{m,n}(r) \exp(i(m\theta + n\phi)), \quad (2.17)$$

the criterion is derived for radii on which  $q(r) = m/n$  is a rational number.

## 2.6.2 Ballooning Modes

If the assumption of constant phase along the flux surface is dropped, localized modes on adjacent rational surfaces can interfere in a way that the amplitude cancels in the region of good curvature but becomes large in the region of bad curvature. As the instabilities are dampened on the inboard side and grow on the outboard side, the plasma gets blown up in this region like a balloon. The resulting instabilities are therefore called **ballooning instabilities**. Like the interchange instabilities, they are driven by the pressure gradient and stabilized by the magnetic shear. The ballooning stability of an equilibrium can be evaluated numerically (e.g. with HELENA) by using a shooting method to converge to a particular pressure gradient value that is then unstable. However, for the special case of a large aspect ratio tokamak with circular flux surfaces, a simple differential equation for a test function  $\hat{X}$  and the ballooning angle  $\theta^{11}$  can be derived to examine the stability [87]

<sup>11</sup>The ballooning angle is an artificial but mathematically valid extension of the poloidal angle to make the boundary conditions of the ballooning equation  $\rightarrow 0$  at infinity, making the solution calculable.

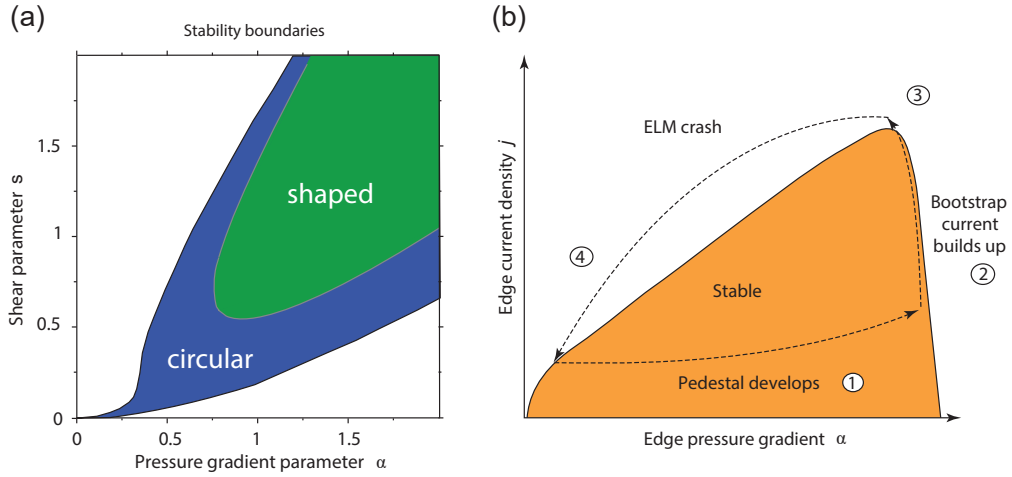


**Fig. 2.7:** (a) Ballooning stability diagram in a plane of normalized pressure gradient  $\alpha$  versus normalized shear  $s$  for circular flux surfaces (blue) and shaped plasmas (green), reproduced from [87]. (b) Sketch of the peeling-ballooning diagram for tokamak edge stability, reproduced from [25].

$$\frac{d}{d\theta} \left( (1 + (s\theta - \alpha \sin \theta)^2) \frac{d\hat{X}}{d\theta} \right) + \alpha((s\theta - \alpha \sin \theta) \sin \theta + \cos \theta) \hat{X} = 0. \quad (2.18)$$

Equation 2.18 shows the main parameters of ballooning stability, namely the magnetic shear  $s$  and the normalized pressure gradient

$$\alpha = -\frac{2\mu_0 R_0 q^2}{B^2} \frac{dp}{dr}. \quad (2.19)$$

The stability of the system against ballooning modes can therefore be described in  $s$ - $\alpha$  space, leading to so-called  $s$ - $\alpha$  stability diagrams. Such a diagram is shown in figure 2.7(a). In the left top of the graph the plasma behaves as explained above, namely a higher shear permits a higher pressure gradient before hitting the region of instability (colored). However, a second region of stable  $s$ - $\alpha$  configurations exists at very low shear and high pressure gradient in which increasing the shear would destabilize the plasma. This is due to the effect of the pressure gradient entering in the expression of the local shear in equation 2.18 and yielding a larger contribution from the high field side when averaging the curvature along a field line. In the simple circular picture, the second stability region is not accessible because the unstable region extends to the origin of the  $s$ - $\alpha$  space. However, a strong shaping of the plasma can alter the stability boundary in such a way that the second region is accessible (green area in figure 2.7(a)). In this case, a high localised current density

(see next section) can lead to a flat local  $q$ -profile and stabilize the ballooning mode. The second stable region also becomes accessible when using a more complete equilibrium model which includes the Shafranov shift in a self-consistent manner. The radial derivatives in equations 2.16 and 2.19 are then replaced by volume terms [95] yielding

$$s = 2V \frac{dq}{dV} \quad \text{and} \quad \alpha = -2\mu_0 \frac{dV}{d\psi} \frac{1}{(2\pi)^2} \left( \frac{V}{2\pi^2 R_0} \right)^{1/2} \frac{dp}{d\psi}. \quad (2.20)$$

### 2.6.3 Current driven Instabilities

The current term of equation 2.14 is proportional to the current density parallel to the magnetic field  $j_{0\parallel}$ . A high current density leads to a kinking of a plasma tube which minimizes the total energy although field lines are bent by the kinked topology. A mechanical analogue to such instabilities is the kinking of a towel when it is twisted. Due to the higher current density, kink instabilities are mostly relevant in the plasma core. However, due to a combination of the density gradient and the interaction of particles trapped by the magnetic mirror effect with free flowing particles, the plasma creates its own current which is therefore called the bootstrap current [96].

$$j_{\text{BS}} \propto \sqrt{\epsilon} \frac{\nabla p}{B_\theta} \quad (2.21)$$

It is roughly proportional to the pressure gradient and thus dominant at the edge of H-mode plasmas. Detailed expressions taking into account the plasma shape and particle collision rates can be found in the literature [97, 98]. Due to their localization at the edge, the appearing kinks "peel off" the plasma edge which is why they are also called **peeling instabilities**.

### 2.6.4 Peeling-Ballooning Modes

Due to their different drive mechanisms, peeling and ballooning modes have characteristic mode numbers and features. The current driven peeling modes have low  $n$  and are poloidally large in size, i.e. the corresponding  $m$  is also comparably low. The poloidal mode structure of an  $n = 3$  peeling mode in real plasma geometry is presented in figure 2.8(a). The mode structure is localised at the plasma edge and visible on both HFS and LFS.

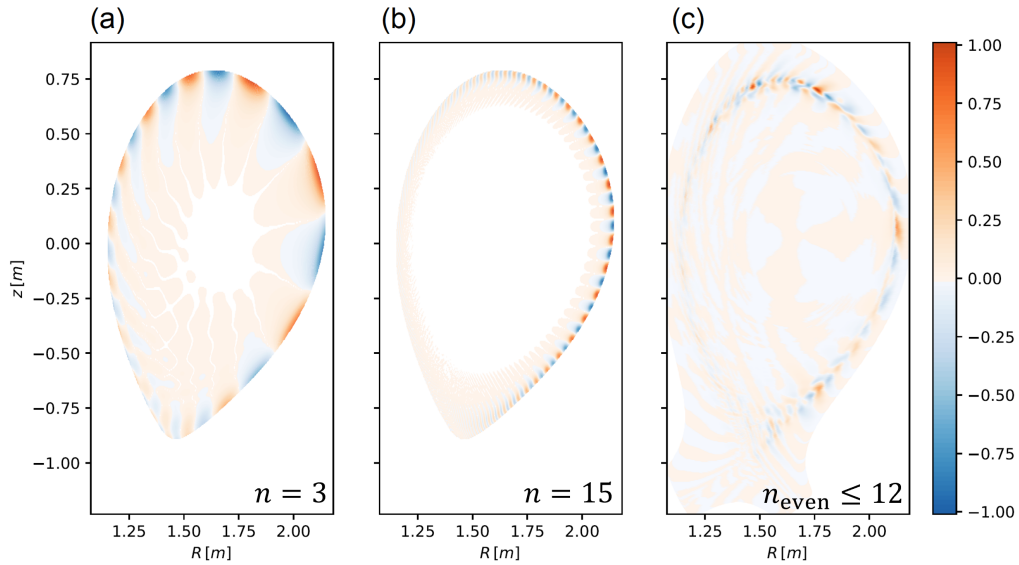


**Fig. 2.8:** Poloidal mode structures: (a) of a low toroidal mode number ( $n$ ) peeling mode, (b) a large  $n$  ballooning mode and (c) coupled peeling-ballooning modes visible as plasma potential fluctuations simulated with the JOREK code. The color represents the amplitude of the mode in (a) and (b) and the normalized potential fluctuation in (c).

In contrast, ballooning modes have relatively large  $n > 10$ . An example of an  $n = 15$  ballooning mode structure is shown in figure 2.8(b). The mode is located predominantly on the LFS, caused by the afore-mentioned ballooning effect. As both peeling and ballooning modes are localised at the far plasma edge at similar values of  $q = m/n$ , the ballooning associated  $m$  have to be higher as well leading to a smaller poloidal structure.

The peeling-ballooning (PB) theory couples the effects of pressure and current driven modes, and has been the most widely accepted theory to describe type-I ELM stability since the 90s [25, 26]. The basic ideas of this theory are still partly valid today and can be used to illustratively describe the ELM crash. The key points are shown in figure 2.7(b) and briefly described here:

Starting at stable plasma conditions, the pressure gradient increases until a critical  $\alpha$  is reached (1). Very localized ballooning modes become unstable and limit or slightly reduce the pressure gradient. The bootstrap current rises due to an increase of the edge temperature and therefore a reduction in collisionality (2). At a critical current density (3) a low  $n$  peeling mode becomes unstable and causes large transport leading to the ELM crash (4).

A more advanced model, that takes into account the width and height of the pedestal and is nowadays widely accepted, is the EPED model [99]. In combination with

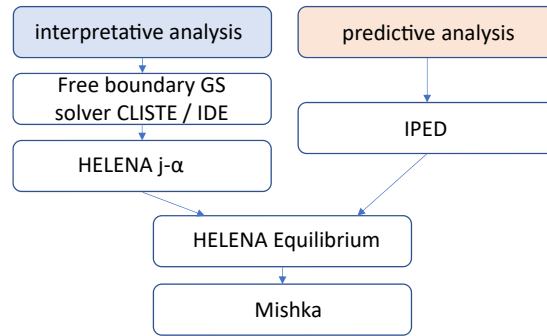


**Fig. 2.9:** Predictive and interpretative peeling-ballooning stability analysis workflow on AUG.

linear stability codes (see next section), it similarly describes the ELM evolution, where first a ballooning boundary is reached giving rise to a so-called kinetic ballooning mode which creates enough transport to limit the gradient. The width of the pedestal is assumed to scale with the normalized pressure  $\beta$  as  $\Delta_{\text{ped}} = c \cdot \sqrt{\beta_{\text{pol,ped}}}$ , where  $c$  is a constant matched to the experiment. The width of the gradient region still grows leading to a broader region in which the unstable mode can develop. At a certain point, the PB stability boundary is reached and the ELM crash occurs.

A similar code IPED has been developed at AUG [100] that also permits relative shifts in the temperature and density profile and has been utilized for this work.

## 2.6.5 Linear Stability Analysis

The minimization of the energy functional as described above only calculates whether the system is stable or not whereas normal mode techniques, which are used in the linear stability codes such as MISHKA [101], also return a linear growth rate. The normal mode technique solves linearized MHD equations for small perturbations. If a solution with a finite growth<sup>12</sup> rate is found, the system is considered to be unstable. Two different kinds of linear stability analysis have been performed in the course of this work. The workflows of these two different approaches are depicted in figure 2.9 and explained briefly in the following section.

<sup>12</sup>In this work 4% of the Alfvén growth rate was chosen as the limit

## Interpretative Analysis

In order to determine the peeling-ballooning stability of experimentally acquired plasma equilibria, the interpretative analysis workflow is used [100]. As shown on the left side of figure 2.9, the process starts by calculating a plasma equilibrium using the CLISTE or the IDE code with the input parameters mentioned in section 2.5.5. The equilibrium profiles  $p'$  and  $f f'$  and the plasma boundary (separatrix) of these equilibria are then used as input to calculate a more highly resolved equilibrium using HELENA. In this step HELENA can also be used to determine the  $\infty$ - $n$  ballooning boundary and return the normalized pressure profile at which the plasma would be unstable against ideal ballooning modes  $\alpha_{\text{crit}}$  and the marginal stability factor  $F_{\text{marg}} = \frac{\alpha_{\text{exp}}}{\alpha_{\text{crit}}}$  across the entire plasma cross section. When the HELENA reference equilibrium has been constructed, the pressure and current density profiles are modified to create a grid in  $j$  and  $\alpha$  using scaling factors. The profiles are changed in a way that the stored energy  $W_{\text{MHD}}$  and the total plasma current  $I_P$  are conserved. For each of these combinations of current density and normalized pressure gradient, another high resolution HELENA equilibrium is calculated and used as input for MISHKA to calculate the stability including the most unstable mode number. In a final step the data on the  $j$ - $\alpha$  grid are interpolated to create an image of the peeling-ballooning boundary.

## Predictive Analysis

To further explore the influence of the  $n_e$ ,  $T_e$  and current density profiles on the peeling-ballooning stability, the IPED code can be used to perform predictive analyses. The experimentally acquired profiles can be used as a starting point and then varied while keeping the pedestal width according to  $\Delta_{\text{ped}} = c \cdot \sqrt{\beta_{\text{pol,ped}}}$ . The current density is calculated using the bootstrap current formulae from [97, 98]. The altered profiles are then used for high resolution HELENA equilibrium reconstructions which in turn serve as input for MISHKA stability calculations. This technique has been used to explore relative shifts of the density and temperature profile [102] and for this work to explore the effect of changing the separatrix density.

### 2.6.6 Nonlinear Modeling with JOREK

Some ELM phenomena such as the peeling-ballooning stability can be analyzed with linear codes but as ELMs are explained by a coupling of modes, the problem

is fundamentally nonlinear. In addition, most linear stability codes run without separatrix geometry, which also has a stabilizing effect on current driven modes [103] and plays an important role in the description of ELMs.

The JOREK code has been developed to solve these problems i.e. to simulate ballooning modes and external kink (or peeling) modes located on open and closed field lines including the separatrix. The nonlinear MHD equations are solved on a 3D grid where the poloidal cross section is discretized using bi-cubic 'Bezier' finite elements [103] and the toroidal direction is decomposed into Fourier eigenmodes. The Bezier elements are a generalization of the cubic Hermite elements (used in the HELENA equilibrium code [93]). This representation of the poloidal plane allows an accurate alignment of the finite elements to the equilibrium flux surfaces. Different versions of the JOREK code exist for different purposes, including reduced and full MHD models and dedicated versions for disruption studies. The version used in this work solves the reduced nonlinear MHD equations including an  $E \times B$  drift term and has recently been used to simulate multiple type-I ELM cycles [104]. The starting point is a stable equilibrium solution of the GS equation reproduced from an experimentally observed case. Toroidal perturbations with multiple mode numbers are introduced at noise level and the system is evolved in time. A reduction in computation time can be achieved by using only even mode numbers while the simulation can reproduce ELM crashes. The plasma potential fluctuations during such an ELM crash including only even  $n$  up to  $n = 12$  are depicted in figure 2.8(c). First results in reproducing small ELM crashes with the JOREK code are shown in chapter 6. The derivation of the reduced MHD equations as well as further details on the JOREK code can be found in [105].

# Significance of the Separatrix

“ *It’s the edges of the maps that fascinate...*

— David Mitchell  
Author

*Parts of this chapter have been published in [106] and [107].*

## 3.1 Introduction

As explained in chapter 1, due to its higher confinement, the foreseen operation scenario for future fusion devices is the H-mode. Therefore the fusion community has great interest in the study of edge localized modes (ELMs). Large type-I ELMs will not be tolerable in future large devices because they will cause damage to the plasma facing components [14]. Different ideas for reactor relevant scenarios have been proposed. These range from mitigating or suppressing, to replacing type-I ELMs with smaller, more tolerable ELMs. Mitigation or suppression of ELMs via external magnetic perturbations mostly concentrates on plasmas with a low pedestal top collisionality, as expected for large machines [108]. Extrapolated ELM energy

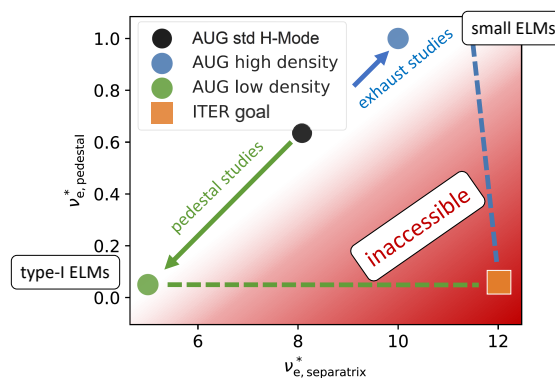


**Fig. 3.1:** Electron collisionality operational space diagram: collisionality at the pedestal top as a function of separatrix collisionality.

fluences for those mitigated ELMs compared to material limits in ITER could still be of concern [109, 110].

A sketch of the pedestal top in relation to the separatrix collisionality is depicted in figure 3.1 for AUG. Operationally it is not possible to obtain pedestals with low pedestal top collisionalities and reactor relevant exhaust scenarios at the same time. Scenarios optimized for exhaust studies come with high separatrix densities [111] in present day devices. There are, therefore, two lines of research towards mitigated or small ELMs. The first line deals with low density and low pedestal top collisionality, and the second one with high separatrix density which then comes with high pedestal top collisionality in medium sized tokamaks. ELM scenarios have been studied on several tokamaks (on ASDEX Upgrade (AUG) [112], on JET [113, 114] and as grassy ELMs on JT60-U [115]) leading to a large variety of different ELM types. These are reviewed in chapter 1.2.2 and in more detail in references [41, 39, 21]. The collisionality dependence of different small ELMs has more recently been examined [43, 42, 116]. Theoretical explanations in the frame of peeling-ballooning (PB) theory from AUG and JET [117, 118] suggest that small ELMs at high density and shaping (type-II ELMs) occur because of lower bootstrap current  $J_{BS}$  (global PB theory). Furthermore, a local mode mechanism to describe small ELMs theoretically has been proposed [119, 120]. The local or global nature of small ELM instabilities is not totally clear. Do they affect the whole pedestal region, or are they very narrow instabilities which become unstable close to the separatrix? Experiments to decouple pedestal top and separatrix parameters were already proposed and performed at AUG [121]. This work expands on these experiments and presents detailed analyses.

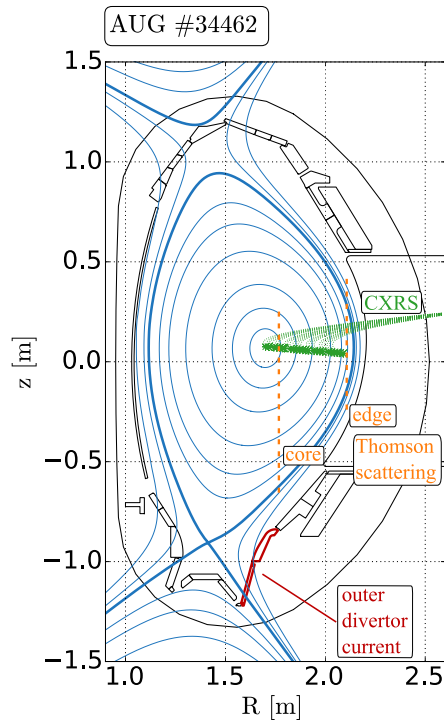


Fig. 3.2: Close to double null equilibrium of a discharge during a small ELM phase and utilized diagnostics.

## 3.2 Experiments and Simulations

The following section describes experiments in which the plasma transits from mainly small ELMs to the reappearance of type-I ELMs. The goal was to keep the pedestal top electron density and temperature as similar as possible. The overall shape of the plasma and the total heating power were also controlled to be constant.

The standard recipe to achieve a plasma with small ELMs at high density in ASDEX Upgrade consists of a start-up with a high deuterium gas puff followed by an upwards shift of the plasma close to a double-null shape. In Figure 3.2, the magnetic equilibrium of such a shape close to double-null is shown. As a measure of the closeness to double-null the radial distance of the separatrix and the separatrix of the upper X-point is  $\Delta r_{\text{sep}} = 12$  mm. Also shown are the profile diagnostics (see also section 2.5) that were used in this section, namely the core and the edge Thomson scattering (TS) system [122] (orange), as well as the charge exchange recombination spectroscopy (CXRS) system [123, 124] (green). The outer divertor tiles where the divertor current is measured via shunt resistors, is shown in red. As described in section 2.5, it is used as an ELM monitor. Starting from the plasma configuration in figure 3.2, experiments were carried out in which the goal was to change separatrix density independently of the pedestal top density.

### 3.2.1 Influencing the Separatrix Density

In tokamak plasmas we usually control the density via gas puffing. Here the dominant particle source lies outside the confined plasma, and therefore the separatrix density and the plasma density are closely linked [125]. When plasmas are fueled with pellets where particles are deposited further inside the confined plasma region, this link can be broken [126].

In figure 3.3 time traces of various plasma parameters of an ASDEX Upgrade discharge (#34462) are shown in which the plasma follows the high shaping and high gas puff recipe with a configuration very close to double-null (figure 3.2).

The stored energy stays constant at around 800 kJ (figure 3.3(a)) after 3.0 s. The radiated power  $P_{\text{RAD}}$  (figure 3.3(b), purple) and the heating powers  $P_{\text{NBI}}$  and  $P_{\text{ICRH}}$  (figure 3.3(b), red and green), are stable until 5.7 s, after which the ELM frequency is reduced. This leads to tungsten accumulation and thus an increase in  $P_{\text{RAD}}$  and results in loss of core temperature and thus  $W_{\text{MHD}}$ . As an ELM monitor the divertor current is shown in figure 3.3(c). The plasma is fueled via high gas

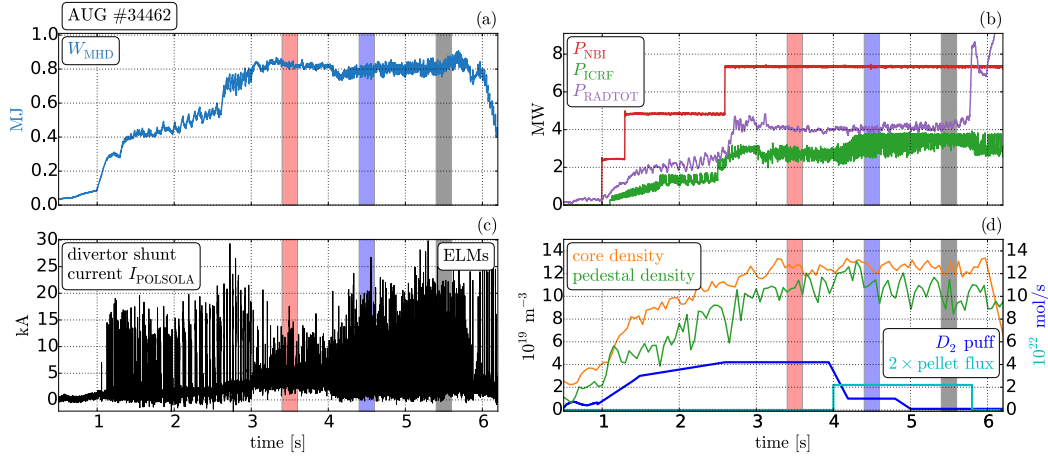


**Fig. 3.3:** Time traces of (a) stored energy ( $W_{\text{MHD}}$ ), (b) heating power of neutral beams ( $P_{\text{NBI}}$ ) and wave heating ( $P_{\text{ICRF}}$ ) as well as radiated power ( $P_{\text{RAD}}$ ), (c) outer divertor shunt current as ELM indicator and (d) core (orange) and pedestal electron density (green) measured by the Thomson scattering diagnostic, Deuterium gas puff (dark blue) and pellet flux (light blue) multiplied by 2 for better visibility.

puff during the small ELM phase between 3.0 s and 4.0 s (figure 3.3(d), dark blue), while in the phase between 4.0 s and 5.0 s it is fueled with pellets and a reduced gas puff and finally in the phase from 5.0 s to 5.8 s no gas puff is present and the plasma is fueled with pellets only. The pellet flux achieved from 4.0 s to 5.8 s was  $\Gamma_{\text{pellet}} = 1.1 \times 10^{22}$  mol/s (figure 3.3(d), light blue, scaled by a factor of two for better visibility). The pellet frequency was chosen to match the same core density in all phases and therefore the core and pedestal densities (from two different channels of the Thomson scattering diagnostic shown in orange and green) do not change significantly. However, the ELM characteristics, are distinctly different. The gas fueled phase is dominated by small ELMs and large ELMs appear again as soon as the gas puff is reduced.

Figure 3.4 shows a comparison of edge (a) electron density, (b) electron temperature, (c) electron pressure and (d) ion temperature for these three phases, called 'gas' (red), 'gas+pellets' (blue) and 'pellets' (black). The corresponding time windows are marked in figure 3.3 by colored bars. Electron density and temperature data from the Thomson scattering diagnostic are radially binned to reduce systematic noise. This is done by using a radial running average of density and temperature for all points in the specified 200 ms time windows. The median of six neighbouring points in space is represented by every plotted point. In addition, the modified tanh (mtanh) method described in [127] is used to fit the data-points shown in figure 3.4. The experimental error bars have only been plotted for the 'gas' case to increase visibility. Inside the separatrix, which is indicated by a solid black line, all

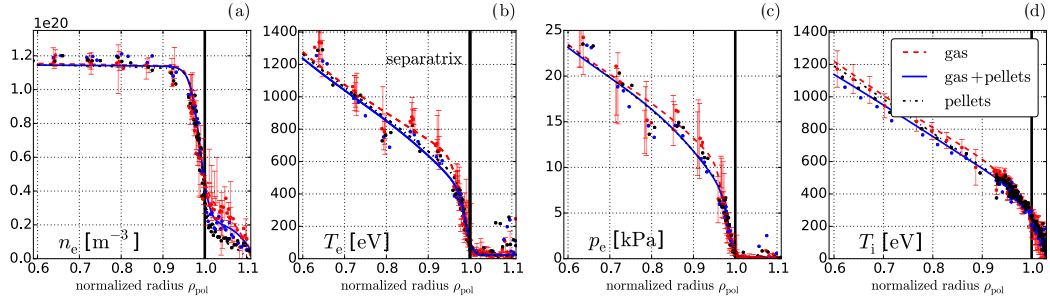


**Fig. 3.4:** Edge profiles of electron density, electron temperature, electron pressure and ion temperature for the three different phases indicated in figure 3.3, in which fueling changes from pure gas puff ('gas') to a mixture of gas puff and pellets ('gas + pellets') to pure pellet fueling ('pellets'). The height of the density 'shoulder' changes significantly in the plasma edge.

profile data are very similar and stay within their scatter width. The main significant difference in the profiles for the three different time windows lies in the electron density around the separatrix and in the scrape-off layer. A distinct density shoulder in the scrape-off layer is present in the gas fueled case which decreases (from red to black) as the gas puff is reduced and the fueling mechanism switched to pellets.

In the different phases, the electron and ion temperature profiles do not change significantly. The ion temperature profile at the separatrix is approximately 2.5 times higher than the electron temperature, as has been reported in other high density experiments at AUG [128, 123].

The difference in the density profiles at the separatrix is also found when computing the fall-off lengths  $\lambda_{n_e}$  and  $\lambda_{p_e}$  using the method described in [129], taking Thomson scattering data in the near SOL. The density fall-off length is reduced by more than a factor of two comparing the three phases, while for the fall-off length of the pressure profile a change of only 20% is observed.

time	dominant ELM type	$\lambda_{n_e}$	$\lambda_{p_e}$
3.5 s	small	45 mm	12 mm
4.5 s	mixed	35 mm	11 mm
5.5 s	large	20 mm	9 mm

**Tab. 3.1:** Fall-off lengths of electron density and electron pressure at the separatrix.

The outer divertor current (figure 3.5(a)-(c)) as well as the stored energy (figure 3.5(d)-(f)) for the three different phases indicate the respective ELM behaviour. Figure 3.5(a) shows the purely gas fueled phase in red. The divertor current shows some larger events with amplitudes in the range of 10 – 20 kA and corresponding losses in  $W_{\text{MHD}}$  of  $< 6\%$ . In between those, the small, high frequency ELMs exhibit

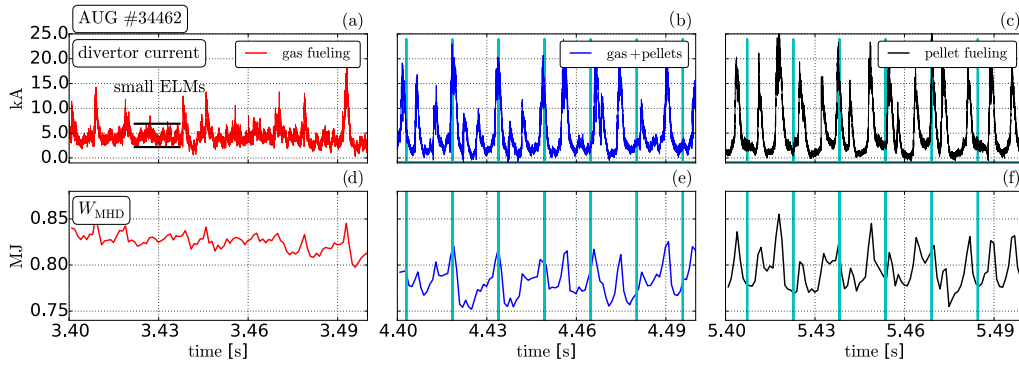


**Fig. 3.5:** Divertor current (a) - (c) and stored Energy  $W_{\text{MHD}}$  (d) - (f) of the three different time windows defined in figure 3.3, comparing gas (red), gas+pellet (blue) and pellet only (black), fueling. The pellet arrival in (b), (c), (e) and (f) is indicated by light blue lines.

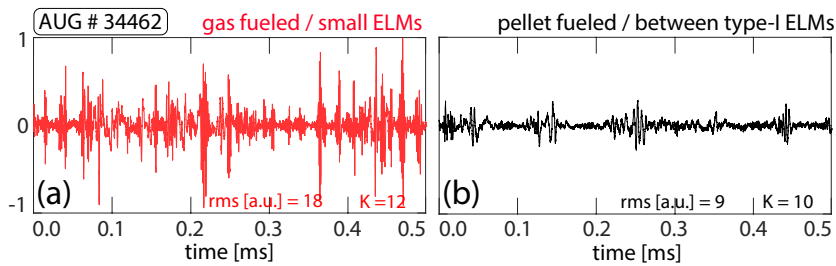


**Fig. 3.6:** Real part of the Doppler backscattering signal, measured at  $\rho_{\text{pol}} = 0.99$ ; (a) during 0.5 ms in the small ELMs phase (b) in 0.5 ms in between type-I ELMs.

a divertor current amplitude of  $\sim 5$  kA (shown by two black lines in figure 3.5(a)). As the gas puff is reduced and finally completely switched off, the type-I ELMs become larger (figure 3.5(b) & (c)) with losses in  $W_{\text{MHD}}$  reaching up to 10% while at the same time the small ELMs decrease in amplitude to  $\sim 2$  kA.

The pellet times are indicated in light blue and show no strict correlation between the pellet injection time and the appearance of a large type-I ELM. Direct pellet triggering can be observed for some ELMs while others are clearly not triggered. This is in agreement with previous findings [62] of a so-called lag time at high collisionalities, i.e. a time after an ELM in which a pellet is not able to trigger an ELM.

A significant change in filamentary transport at the foot of the pedestal has been observed on MAST [130] when comparing type-I ELMs to type-II ELMs. Such a change is also present in AUG #34462, as can be seen in Doppler backscattering (DBS) measurements just inside the separatrix ( $\rho_{\text{pol}} \sim 0.99$ ). Figure 3.6 shows the real part of a 500  $\mu\text{s}$  long time slice of the DBS signals measured in the gas-only (a) and the pellet-only phase (b). For the small ELM dominant regime (gas fueling, red),

the DBS signal shows large bursts in amplitude. These bursts are in the range of 40 – 80 kHz and are much more frequent than in between type-I ELMs later in the discharge (pellet fueling, black) [131]. More investigations are needed to clarify the change in the turbulent transport between both ELM regimes as this suggests a correlation with the filamentary transport in the scrape-off layer. This will be explored further in chapter 7.

In summary, the three cases with different particle fueling scenarios described above, show a clearly different ELM behaviour, while the plasma shape is kept constant and the pedestal profiles, with the exception of the density around the separatrix and in the scrape-off layer, are very similar. An elevated separatrix density leads to strong fluctuations or small ELMs in between some low amplitude large ELMs. The reduction of the separatrix density increases the large ELM amplitude and the small ELM fluctuations decrease in size. This behaviour is also seen in the measurements of the Doppler reflectometer.

Several more experiments comparing pellet and gas fueling were done at ASDEX Upgrade in addition to the discharge shown in detail in this section. Three different pellet velocities and two different pellet sizes were explored with the aim of keeping a constant pedestal top density and matching the rate of the gas fueling by variation of the pellet frequency. The measured data suggest neither a dependence on the pellet size nor the pellet velocity on the ELM behaviour. This missing correlation between pellet parameters and ELM triggering was also found for the lag-time mentioned above [62].

### 3.2.2 Predictive Modeling

A predictive scan using the IPED stability code [100] was performed in which  $n_{e,sep}$ , was varied independently with respect to the pedestal top density in order to understand the effect that the separatrix density has on the maximum stable pedestal top pressure  $p_{ped} = p_{e,ped} + p_{i,ped}$ .

Figure 3.7 shows this scan as grey dots with 5% error bars and with three specific examples for  $n_{e,sep} = 3.2 \times 10^{19} \text{ m}^{-3}$  in green,  $n_{e,sep} = 3.9 \times 10^{19} \text{ m}^{-3}$  in magenta and  $n_{e,sep} = 4.8 \times 10^{19} \text{ m}^{-3}$  in orange. The maximum pedestal top pressure in figure 3.7(a) does not change in these cases. However,  $p_{ped}$  increases by  $\sim 10\%$  when  $n_{e,sep}$  is slightly changed by varying the out-most (at  $\rho_{pol} = 0.99$ ) density gradient  $\nabla n_{e,sep}$ , i.e. shifting the maximum gradient slightly inward (see changes comparing magenta and blue profile).

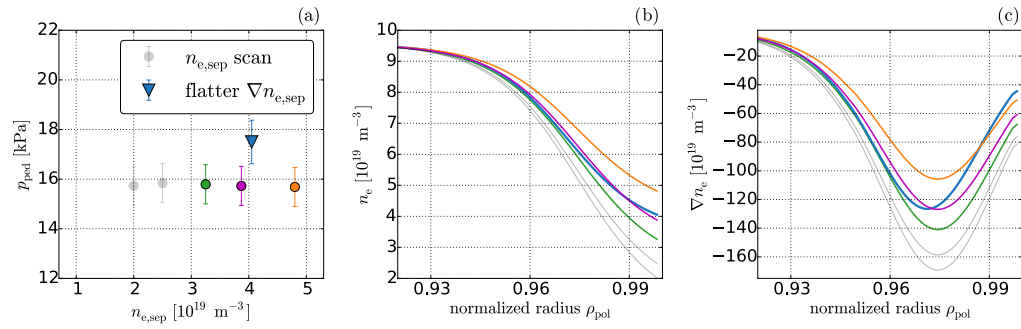


**Fig. 3.7:** Predictive stability scan with the IPED code (a) with corresponding electron density profiles (b) and electron density gradient  $\nabla n_e$  (c).

This behaviour can be explained by the fact that the region with steep gradients is narrower and shifted inward, providing better stability against PB modes (less space for modes to grow) and consequently allowing for higher pedestal top values.

As explained in section 2.6, IPED does not run with separatrix geometry, and the region included is restricted to the closed flux surfaces. The model considers ideal MHD modes, with mode numbers ranging between 1 and 70. When an unstable mode is found, a mode structure covering the entire gradient region will be returned. This is the main focus of the IPED code. An actual calculation of the stability of the  $n = \infty$  ballooning mode has not been done in this case. Such calculations are shown in chapter 6 using the HELENA code.

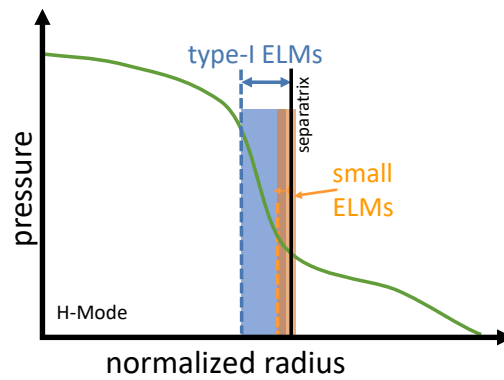


**Fig. 3.8:** Sketch of the relevant regions for type-I ELMs and small ELMs depicting the narrowing of the pedestal.

### 3.3 Chapter Summary

- Small ELMs and type-I ELMs can appear simultaneously.
- Small ELM stability is dominated by the separatrix conditions as  $n_{e,sep}$  is the most significant quantity.
- In high collisionality plasmas no strict correlation between pellets and ELM triggering is found.
- IPED predicts higher pedestal top pressure and therefore higher stability against type-I ELMs for pedestals narrowed by small ELMs (see figure 3.8).



# Ballooning Model

“ Every explanation is after all an hypothesis.

— Ludwig Wittgenstein  
Philosopher

*Parts of this chapter have been published in [106].*

In this chapter the change of dominant ELM type with a slight change of the plasma shape is described. This is further explored by analyzing the peeling-ballooning stability of this so-called  $z$ -shifted phases and the pellet experiments from the previous chapter. In conclusion a ballooning model is presented, extending the  $j$ - $\alpha$  peeling-ballooning stability diagram with the inclusion of the separatrix conditions.

## 4.1 Plasma Shape Changes: The $z$ -shift

The AUG small ELM recipe [39, 43] suggests that closeness to double-null is crucial for small ELMs to occur. To further examine this dependence, a set of experiments was conducted, starting from a small ELM regime with constant gas puff and shifting the plasma slowly downwards, away from the double-null configuration.

In figure 4.1 time traces of a discharge exhibiting this downward shift are shown. Following the procedure described in the previous chapter, a small ELM phase with a high gas puff and an upwards shift of the plasma is achieved by creating a close to double-null shape at 3.0 s. After 3.0 s the stored energy  $W_{\text{MHD}}$  stays constant at 0.8 MJ (figure 4.1(a), blue) and the ITER confinement time scaling factor  $H_{98(y,2)}$  is around 1.1 (figure 4.1(a), orange). The NBI and ICRF heating power (figure 4.1(b), red and green) was kept constant (neutral beam sources dropped for short periods due to the high density, with no lasting impact on the plasma parameters 2.2 s and 5.0 s). The ELM behaviour is shown in the outer divertor current in figure 4.1(c). The plasma density measured with Thomson scattering stays constant and the gas puffing rate (figure 4.1(d) in dark blue) is not changed after 3.0 s. The vertical ( $z$ ) position of the magnetic axis is shown in purple in figure 4.1(d) being

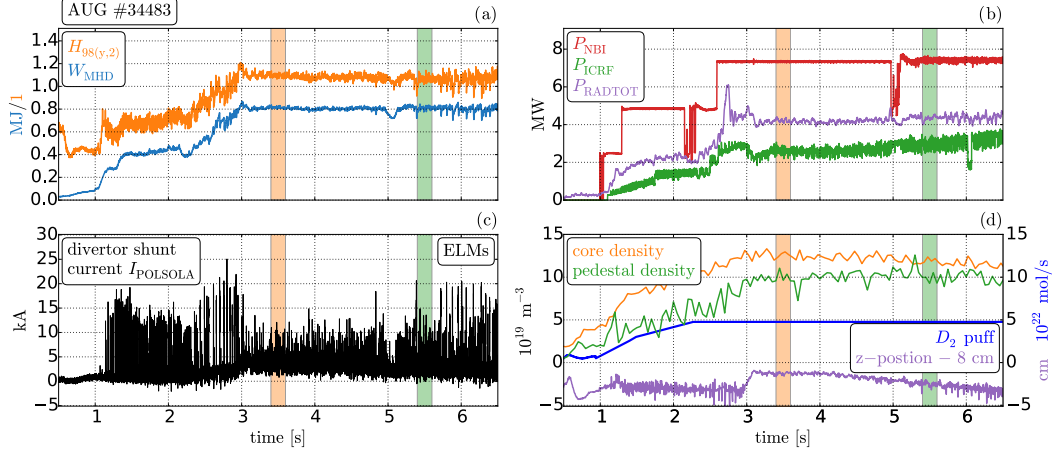


**Fig. 4.1:** Time traces of (a) stored energy ( $W_{\text{MHD}}$ ) and H-factor ( $H_{98(y,2)}$ ), (b) heating power of neutral beams ( $P_{\text{NBI}}$ ) and wave heating ( $P_{\text{ICRF}}$ ) as well as radiated power ( $P_{\text{RAD}}$ ), (c) outer divertor shunt current as ELM indicator and (d) core (green) and pedestal electron density (orange) measured by the Thomson scattering diagnostic, deuterium gas puff (dark blue) and the  $z$  position of the magnetic axis shifted by  $\sim 1.5$  cm (purple).

shifted downwards from 4.0 s onward. Gradually larger ELMs reappear changing the dominant ELM characteristics.

In figure 4.2 the plasma shapes of the two time windows indicated in figure 4.1, that were calculated with CLISTE are depicted. The top of the plasma changes significantly as the magnetic axis is shifted downwards by 1.5 cm while the lower X-point remains in the same position. This downward shift of the magnetic axis also changes the plasma elongation from  $\kappa = 1.688$  to  $\kappa = 1.673$ . The midplane radial difference of the two separatrices  $\Delta r_{\text{sep}}$  as a measure of closeness to double-null is increased from 12 mm to 17 mm, which represents a shift of the second separatrix from  $\rho_{\text{pol}} = 1.011$  to  $\rho_{\text{pol}} = 1.019$ . Another parameter that is influenced by downward  $z$ -shift is the triangularity. The upper triangularity is reduced from  $\delta_{\text{upper}} = 0.317$  to 0.285 by around 10%. As seen by the non changing lower X-point, the lower triangu-

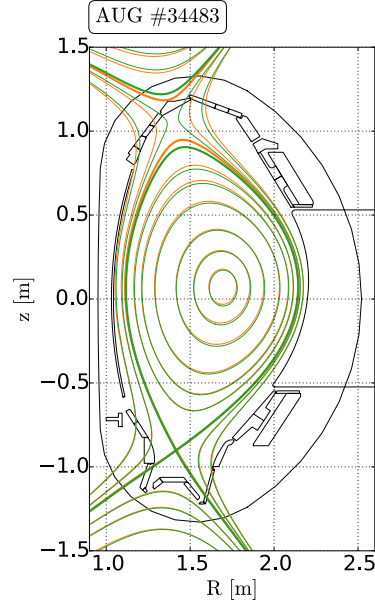


**Fig. 4.2:** Equilibria of the two time windows defined in figure 4.1 comparing the  $z$ -up (orange) and the  $z$ -down (green) position.

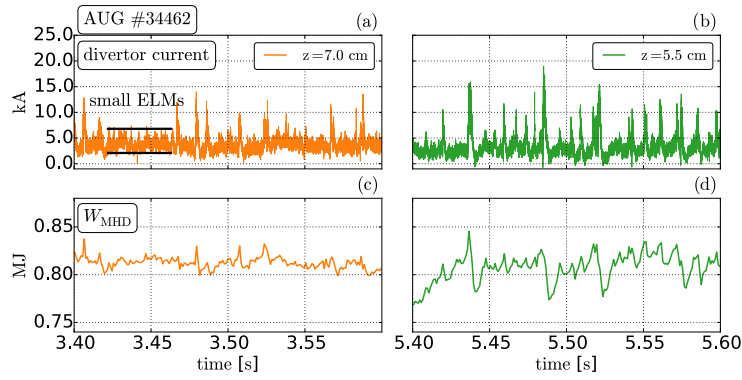


**Fig. 4.3:** Divertor current (a),(b) and stored Energy  $W_{\text{MHD}}$  (c),(d) of the two time windows defined in figure 4.1, comparing the plasma shapes shown in figure 4.2.

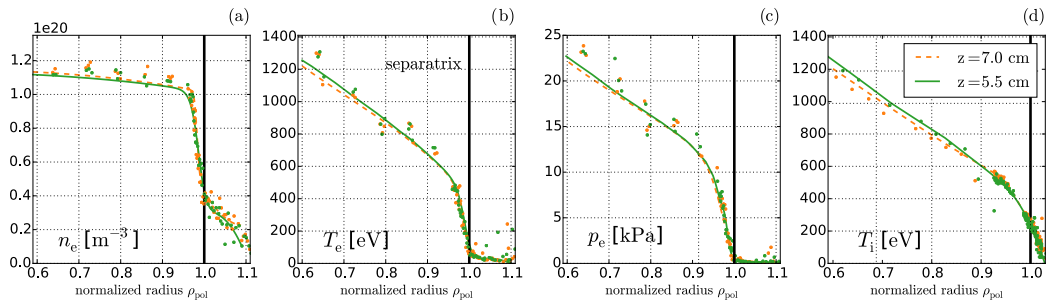


**Fig. 4.4:** Kinetic plasma profiles during the time windows indicated in 4.1 (orange  $\sim 3.5$  s and green  $\sim 5.5$  s) Edge profiles of electron density, electron temperature, electron pressure and ion temperature for the two different phases indicated in figure 4.1, in which the magnetic axis of the plasma is shifted from 7.0 cm (orange) to 5.5 cm (green) (figure 4.2).

larity stays constant within the margin of error (increases  $\sim 1\%$  from  $\delta_{\text{lower}} = 0.423$  to 0.428).

Figure 4.3 shows the divertor current ((a),(b)) and  $W_{\text{MHD}}$  signals ((c),(d)) for the small ELM case ( $z = 7.0$  cm in orange) and the mixed case ( $z = 5.5$  cm in green). The small ELMs dominate the transport in between some irregular large ELMs for the case with the higher position (orange). At the lower plasma position (green), larger type-I ELMs reappear. Additionally the small ELM amplitude decreases from  $\sim 5$  kA to  $\sim 3$  kA and the large ELM size increases from  $\sim 10$  kA to  $\sim 20$  kA. The reappearance of the large ELMs is best seen in the big drops in stored energy that are on the order of 10%.

Figure 4.4 shows a comparison of edge (a) electron density, (b) electron temperature, (c) electron pressure and (d) ion temperature profiles for the two phases representing  $z$  positions at 7.0 cm (orange) and 5.5 cm (green) also indicated in figure 4.1. While the ELM behaviour does change (figure 4.3), as the gas fueling is kept constant, the

kinetic profiles remain unchanged inside the uncertainties given by the scatter of the data. This is in contrast to the profiles shown in figure 3.4 of the previous chapter, where a distinct difference around the separatrix density was visible. The mtanh function was used to fit the profiles from Thomson scattering and charge exchange diagnostics, and the experimental error of the profiles shown in figure 4.4 is very similar to the one in 3.4 and has been omitted here for better visibility.

This experimental scans together with the change in separatrix density of the previous chapter, show that the separatrix density is a necessary but not sufficient criterion for the existence of small ELMs. The previous set of experiments (section 3.2.1) aimed at decoupling the pedestal top density ( $n_{e,\text{ped}} \sim 11.5 \times 10^{19} \text{ m}^{-3}$ ) and the separatrix density by changing from gas fueling ( $n_{e,\text{sep}} \sim 4.0 \times 10^{19} \text{ m}^{-3}$ ) to pellet fueling ( $n_{e,\text{sep}} \sim 2.0 \times 10^{19} \text{ m}^{-3}$ ), showing a small ELM dominant phase at high separatrix density. In this second set of experiments (section 4.1) however, a small change in the plasma configuration led to a reappearance of larger type-I ELMs, without a change in the kinetic edge profiles ( $n_{e,\text{sep}}$  stayed at  $4.0 \times 10^{19} \text{ m}^{-3}$ ).

## 4.2 Peeling-Ballooning Stability in small ELM Regimes

To understand the transition from type-I to small ELMs dominated phases and vice versa, the first step is to analyze the pedestal in the frame of ideal peeling-ballooning (PB) modes. Therefore the work-flow described in [132] was used to calculate the linear ideal stability boundary for the different cases. In figure 4.5 the operational points of all 5 instances described in the previous section is shown, including 15% error bars, and keeping the color code from the previous chapters. All operational points lie very close to their respective ideal peeling-ballooning stability boundary.

The two regimes with dominant small ELMs (orange '7.0 cm' and red 'gas fueling') show the highest normalized pressure gradient  $\alpha$ , with  $\alpha = 5$  and also the highest edge current density  $j_{\phi\text{max}}$ . The explanation for smaller ELMs at higher collisionality being due to the effect of a reduced edge current density [118] is therefore not applicable in the presented cases. The correlation between edge current density and normalized pressure gradient is not easily broken [133]. This has been explained, as the neoclassically driven current density is influenced by two effects that go in opposite directions. The increased collisionality reduces the drive while the density gradient provides a stronger drive than the temperature gradient. It seems counter-intuitive that the small ELM points lie close to the type-I ELM boundary, but it is

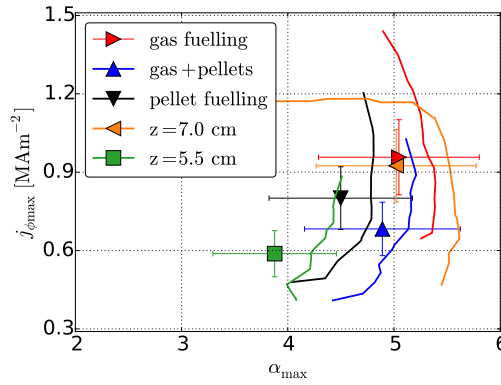


**Fig. 4.5:** Peeling-ballooning stability diagrams of discharges #34462 and #34483 (edge plasma current density  $j$  vs. normalized pressure gradient  $\alpha$ ) for all analyzed time windows.

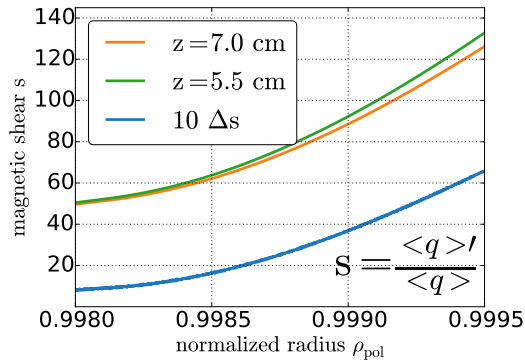


**Fig. 4.6:** Flux surface averaged magnetic shear  $s = q'/q$  for the two phases defined in figure 4.1. For better visibility the difference of the shear profiles  $\Delta s$ , plotted in blue, is magnified by a factor of 10.

likely that the changes in stability parameters are too small to be identified outside of experimental uncertainties.

### 4.3 Influence of the magnetic Shear close to the Separatrix

The strong dependence of the small ELM fluctuations on the separatrix density suggests, that they are very localized modes near the separatrix. For AUG plasmas it has been reported [134] that the so-called H-mode density limit, an operational limit of the plasma density depending on the plasma current, is correlated with the stability of modes at the separatrix.

The pressure gradient acts as a drive and determines the ballooning stability of such modes while the magnetic shear stabilizes them, see  $s$ - $\alpha$  diagram in [87, chapter 5.2.2]. As no significant change in the pressure gradient is found for the  $z$ -shift experiments (compare profiles in figure 4.4), the analysis focuses on the evaluation of the magnetic shear.

In figure 4.6 the flux surface averaged magnetic shear  $q'/q$  at the very edge of the plasma shows higher shear values for the lower plasma position. The derivative of the safety factor  $q'$  is calculated here as  $q' = \frac{dq}{d\rho_{\text{pol}}}$ . To see if the effect is due to flux expansion, a factor  $\frac{d\rho_{\text{pol}}}{dR}$  can be taken into account to compute  $\frac{dq}{dR}$ . This factor turns out to be lower for the lower shear case and higher for the case with the higher shear. This therefore amplifies the difference of the shear profiles shown in figure 4.6. The safety factor profiles for this analysis were taken from CLISTE equilibria with a high resolution of 256x512 and extrapolated close to the separatrix under the assumption that the profile has a pole of order 2 at the separatrix meaning  $q \propto 1/(\rho - 1)^2$ . The so-called local magnetic shear [135] also shows differences when comparing the two  $z$ -shift cases. The analysis there is more complex as it depends on the poloidal angle. More detailed results are presented in chapter 6. A local change of ballooning mode stability due to distortion of the local magnetic shear has also been reported in ASDEX Upgrade experiments with external magnetic perturbations [34].

## 4.4 Schematic small ELM Model

From the presented experiments and simulations in the previous chapters the following picture emerges: As observed in experiments small ELMs and type-I ELMs can occur simultaneously. On the one hand for standard ELM-ing pedestal models [26, 136, 137], linear peeling-ballooning theory can describe the existence of global type-I ELMs, where the pressure gradient is set by some transport limitation and the critical pedestal height and width by PB stability limits. The stability and magnitude of the small ELMs, on the other hand, are influenced by local parameters. As small scale localized turbulent structures can drive ballooning modes [138], small ELMs might be such ballooning modes that are localized near the separatrix. These modes are radially very narrow as they have high toroidal mode numbers and are driven by the local pressure gradient and stabilized by magnetic shear. Increased density leads to increased transport by such modes [138]. For high enough separatrix density they can create large particle transport locally, flattening the gradient and effectively

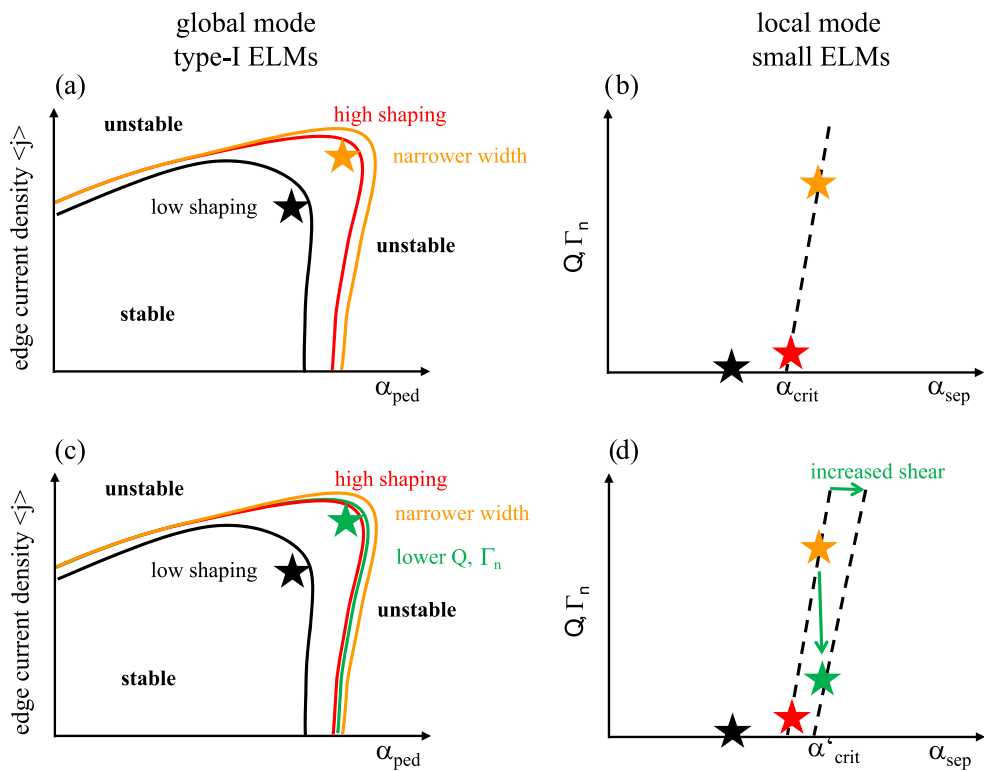


**Fig. 4.7:** Schematic description of small ELM occurrence. Type-I ELM mechanism on the left (a) and (c), small ELM mechanism on the right (b) and (d) (color coding analogous to the experiments).

narrowing the pedestal width, which in turn increases the stability against global PB modes and therefore type-I ELMs.

This emerging picture is demonstrated schematically in figure 4.7, making use of the PB  $j$ - $\alpha$  diagram and extending it with a heat- or particle flux diagram with a critical separatrix gradient. Figure 4.7(a) depicts the low triangularity type-I ELM case with its operational point close to the stability boundary in black. The critical pressure gradient  $\alpha_{\text{crit}}$  (figure 4.7(b)) at the separatrix is not yet reached for these cases. Here, type-I ELMs are the only limiting instability and small ELMs do not play a significant role. The stability boundary is shifted towards higher  $\alpha_{\text{ped}}$ , for higher triangularity shown in red. The normalized pressure gradient at the separatrix,  $\alpha_{\text{sep}}$ , at the same time, reaches the critical gradient and drives ballooning modes unstable. The increase of the pressure gradient at the separatrix is only possible with an increase in density, as the temperature is limited by parallel heat transport to the divertor plates (2-point model). An increase in  $\alpha_{\text{sep}}$  leads to even higher transport, indicated by the orange star (figure 4.7(b)), visible as small ELMs with increasing amplitude, which keeps the pressure gradient around the separatrix close to the small ELM critical stability limit. This region therefore contributes less to the total pressure gradient of the global type-I ELM, effectively narrowing the pedestal width. A steeper pressure gradient can be tolerated by this narrower pedestal, and the stability boundary is shifted to higher  $\alpha_{\text{ped}}$ , indicated in orange (figure 4.7(b)). The operational point is then far enough from the peeling-ballooning stability boundary and no type-I ELMs occur. For increasing values of the magnetic shear, e.g. due to a small downward shift of the plasma position, the critical gradient at the separatrix,  $\alpha_{\text{crit}}$ , will shift towards higher values. This in turn stabilizes the small separatrix located ELMs and decreases the transport they cause, as indicated by the green star in figure 4.7(d). A higher  $\alpha_{\text{crit}}$  and the reduced transport of the small ELMs increases the effective pedestal width. A wider pedestal allows for lower  $\alpha_{\text{ped}}$  and this, in turn, moves the PB boundary to lower values, leading to a reoccurrence of the type-I ELMs (green in figure 4.7(c)).

## 4.5 Chapter Summary

- Slight changes in the  $z$  position of the magnetic axis of a small ELM dominated plasma lead to a reappearance of type-I ELMs.
- Peeling-ballooning stability analyses show all operational points close to the stability boundary, with the small ELM dominated cases having the highest normalized pressure gradients and current densities.
- The  $z$ -shift influences the magnetic shear very close to the separatrix of the CLISTE equilibrium.
- A schematic model with a critical gradient at the separatrix, can explain the observed phenomena in addition to peeling-ballooning theory.



## Small ELM Studies in TCV

” *Repetition makes us feel secure and variation makes us feel free.*

— **Robert Hass**  
Poet

*Parts of this chapter have been published in [107]*

In this chapter the results of a series of experiments, conducted in TCV and aimed at disentangling the role of plasma fueling, plasma triangularity and closeness to the double-null (DN) configuration for the onset of a small ELM regime are summarized. It is not clear whether future machines such as ITER will be able to operate in a small ELM regime. A multi machine approach for the study of small ELMs can widen the achievable parameter range and therefore improve extrapolations to ITER. The ITER base line scenario is compared to small ELM operational parameters in section 5.1. As seen in the previous chapters for ASDEX Upgrade, the necessity of a large density at the separatrix is also demonstrated for TCV in section 5.2, while in section 5.3, the crucial role of the plasma shape is reported. A physical interpretation confirming the prominent role of the magnetic shear is given in section 5.4.

### 5.1 The ITER Baseline Scenario and small ELMs

To achieve its goals, as discussed in chapter 1.2, ITER will need to operate in the H-mode confinement regime, specified within the ITER baseline scenario (IBS) [139] for which the key parameters are shown in figure 5.1. An attractive solution to overcoming the limitation of type-I ELMs is to operate in the H-mode confinement regime with small ELMs such as type-II or grassy ELMs [36, 112, 41, 21], for which the good confinement is maintained and similar to the type-I ELM regime.

As discussed in section 1.2.2, historically a distinction was made between type-II and grassy ELMs: Type-II ELMs are observed when the plasma density, the edge safety factor and the triangularity are increased, moving the plasma close to a double-null (DN) configuration. Additionally a broadband fluctuation in the range of 30 –

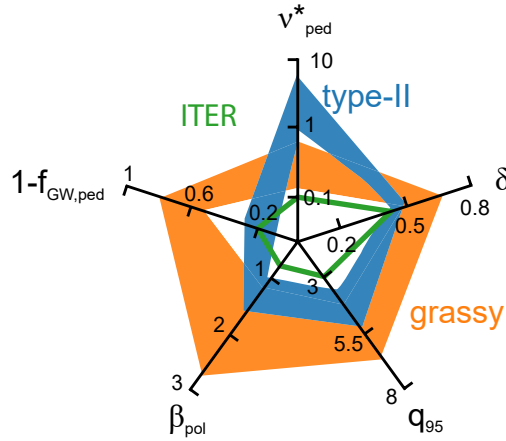


**Fig. 5.1:** Comparison of operational parameters for the ITER baseline scenario with type-II and grassy ELMs. From top left clockwise: Greenwald fraction  $f_{GW,ped}$ , pedestal top collisionality  $\nu_{ped}^*$ , triangularity  $\delta$ , safety factor at the plasma edge  $q_{95}$  and the plasma pressure normalized to the poloidal field  $\beta_{pol}$ .

50 kHz, observed in the magnetics, microwave reflectometry and electron cyclotron emission diagnostic up to the pedestal top ( $0.7 < \rho_{pol} < 0.95$ ), was reported to accompany the type-II ELM regime [43]. Grassy ELMs were reported on JT-60U with high triangularity and increased edge safety factor, but at lower Greenwald density fractions and therefore low collisionality, closer to ITER-relevant values. The distinction between type-II (blue) and grassy ELMs (orange) is highlighted in figure 5.1 where the typical values of the IBS key parameters are shown in green.

Due to the high current, the ITER baseline scenario has a low poloidal beta. The high pedestal top temperature leads to a very low collisionality and as the fusion power of a tokamak scales inversely with the safety factor squared, ITER aims for a low  $q_{95}$ . Both small ELM scenarios occur at too high pedestal top collisionalities, edge safety factors and plasma pressures normalized to the poloidal field. It is not clear whether the IBS parameters are the deciding quantities that need to be fulfilled to achieve a small ELM regime or if other key ingredients, e.g. separatrix conditions, as suggested in the previous chapter, are more important. It is also of great importance to decide whether a small ELM regime would be achieved in ITER for varying plasma parameters. Hereafter, the distinction between type-II and grassy ELMs is dropped intentionally and both are called small ELMs.

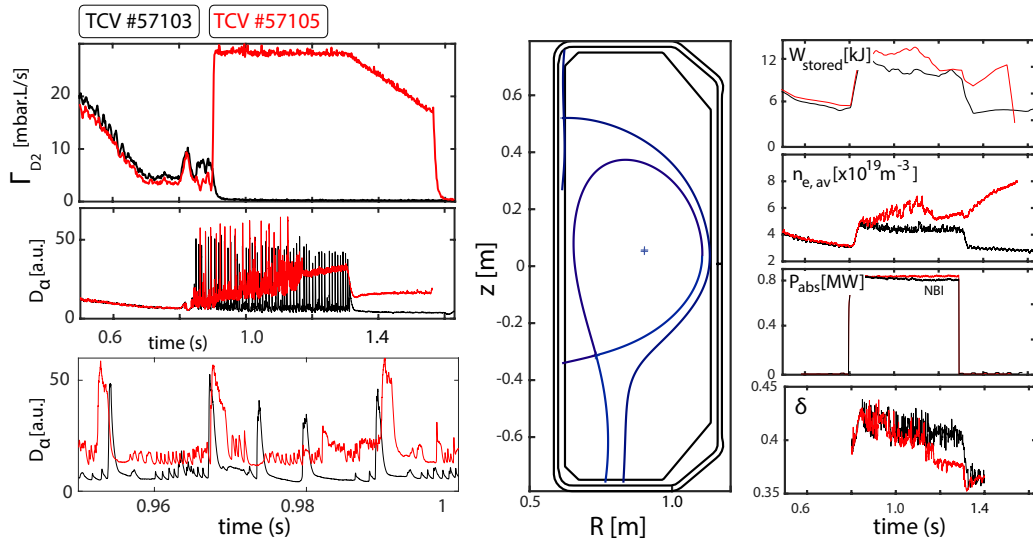


**Fig. 5.2:** Overview of TCV shots #57103 ( $\Gamma_{D_2} = 0$ ,  $H_{98y2} = 1.13$ ) and #57105 ( $\Gamma_{D_2} = 28 \text{ mbar} \cdot \text{ls}^{-1}$ ,  $H_{98y2} = 1.06$ ) showing how type-I ELMs frequency is reduced with strong fueling.

## 5.2 Gas Fueling Scan in ELMy H-mode

Obtaining a reliable type-I ELMy H-mode scenario in TCV is usually achieved with the following parameters: Lower Single Null,  $I_P = 140 \text{ kA}$ ,  $B_T = 1.4 \text{ T}$ ,  $\kappa = 1.5$ ,  $\delta = 0.38$ ,  $\Delta_{\text{sep}} = 24 \text{ mm}$ ,  $q_{95} = 4.5$ ,  $P_{\text{NBI}} = 1 \text{ MW}$  ( $P_{\text{L-H}} \sim 0.7 \text{ MW}$  at  $n_{e,\text{av}} = 3 \times 10^{19} \text{ m}^{-3}$ ). A plasma discharge with these parameters is depicted in figure 5.2 for TCV #57103 (black traces). The plasma density remains constant with zero gas fueling after 0.9 s by sufficient recycling from TCV’s carbon wall. The ELMs are monitored with a photo diode measuring the  $D_\alpha$  radiation along a vertical line-of-sight (see figure 2.5). The recently upgraded Thomson scattering system [69] is utilized to obtain the pedestal profiles fitted with a modified mtanh function [140] and shifted in such a way that  $T_{e,\text{sep}} = 50 \text{ eV}$  (see section 5.4). Further investigations on the effect of gas fueling and impurity seeding on the pedestal structure and the energy confinement have made use of this scenario [141, 142].

As seen in the AUG experiments in the previous chapters, operation at sufficiently large density at the separatrix ( $f_{\text{GW,sep}} \sim 0.3$ ) is a key ingredient to achieve a small ELM regime. This can be controlled via gas fueling. Starting from the reference type-I ELM regime, a mix of type-I and small ELM has been realized in TCV with a scan in deuterium fueling on a shot to shot basis [141, 142]. Figure 5.2 shows a summary of TCV #57105 for the largest fueling rate (red traces). The following observations can be made as the  $D_2$  flow increases, (Table 5.1):

**Tab. 5.1:** Summary of fueling scan of type-I ELMy H-mode in TCV with  $q_{95} = 4.5$ ,  $\delta = 0.4$ ,  $P_{NB} = 1$  MW.

$\Gamma_{D2}$ (mbarl/s)	$f_{ELM}$ (Hz)	$\frac{\Delta W}{W}$ (%)	$T_{e,ped}$ (eV)	$W_{MHD}$ (kJ)	$P_{rad}$ (kW)	$f_{rad,core}$ (%)
0	103±21	11±1	203±12	10±0.3	187±7	34±3
5	109±29	10±2	144±9	11±0.4	190±13	32±6
15	96±38	11±3	185±5	12±0.4	230±13	30±4
28	65±14	12±1	147±7	13±0.5	239±12	31±3

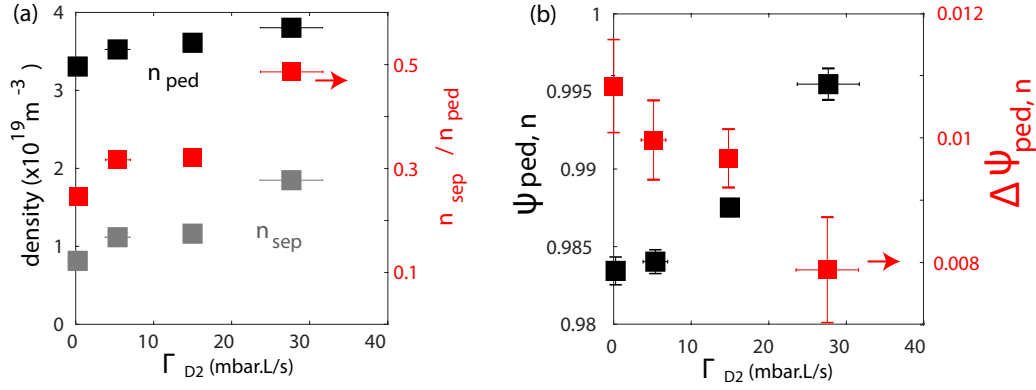


**Fig. 5.3:** Main results of the D<sub>2</sub> fueling scan (a) Pedestal density (black), separatrix density (gray) and their ratio (red), (b) Pedestal locations (black) and widths (red).

1. The relative loss energy  $\Delta W/W$  remains around 11% while the type-I ELM frequency decreases by a factor of 2.
2. An increasing recycling level might be indicated by the rise of the baseline level of the  $D_\alpha$  signal.
3. The small ELM frequency, in between the type-I ELMs increases and is typically around 2.5 kHz.

The reduced type-I ELM frequency hampers the plasma density control and it therefore increases with time, eventually leading to an L-mode back transition. The relative energy loss for each small ELM is below 1% which corresponds to the diagnostic resolution. No clear correlation is found between the variations in pedestal top pressure and the changes in the plasma stored energy when the fueling rate is varied [141]. The density increases faster at the separatrix compared to the pedestal top. The ratio  $n_{e,sep}/n_{e,ped}$  is therefore increased by a factor of 2 from 0.25 to 0.5 (figure 5.3(a)). No significant carbon accumulation in the plasma core is observed, despite the fact that the wall recycling is increased. This leads to a reduced fraction of core radiation with gas fueling.

With increased fueling the density pedestal shifts outward together with a reduction of the pedestal widths (figure 5.3(b)). Both effects lead to a reduction of the peeling-

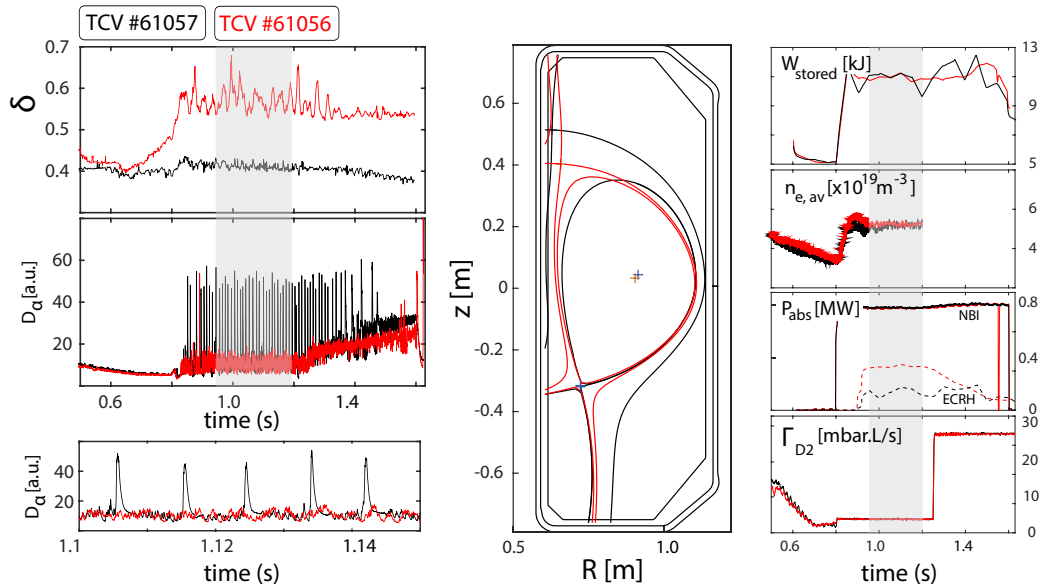


**Fig. 5.4:** Overview of TCV #61057 ( $\delta = 0.4 \Leftrightarrow \Delta_{\text{sep}} = 24 \text{ mm}$ , black) and #61056 ( $\delta = 0.54 \Leftrightarrow \Delta_{\text{sep}} = 3 \text{ mm}$ , red) showing how type-I ELMS are fully stabilized close to a DN configuration.

ballooning stability for type-I ELMS. A so-called high field side high density front that has been reported on AUG for similar plasmas [132], is not found in these discharges. This might be due to the TCV open divertor geometry and could be investigated further with the TCV divertor baffles [143].

In the set of discharges examined no broadband turbulence has been observed with the magnetic probes. Although in a different study, a signature of turbulence in the frequency range of 20 – 40 kHz in the magnetics was found for a similar fueling scan with plasmas at higher triangularities [141]. These discharges also show a transition to a mixed ELM regime.

### 5.3 The high Triangularity small ELM Regime at TCV

Plasma shapes with a high triangularity are crucial to obtain small ELM regimes [144, 41, 145, 43]. In order to study the shape dependence on the dominant ELM type, two discharges (LSN,  $I_P = 170 \text{ kA}$ ,  $B_T = 1.4 \text{ T}$ ) have been performed with changes in the upper triangularity while keeping all other parameters constant. As shown in figure 5.4 the upper triangularities change from  $\delta_u = 0.1$  (#61057,  $\delta = 0.38$ ,  $\Delta_{\text{sep}} = 24 \text{ mm}$ ) to  $\delta_u = 0.32$  (#61056,  $\delta = 0.54$ ,  $\Delta_{\text{sep}} = 3 \text{ mm}$ ). For the high

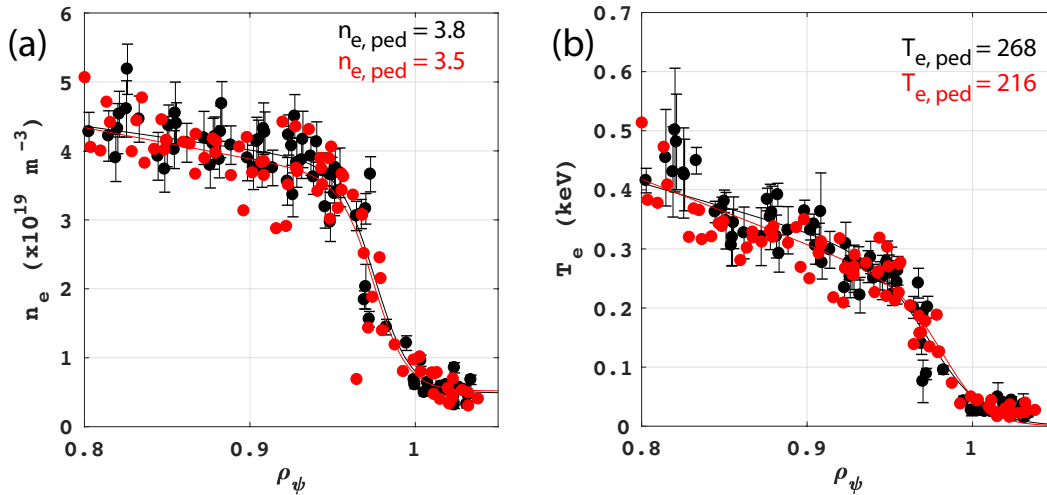


**Fig. 5.5:** Kinetic profiles from the Thomson scattering diagnostic for TCV #61057 ( $\delta = 0.4$ , black) and #61056 ( $\delta = 0.54$ , red) together with the associated *mtanh* fits.

triangularity discharge, a small ELM regime with controlled plasma density has been achieved.

The heating mix of both plasmas consisted of 1 MW of NBI plus 0.75 MW of X3 ECRH. The  $D_2$  gas flow was kept constant at 3.8 mbar · ls at the L-H transition leading to a Greenwald fraction of  $f_{GW,ped} \simeq 0.35$ . The medium triangularity discharge exhibits large type-I ELMs ( $f_{ELM} = 100$  Hz,  $\Delta W/W \sim 10\%$ ) while in the high triangularity discharge, small highly frequent ELMs for which  $\Delta W/W < 1\%$  appear.

In both discharges, the fueling at 1.25 s was increased by a factor of 8, leading to an increase of the plasma density, up to an H-mode density limit disruption, for the high triangularity case. For the medium triangularity shape, the density increases due to a decreasing type-I ELM frequency leading to a back-transition to L-mode similar to the discharges described in section 5.2.

The density is well controlled in both discharges and the stored energy stays the same for both triangularities. Figure 5.5, shows the temperature and density profiles, again measured by the Thomson scattering system and fitted with the modified *mtanh* function. The profiles for both discharges agree remarkably well, even though the data are selected in the [75%-90%] phase of the type-I ELM cycle while they are time averaged for the small ELM case. Some plasma and pedestal parameters are compared in Table 5.2.

As the relative energy loss per ELM is lower, a reduction of the peak heat loads at the targets is an expected benefit of the small ELM regime. A preliminary analysis of the heat loads at the outer strike point has been performed from infra-red measurements

**Tab. 5.2:** Plasma and pedestal parameters comparing the type-I and small ELM regimes at TCV averaged over the time window indicated by the shaded area in figure 5.4

ELMs	$q_{95}$	$\delta$	$\Delta_{\text{sep}}$ (mm)	$n_{e,\text{sep}}$ ( $\times 10^{19} \text{ m}^{-3}$ )	$\nu_{*,\text{ped}}$	$\beta_{\text{pol}}$	$f_{\text{GW,ped}}$	$W_{\text{MHD}}$ (kJ)	$H_{98y2}$
type-I	4.7	0.38	24	0.9	2.66	1.13	0.34	11	1.0
small	4.7	0.54	3	0.8	1.95	1.13	0.32	11	0.95

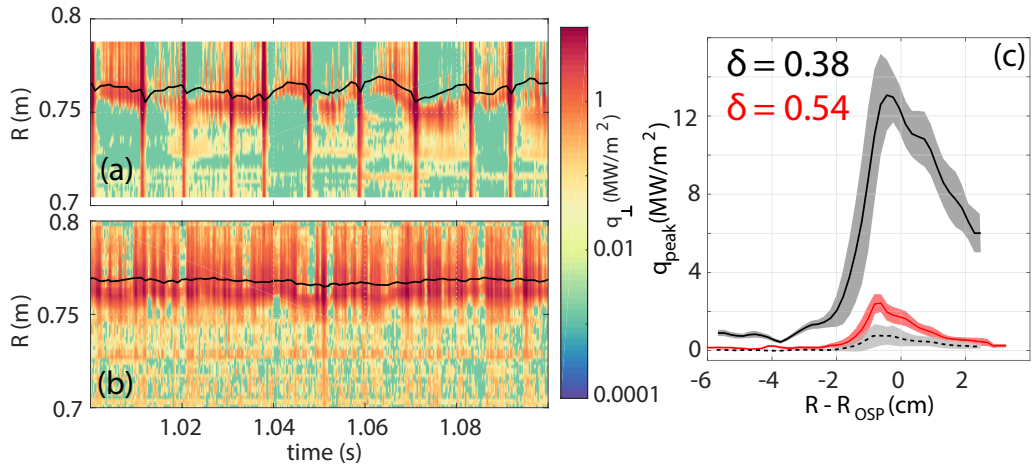


**Fig. 5.6:** Outer target heat loads measured with IR thermography for (a) TCV #61057 (type-I ELMs); (b) TCV #61056 (small ELMs); The black lines in (a) and (b) are the outer strike point locations according to the magnetic reconstruction; (c) Peak heat flux for type-I (black), small (red) and in between type-I ELMs (black; dashed).

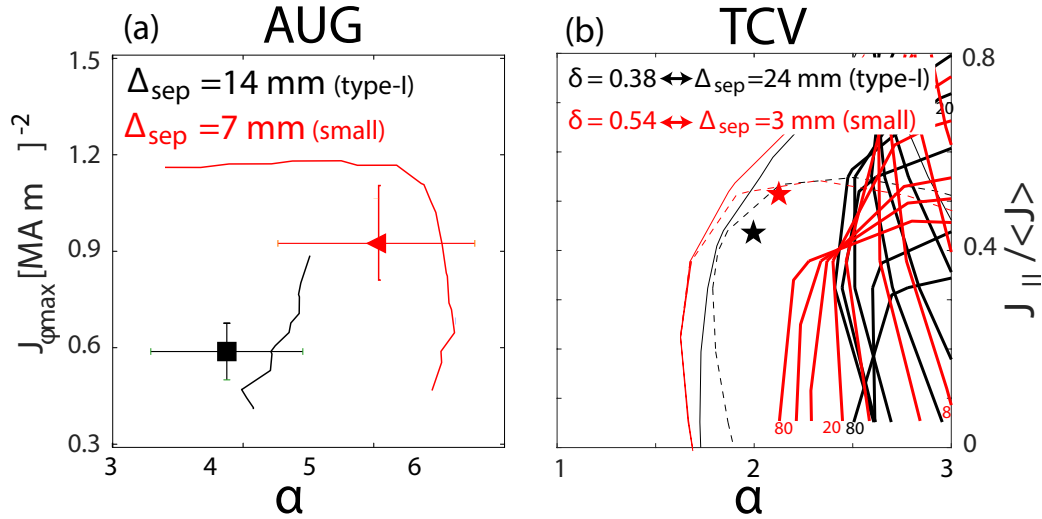


**Fig. 5.7:** Stability analysis of the pedestal; (a) Experimental points for AUG and peeling-ballooning boundary computed with HELENA and MISHKA; (b) Experimental points for TCV and peeling-ballooning boundary (thick solid), infinite  $n$  ballooning boundary at most unstable location (thin solid) and infinite  $n$  ballooning boundary at max.  $p'$  location computed (thin dashed) with CHEASE and KINX.

[146] for both plasmas. In Figure 5.6 a time trace of the perpendicular heat flux along the outer target is shown. The peak heat flux is reduced by a factor of  $\sim 10$  in the small ELM regime, reaching similar levels as the inter-type-I ELM periods. Another beneficial characteristic of the small ELM regime is that compared to the value evaluated in between type-I ELMs, the time averaged heat flux decay length  $\lambda_q$  for the small ELM case is about 20% larger (6.5 mm vs 5.5 mm). This can be seen as a possible indication of an enhanced cross-field transport in the SOL.

## 5.4 Physical Interpretation

The experimental results from TCV are consistent with those from ASDEX Upgrade reported in the previous chapters. They can be summarized as follows: a small ELM regime at high confinement can be achieved *if and only if* the separatrix density is large enough  $f_{GW,sep} \geq 0.35$  and the plasma shape is close to a double-null configuration. For further exploration of the commonalities and differences between the small ELM regimes found on both machines, their physical implications are discussed, starting with the pedestal stability analysis.

For the TCV plasmas discussed in section 5.3, the pedestal stability is analyzed using a combination of CHEASE and KINX [147] which is then compared to the AUG

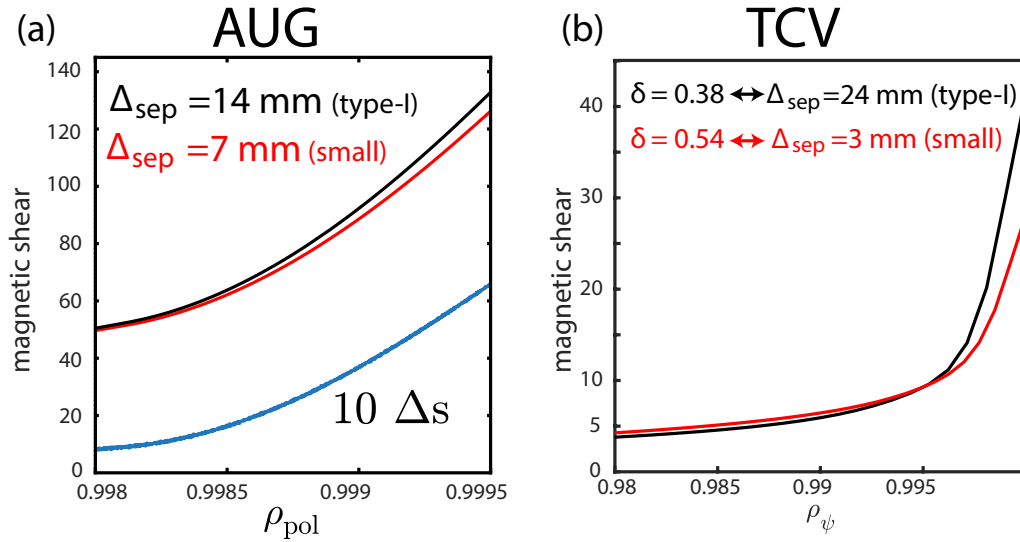


**Fig. 5.8:** Magnetic shear profiles (a) for AUG plasmas (as seen in figure 4.6) and (b) for TCV plasmas #61056 & #61057.

z-scan points obtained with HELENA and MISHKA (compare figure 4.5). As input for the codes, the experimental  $T_e$  and  $n_e$  profiles fitted with the modified mtanh function [140] are used. The absolute pedestal position cannot be determined within an accuracy of  $\sim 5$  mm due to the uncertainties in equilibrium reconstruction. Therefore the profile location relative to the separatrix is assigned based on power flow criteria [148]. Using the so-called two-point model [149],  $T_{e,sep} = 100$  eV is a typical value for the separatrix temperature in AUG H-modes [100]. Due to its smaller size, for TCV the model predicts a separatrix temperature of  $T_{e,sep} = 50$  eV. However, the pedestal location is not significantly impacted by uncertainty of 10-20% in  $T_{e,sep}$  as the gradients there are very steep. To match the temperature values of the model, at the separatrix, the  $T_e$  profiles are shifted and as the Thomson scattering diagnostic measures temperature and density at the same location,  $n_e$  is shifted accordingly. Figure 5.7 shows the  $j$ - $\alpha$  peeling-ballooning stability diagrams where  $j$  is the current density and  $\alpha$  is the normalized pedestal pressure gradient, both of which are evaluated in the middle of the pedestal. The experimental pressure gradient and current values for the type-I ELM cases (low shaping, black symbols), are close to the peeling-ballooning stability boundary. The intermediate- $n$  peeling-ballooning boundary expands considerably when the plasmas are strongly shaped towards DN and small ELMs are achieved. Nevertheless, the experimental pedestals are still close to this boundary, pointing to an increase in pressure gradient and possibly the edge current density in both devices when the small ELM regime is achieved.

As reported in section 4.3, changes in the magnetic shear at the plasma edge are correlated with changes in dominant ELM type. For the calculation of plasma equilibria, with high spacial resolution, the CHEASE code [150] was used for the TCV cases as it includes the pedestal bootstrap current self-consistently, similar to the CLISTE code that was used for the AUG cases. Figure 5.8 shows the flux surface averaged magnetic shear profiles for type I ELM dominated (black) and small ELM dominated (red) phases on both machines. The plasma shear at the very edge in the immediate vicinity of the separatrix is higher when the plasmas are further away from the double-null configuration (higher  $\Delta_{\text{sep}}$ ). For the AUG cases (5.8(a)) this increase is present outside of  $\rho \geq 0.999$  and might be influenced by the grid size of the equilibrium or when current diffusion is taken into account (see chapter 6). The TCV cases (5.8(b)) show this change further inside  $\rho \geq 0.996$  although there the overall plasma shapes differ more. Nevertheless, these results can be interpreted as further evidence that the small ELMs behave like ballooning modes with high toroidal mode numbers that are driven by the local pressure gradient and can be destabilized by a reduced magnetic shear [151, 152].

## 5.5 Chapter Summary

In this chapter, experiments conducted at TCV were compared to the findings of AUG in order to assess the effect of plasma fueling and plasma shape on the onset of small ELM regimes on a second machine. This clarified the key role of the two parameters, separatrix density and the magnetic shear in the immediate vicinity of the separatrix. In summary, for the emergence of a small ELM regime:

- The plasma density at the separatrix must be large enough ( $n_{e,\text{sep}}/n_{\text{GW}} \geq 0.3$ ) to drive a large ballooning transport and therefore to flatten the pressure profile near the separatrix which stabilizes type-I ELMs.
- The plasma triangularity has to be large enough ( $\delta \geq 0.35$ ) which, in practice, results in a magnetic configuration close to a double-null (DN), parametrized with  $\Delta_{\text{sep}}$ . This leads to a reduction in the magnetic shear in the extreme vicinity of the separatrix. As a consequence, its stabilizing effect on ballooning modes is weakened.

These critical parameters are compared for AUG, TCV and the expected values for ITER [153, 14] in Table 5.3. As the separatrix conditions seem to be crucial for the small ELM regimes, it is important to realize that not only the ITER plasma shape but also the separatrix parameters  $f_{\text{GW,sep}}$  and  $\nu_{\text{sep}}^*$  can be matched in present day

**Tab. 5.3:** Plasma and pedestal parameters for small ELM regimes in AUG and TCV, compared to parameters of the ITER baseline scenario assuming  $T_{e,\text{ped}} = 4 \text{ keV}$ ,  $T_{e,\text{sep}} = 0.2 \text{ keV}$ ,  $n_{e,\text{ped}} = 0.7 \times 10^{20} \text{ m}^{-3}$  and  $n_{e,\text{sep}} = 0.3 \times 10^{20} \text{ m}^{-3}$ .

	$q_{95}$	$\delta$	$\Delta_{\text{sep}}$	$\nu_{*,\text{ped}}$	$\nu_{*,\text{sep}}$	$f_{\text{GW,ped}}$	$f_{\text{GW,sep}}$
AUG (small ELM)	4.5	0.37	7 mm	$\sim 1.4$	$\sim 7$	0.82	0.3
TCV (small ELM)	4.5	0.54	3 mm	$\sim 2$	$\sim 10$	$\sim 0.35$	$\geq 0.1$
ITER	3.0	0.40	80 mm	$\leq 0.1$	$\sim 7$	0.6 – 0.8	0.25

tokamaks. A small ELM regime with good confinement might therefore be achievable in ITER. Nevertheless, since it is known that the ITER pedestal collisionality cannot be matched in present machines while keeping the same separatrix conditions, a better physical understanding of the onset of the small ELM regime is still needed for extrapolations to ITER and beyond.



# Stabilizing Effects in small ELM Scenarios

” *There is nothing so stable as change.*

— **Bob Dylan**  
Musician

The following chapter aims to explore three different elements relevant for plasma edge stability, namely the magnetic shear, the  $E \times B$  shear and the connection between the good and bad curvature region. Firstly in section 6.1, experiments with a modulation in the plasma current are evaluated which indicate a more complex behavior of the global magnetic shear  $s$ . This is further explored by comparing the magnetic shear of equilibrium reconstructions with and without current diffusion included. In addition four discharges of the  $z$ -shift type (see section 4) with a variation in edge safety factor are analyzed in section 6.2. The effects of the magnetic shear are shown in more detail in section 6.3 by means of comparisons with ideal ballooning stability calculations using the HELENA code. The 2D local magnetic shear [135] is introduced and compared for the four discharges and studied in more detail in the  $s$ - $\alpha$  parameter space.

The plasma shaping effect is investigated in section 6.4 in first results of JOREK simulations of small ELMs including the  $E \times B$  shear. The experimentally obtained  $E_r$  profiles and their gradient are compared as being the main component of the  $E \times B$  shear. Section 6.5 concludes the chapter with a depiction of the connection length between HFS and LFS midplane as an important parameter for ballooning stability. A summary of the results is given in section 6.6.

## 6.1 Modulation of the Plasma Current

The safety factor profile and therefore the magnetic shear can be influenced via the plasma current and the shape of the plasma. In this section, a plasma discharge with a modulation of the plasma current (AUG #34937,  $B_T = -2.5$  T,  $I_P = 0.6$  MA) is investigated in order to examine the influence of the current on the magnetic shear

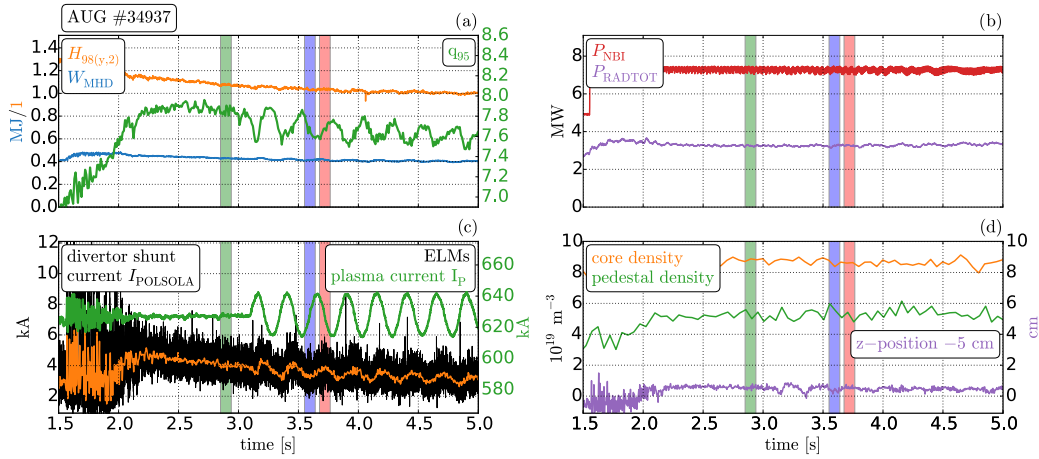


**Fig. 6.1:** Time traces of (a) stored energy ( $W_{\text{MHD}}$ ), H-factor ( $H_{98(y,2)}$ ) and safety factor ( $q_{95}$ ) (b) heating power of neutral beams ( $P_{\text{NBI}}$ ) as well as radiated power ( $P_{\text{RAD}}$ ), (c) outer divertor shunt current as ELM indicator (black) and plasma current with modulation (green) (d) core (orange) and pedestal (green) electron density measured by the Thomson scattering diagnostic, and the  $z$  position of the magnetic axis shifted by  $\sim 5$  cm (purple).

and to compare different methods of evaluating the shear. Figure 6.1 shows time traces of this discharge where a small ELM phase is achieved with a high gas puff and an upwards shift of the plasma to create a close to double-null shape at 2.0 s.  $W_{\text{MHD}}$  stays constant at 0.4 MJ (figure 6.1(a), blue) while the ITER confinement time scaling factor  $H_{98(y,2)}$  is around 1.0 (figure 6.1(a), orange) and the safety factor at 95 % flux (figure 6.1(a), green) is between 7.5 and 8 after 2.0 s. The NBI heating power (figure 6.1(b), red) was kept constant. The outer divertor current shows the ELM behaviour in figure 6.1(c). Figure 6.1(c) also shows the plasma current including the 4 Hz modulation with an amplitude of 12.5 kA on top of the constant 625 kA starting at 3.1 s. The plasma density (see figure 6.1(d) edge/green and core/orange) as well as the vertical ( $z$ ) position of the magnetic axis (shown as the purple time trace in figure 6.1(d)) stay constant from 2.0 s onward. The plasma current modulation changes the divertor current signal, modulating it with 4 Hz but with a phase shift. A minimum  $I_{\text{polSOla}}$  can be found at the rising flank of  $I_{\text{p}}$  (blue) and a maximum at the falling flank (red). A third time-point is marked in green before the current modulation for reference. The 4 Hz modulation can also be seen in the safety factor  $q_{95}$ , being in anti-phase ( $+180^\circ$ ) with  $I_{\text{p}}$ .

Figure 6.2 shows a comparison of radial magnetic shear profiles for the three time windows marked in figure 6.1. The shear of a high resolution CLISTE equilibrium reconstruction calculated using

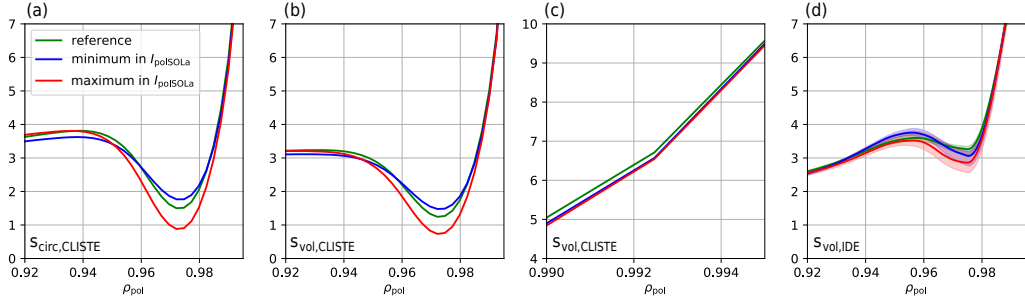


**Fig. 6.2:** Comparison of magnetic shear  $s$  calculated using different formulas ( $s_{\text{circ}}$  vs  $s_{\text{vol}}$ ), (a)-(b), and different equilibria (CLISTE vs IDE) (b)-(d). (c) shows a zoom to the very edge region of (b).

$$s_{\text{circ}} = -\frac{r}{q} \frac{dq}{d\psi} \quad \text{and} \quad s_{\text{vol}} = \frac{2V}{q} \frac{dq}{dV} \quad (6.1)$$

is depicted in figure 6.2(a) and (b), while (c) represents an enlargement of the edge region of (b). The equations have been adapted from equations 2.16 and 2.20 [154], while the latter was adapted to include the missing  $1/q$  dependence. No extrapolation has been done for these profiles, therefore they end at  $\rho = 0.995$ . The use of the two different formulae quantitatively changes the shear profile but the prominent features and trends stay the same. In the zoomed-in panel, the shear of the reference time window is marginally elevated compared to the two other windows. Figure 6.2(d) shows the magnetic shear using the  $s_{\text{vol}}$  formula for highly resolved IDE equilibria. The shaded areas represent the 95% confidence interval of the 200 ms time windows shown in figure 6.1. The inclusion of current diffusion, as done with IDE, broadens the edge current density peak. This leads to a shallower local minimum in the shear profile at the pedestal top  $\rho \sim 0.975$ .

The data suggest that the plasma current modulation affects the magnetic shear further inward compared to the  $z$ -shift (section 4.3) with neither a large change in the kinetic profiles nor the amplitude of the small ELMs. This could be due to the fact that in this high  $q_{95}$  discharge the critical ballooning parameter  $\alpha_{\text{crit}} \propto \frac{q^2}{B^2} \nabla p$  was already reached at a lower pressure gradient  $\nabla p$  and the plasma is deep inside the small ELM regime. As the modulation of the plasma current affects many quantities, further work is needed to decorrelate the different plasma parameters. The change of the shear suggests that the modulation technique is a promising way to investigate the  $s$ - $\alpha$  parameter space of small ELMs.

**Tab. 6.1:** Plasma parameters for four small ELM discharges of the  $z$ -shift type presented in chapter 4

shot #	$I_P$ MA	$B_T$ T	$q_{95}$	$P_{tot}$ MW	$P_{rad}$ MW	$\Gamma$ $\times 10^{22}$ mol/s	$f_{GW,ped}$	$\beta_N$	$H_{98,y2}$
34862	1.0	2.5	4.5	9.2	3.6	4.5	0.87	2.05	1.02
34939	0.8	2.5	5.9	8.8	3.9	1.4	1.00	1.70	0.90
34886	0.6	2.5	8.0	8.4	2.8	0.4	0.96	1.85	1.00
34879	0.6	2.0	6.4	5.0	2.0	0.4	0.87	1.82	1.02

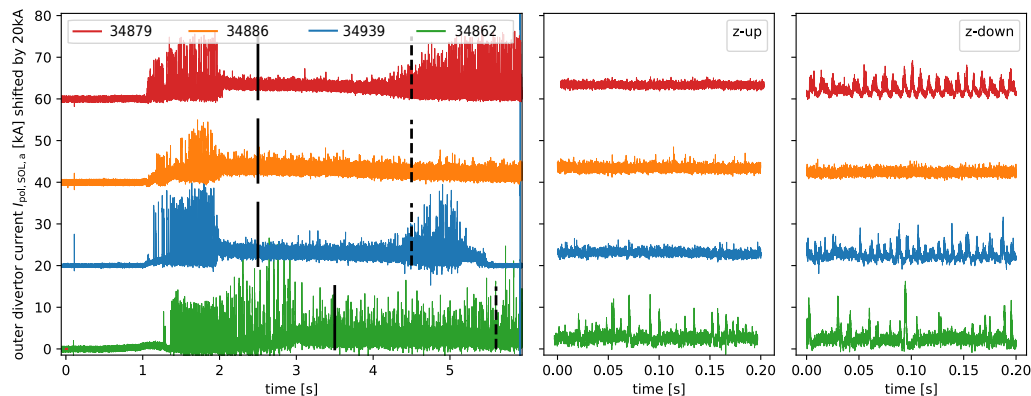


**Fig. 6.3:** Outer divertor current time traces for the four  $z$ -shift discharges offset by 20 kA for illustrative purposes. The solid and dashed lines mark the mid point of the regions of upper (z-up) and lower (z-down) vertical plasma position that are enhanced on the right side.

## 6.2 The $z$ -shift at different Safety Factors

In chapter 4, the so-called  $z$ -shift discharge was presented that showed a reappearance of type-I ELMs when shifting the vertical ( $z$ ) position of the plasma down and away from the double-null configuration. In order to further investigate the effect of the magnetic shear that is crucial for the balance between type-I ELMs and small ELMs, four more discharges of the same type have been performed on AUG. The goal was to analyze the effect of the  $z$ -shift in a broad range of safety factors while keeping the confinement factor  $H_{98,y2}$  and the normalized plasma pressure  $\beta_N$  as similar as possible by adjusting the input heating power and gas fueling levels accordingly. Table 6.1 shows the main plasma parameters of the four discharges. At high pedestal top Greenwald fraction  $f_{GW,ped} > 0.87$ ,  $\beta_N$  varies between 1.70 and 2.05 and the ITER confinement time scaling factor remained at around 1, except for #34939 where only 0.9 was achieved due to too much gas puffing.

The outer poloidal divertor current  $I_{polSOLa}$  signals of the four discharges are depicted in figure 6.3 including offsets of 20 kA for illustrative purposes. The small ELM shape is established at 3 s in the lowest  $q$  discharge (#34862) and at 2 s in

the other three discharges. 1 s later, the plasma  $z$  position is gradually ramped down. While the low  $q$  discharge has some type-I ELMs throughout, the other three discharges show clean small ELM phases without type-I ELMs. For the two medium  $q$  discharges (#34939 and #34879), the downward  $z$ -shift leads to a reappearance of type-I ELMs after 4 s, while for the high  $q$  case (#34886) the pure small ELM phase remains until the end of the discharge. This is best seen in the two zoomed panels on the right side of figure 6.3. The midpoint of these 200 ms time windows is marked in the left panel with a solid line defining the  $z$ -up position and a dashed line defining the  $z$ -down position.

The kinetic profiles of the discharges have been fitted with IDA [72] and used as input for high resolution equilibrium reconstructions including current diffusion with IDE [92]. Radial profiles of the safety factor  $q$ , the magnetic shear  $s_{\text{vol}}$ , the normalized pressure gradient  $\alpha$  (see equation 2.20) and the toroidal current density  $j_{\Phi}$ , extracted from these IDE equilibria, are depicted in figure 6.4. Solid lines represent the median profile of the  $z$ -up position including 95 % confidence intervals of the 200 ms time windows<sup>1</sup> while the dashed lines show the  $z$ -down position. The downward  $z$ -shift causes the  $q$  profile to flatten for  $\rho > 0.95$  in all four cases which in turn lowers the magnetic shear for the whole pedestal region. The normalized pressure gradient that is generally higher for the 1 MA discharge (green) increases for the two medium  $q$  discharges (blue and red) with the  $z$ -shift, while in the high  $q$  case it stays unchanged inside the uncertainties. The toroidal current

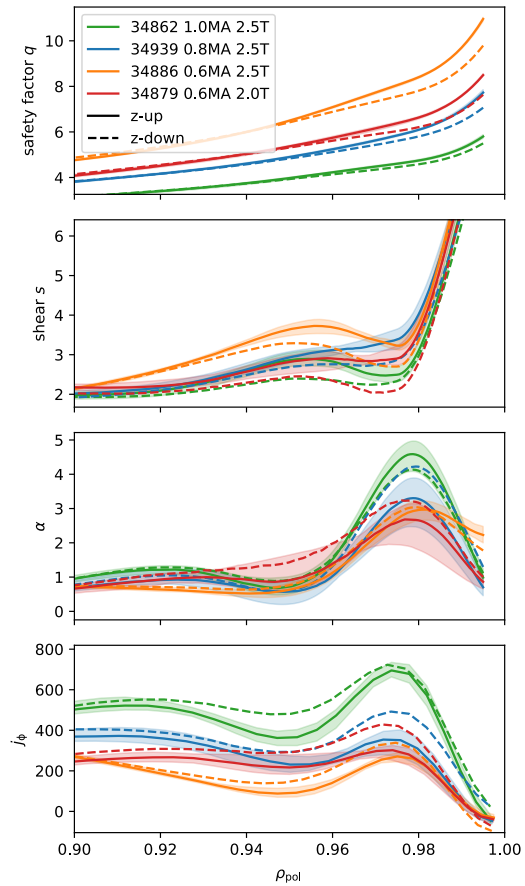


**Fig. 6.4:** Radial profiles of safety factor  $q$ , magnetic shear  $s$ , normalized pressure gradient  $\alpha$  and toroidal current density  $j_{\Phi}$  of four discharges similar to the one shown in figure 4.1 for various combinations of plasma current and toroidal field.

<sup>1</sup>The IDE reconstruction was done every 5 ms. A 200 ms time window therefore represents 40 points.

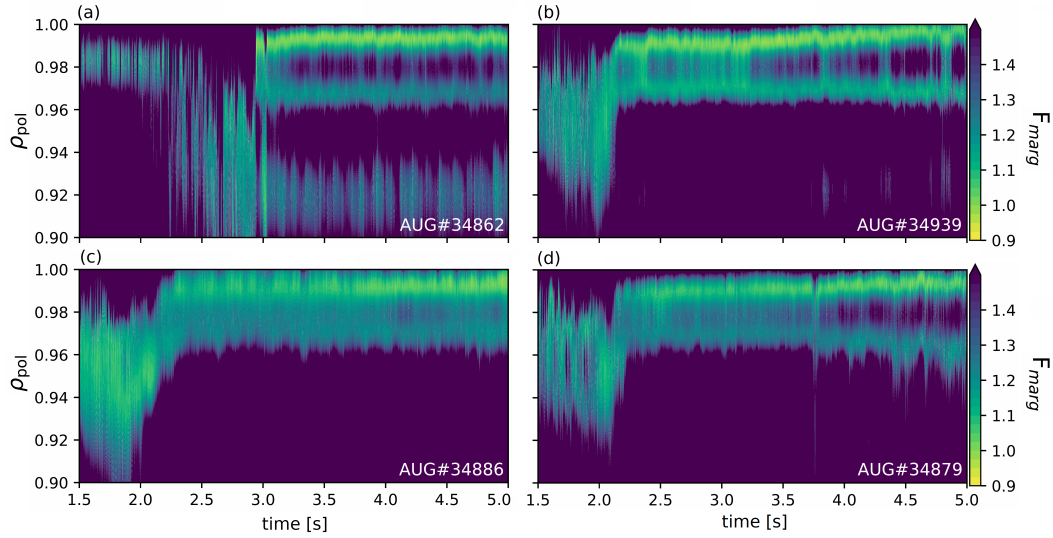


**Fig. 6.5:** Contour plots of the temporal evolution of the marginal stability  $F_{\text{marg}}$  of four  $z$ -shift discharges for different  $\rho_{\text{pol}}$ .

density (bottom panel) also changes in all four cases. With the downward  $z$ -shift the current density of the low  $q$  discharge increases inside the pedestal top ( $\rho < 0.96$ ); in the other three cases it is increased throughout the pedestal region.

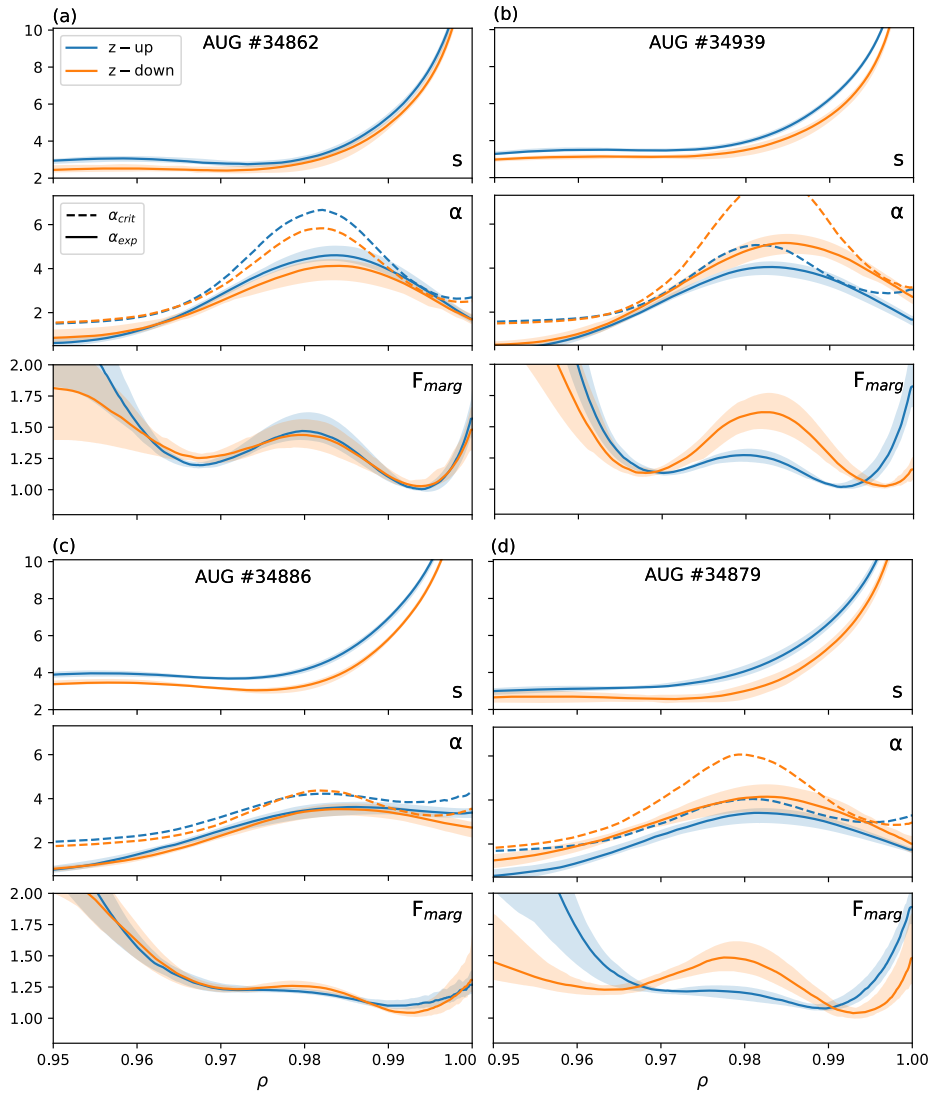
The ideal ballooning stability of the four discharges was calculated with HELENA which uses the IDE boundary as input and evaluates the Suydam stability criterion for ballooning modes [155] for every 5 ms time point of the IDE equilibrium. The output consists of radial profiles of the magnetic shear and the experimentally observed normalized pressure gradient  $\alpha_{\text{exp}}$ , as well as profiles for a critical normalized pressure gradient  $\alpha_{\text{crit}}$  at which the plasma would become ballooning unstable.

Figure 6.5 shows contour plots of the so-called marginal ballooning stability of the four discharges that is defined as

$$F_{\text{marg}} = \frac{\alpha_{\text{crit}}}{\alpha_{\text{exp}}}. \quad (6.2)$$

The temporal evolution of the marginal stability is plotted for different radial positions and shows some distinct features that can be summarized as follows: When the discharge evolves to the high shaping (3 s for 34862, 2 s for the lower current discharges), the plasma becomes ideal ballooning unstable close to the separatrix at  $\rho \approx 0.99$ . A second region that is close to the ideal ballooning boundary is the pedestal top at  $\rho \approx 0.965$ . In the steep gradient region at  $\rho \approx 0.98$ , the plasmas are more stable. After the  $z$  position is shifted downward, this region of stability becomes broader. The effect is best seen in the medium  $q$  shots (figure 6.5(b) and

(d)). Looking at these features in more detail, figure 6.6 shows radial profiles of quantities relevant for the ideal ballooning stability calculations. The four discharges at the  $z$ -up (blue) and  $z$ -down (orange) time windows are compared in 6.6(a)-(d), where the upper panel represents the magnetic shear, the middle panel the experimental (solid lines) and ideal ballooning critical (dashed lines) normalized pressure gradients  $\alpha_{\text{exp}}$  and  $\alpha_{\text{crit}}$  and the bottom panel depicts the marginal stability  $F_{\text{marg}}$ . The lines show the median of the data and the shaded regions represent the 95 % confidence interval of  $\pm 100$  ms. For both phases, as already shown in figure 6.5, the experimental pressure gradient profile comes very close to the critical one at  $\rho > 0.99$  leading to a minimum in  $F_{\text{marg}}$  for all discharges. The stability of the two medium  $q$  discharges in the steep gradient region, around  $\rho = 0.98$ , increases with the  $z$ -shift and the  $F_{\text{marg}}$  minimum moves outward. The difference in the magnetic shear of the re-evaluated profiles from HELENA are very small but the shear decreases within all four discharges with the downward  $z$ -shift. The behavior is counter intuitive as in a simple ballooning stability picture a lower magnetic shear should not lead to increased stability. The flux surface averaged quantities described in this section might not suffice to explain the change in ballooning stability as the shape change in the  $z$ -shift discharges is predominantly localized at the top of the plasma (see figure 4.2). The HELENA stability calculations take the whole plasma cross section into account and are sensitive to small shape changes. Therefore, in order to better understand and interpret the stability calculations, it is reasonable to look at 2D quantities such as the local magnetic shear.



**Fig. 6.6:** Radial profiles of the magnetic shear  $s$ , the experimental  $\alpha_{\text{exp}}$  and critical normalized pressure gradient  $\alpha_{\text{crit}}$  and the marginal stability  $F_{\text{marg}}$  from HELENA for the four  $z$ -shift discharges.

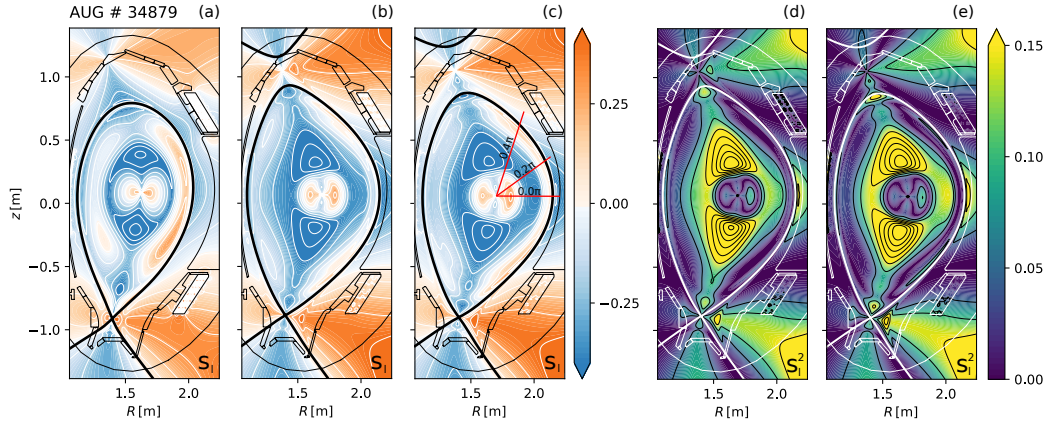


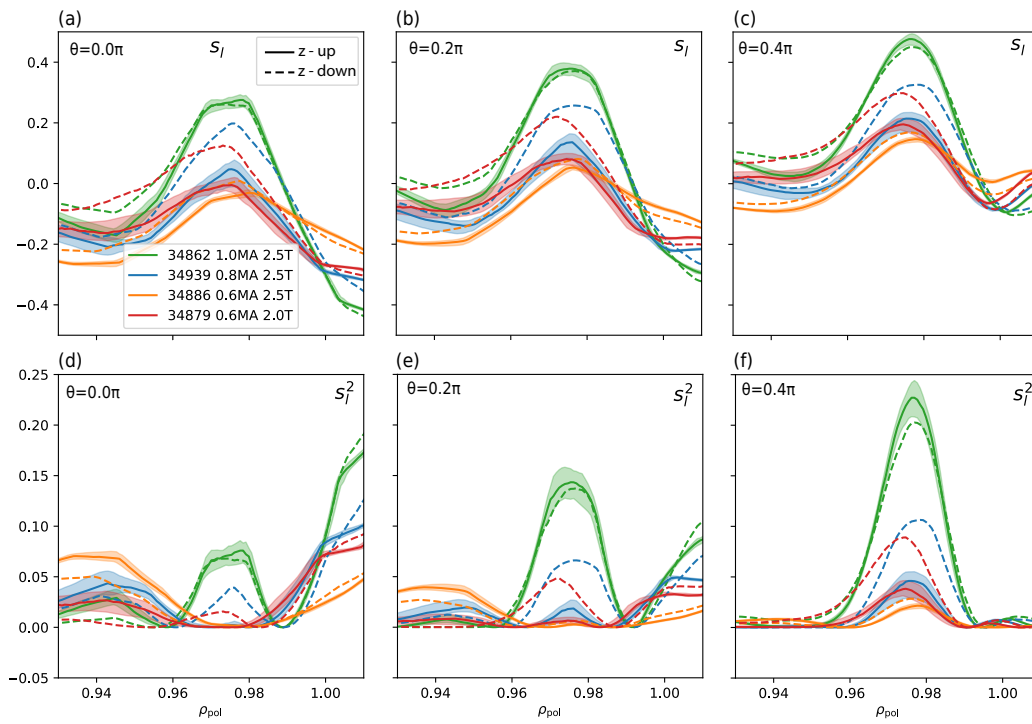
**Fig. 6.7:** Local magnetic shear  $s_{loc}$  [135] of AUG #34879, at (a) 1.5 s, (b) 2.5 s and (c) 4.5 s. (d) and (e) show the square of (b) and (c). Contours of constant  $s_{loc}$  and  $s_{loc}^2$  as well as the separatrix are depicted in black and white.

### 6.3 The stabilizing Effect of the Local magnetic Shear

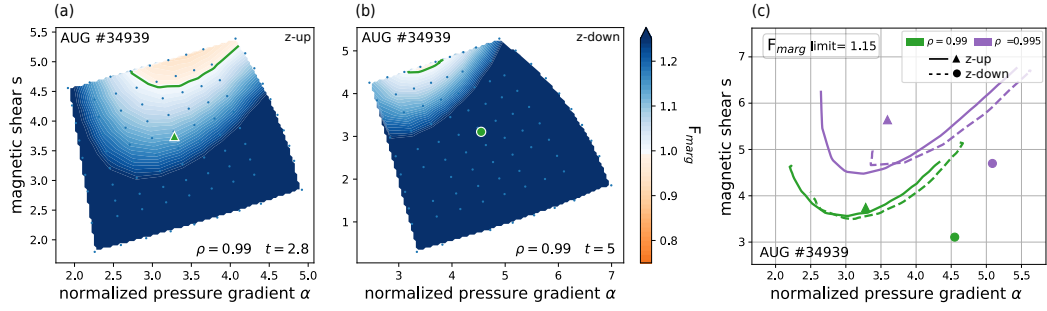
For a better understanding of the shaping effects in the  $z$ -shift discharges, the local magnetic shear  $s_l = -\mathbf{e}_\perp \cdot \nabla \times \mathbf{e}_\perp$  as defined in [135] was calculated. Here the unit vector  $\mathbf{e}_\perp$  is perpendicular to the local magnetic field direction and lies in the flux surface.  $s_l$  represents the local tilt of neighbouring flux tubes.

Figure 6.7 shows the local magnetic shear for AUG #34879 at different times during the discharge. At 1.5 s (figure 6.7(a)) the small ELM shape is not yet established and the plasma still exhibits type-I ELMs. Positive local shear is represented in orange and negative shear in blue while lines of constant shear are depicted by white contours and the separatrix is shown in black. The local shear is mostly negative inside the separatrix, except for the very core of the plasma and an elongated region at the edge around the midplane of both sides, but stronger on the LFS. With the high triangularity shape (figure 6.7(b)) this positive shear region is compressed closer to the separatrix but becomes wider again when the plasma is shifted down (figure 6.7(c)). As can be seen in the Mercier criterion (equation 2.15), the determining quantity for ballooning stability is not the sign of the shear but its magnitude. Therefore figures 6.7(d) and (e) depict  $s_l^2$  for the same time points as figures 6.7(b) and (c). As the shear crosses zero in the region above and below the LFS midplane, this region is visible as having low squared shear. The positive shear regions are only visible above and below the midplane in the  $s_l^2$  plots.

For a more quantitative approach figure 6.8 shows radial profiles of the local magnetic shear. Different colors depict the four different  $z$ -shift discharges. The solid



**Fig. 6.8:** Radial profiles of the local magnetic shear. (a)-(c) show the local shear  $s_l$  of the  $z$ -shift discharges for different poloidal angles (red lines in 6.7(c)). (d)-(f) show the squared local shear  $s_l^2$  for the same angles.



**Fig. 6.9:**  $s$ - $\alpha$  diagrams for AUG #34939: Marginal stability contours for (a) the upper ( $t = 2.8$  s) and (b) the lower  $z$  position ( $t = 5$  s). (c) shows the  $F_{\text{marg}} = 1.15$  contour for different radii represented by different colors and for the two time points represented by different symbols and line styles.

lines (including 95 % confidence intervals of a 100 ms time interval) represent the upper  $z$  position and the dashed lines the downward shifted one. The profiles of the local magnetic shear show a peak inside the separatrix with a zero crossing inside the separatrix for different poloidal angles (a)-(c). The peak size decreases with increasing safety factor values and increases for higher poloidal angles. For the higher  $q$  plasmas, the peak increases in size with the downward  $z$ -shift while for the low  $q$  discharge, it remains relatively constant. This might be due to the changing edge current density shown in figure 6.4. Another prominent feature appears when looking at the square of the local shear plotted in figure 6.8(d)-(f). The zero crossing of the local shear causes a minimum in the squared shear which is located at  $\rho = 0.99$ , the region that was found to be ideal ballooning unstable (see figure 6.5). The increase of the shear peak with the downward  $z$ -shift is also in line with the HELENA simulations showing a broader ballooning stability in the steep gradient region at  $\rho = 0.98$ .

To study the balance between pressure gradient drive and shear stabilization in more detail, HELENA also allows for calculations of ballooning stability diagrams in the  $s$ - $\alpha$  space. The results of such calculations for the  $q_{95} = 5$  discharge AUG #34939 are depicted in figure 6.9. The two left panels (a) and (b) represent contours of marginal stability at  $\rho = 0.99$ , which are calculated by HELENA on a grid in  $s$  and  $\alpha$  shown by the light blue dots. The marginal stability values at these points are then interpolated to get  $F_{\text{marg}}$  contours and therefore the stability boundary. Note, that this is the stability boundary for  $n = \infty$  ballooning modes only, not the one for coupled peeling-ballooning modes. Stable regions are shown in blue and regions with  $F_{\text{marg}} < 1$  are shown in orange. The experimental points are depicted using green symbols; a triangle for the high  $z$  position at  $t = 2.8$  s and a circle for the downward shifted  $z$  at  $t = 5$  s. Both points are ideal ballooning stable and while for

the upper  $z$  position the operation point lies in the connection region between first and second stability, the point for the downward shifted  $z$  moves further into the second stability region. This shift to second stability is also depicted in figure 6.9(c), showing the operational points and the stability boundary  $F_{\text{marg}} = 1.15$  for different normalized radii in different colors.  $F_{\text{marg}} = 1.15$  was chosen as a representative boundary for illustrative purposes due to the fact that the real boundary  $F_{\text{marg}} = 1.0$  is often very close to the simulation domain and therefore small. The upper  $z$  position ballooning boundary is depicted with solid lines and the operational points are marked as triangles. The lower  $z$  position boundary is shown using dashed lines and circles represent the respective operational points. For  $\rho = 0.995$  the points are located closer to the boundary, and in the upper  $z$  position the point lies inside the  $F_{\text{marg}} = 1.15$  contour, very close to the ballooning boundary. The operational points of both radii move to the second stability region for the downward shifted plasma. This results in a broader radial stability region (also seen in figure 6.5(b) & (d)) that might dampen the small ELMs and lead to a reappearance of large type-I ELMs.

## 6.4 The Role of the Electric Field

Recently, full type-I ELM cycles have been simulated with the JOEK code [104]. Using similar plasma parameters, JOEK simulations with lower heating power show smaller ELMs with less impact on the divertor. Figure 6.10 shows fluctuations of the electron density (a) and (d), the electron temperature (b) and (e) and the parallel velocity (c) and (f) during such simulated small ELMs. The two rows show a comparison of ELMs at low triangularity (top) vs high triangularity (bottom). While the low  $\delta$  simulations show a more peeling mode-like characteristic, the fluctuations in the high  $\delta$  case are concentrated on the LFS and the structures are poloidally smaller.

The simulation results are still preliminary, but they point to the role of the  $E \times B$  shear, as without it, JOEK is not able to reproduce ELM cycles of a small or large kind and can only simulate single ELM events [156].

The  $E \times B$  shear, or in other words the radial change of the  $E \times B$  velocity, can be defined as:

$$\omega_{E \times B} = -\frac{(RB_\theta)^2}{B} \frac{\partial}{\partial \psi} \left( \frac{E_r}{RB_\theta} \right). \quad (6.3)$$

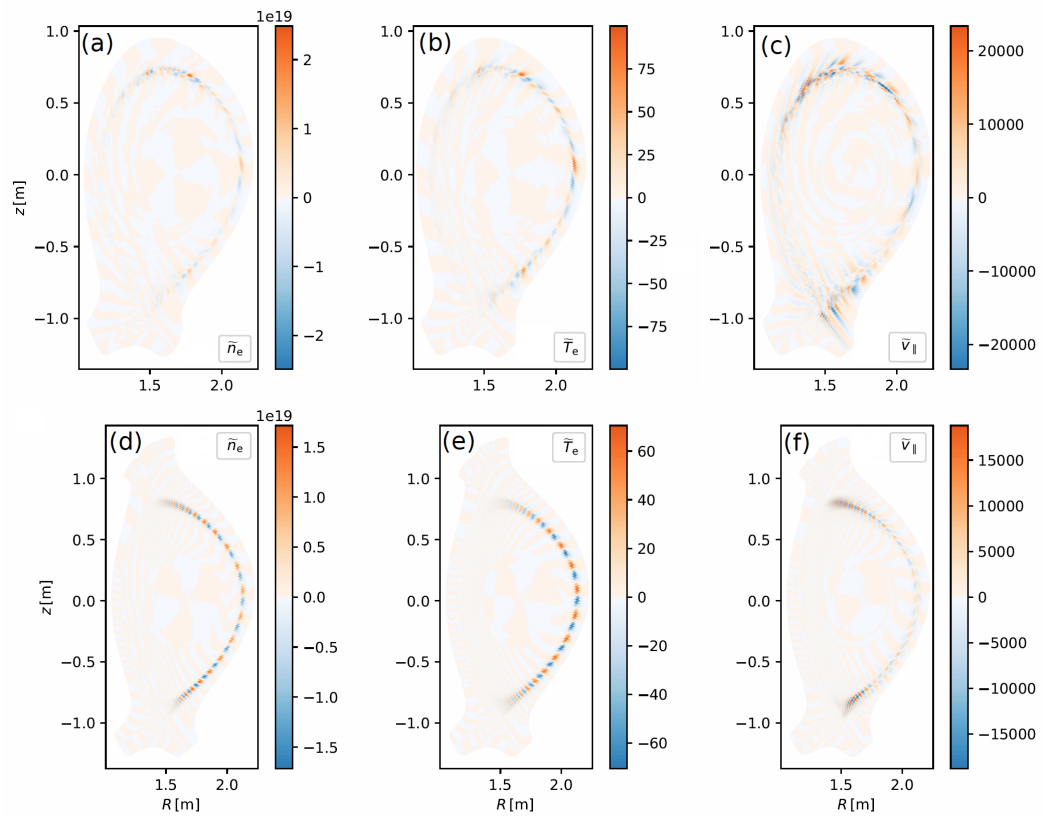


**Fig. 6.10:** JOREK small ELM simulations showing fluctuations of (a)&(d) electron density, (b)&(e) electron temperature and (c)&(f) parallel velocity 4 ms after the start of the simulation during the first ELM crash. The upper row shows a low upper triangularity simulation and the lower row has a high upper triangularity.

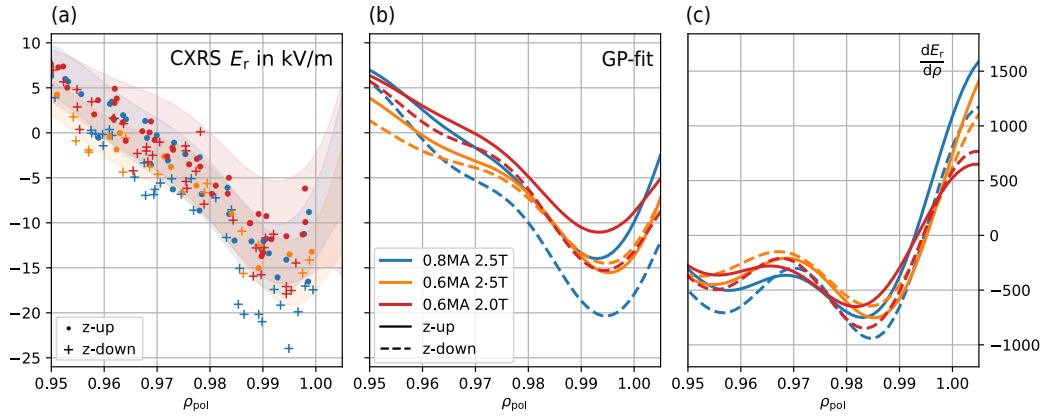


**Fig. 6.11:** The radial electric field of the four  $z$ -shift discharges and its gradient, where solid lines and circles represent the upper  $z$  position and dashed lines and crosses the lower  $z$  position. (a) shows the measured data points from CXRS including confidence intervals from the fit, (b) the Gaussian process fit and (c) the fitted gradient.

Its main ingredient is the gradient of the radial electric field which is notoriously hard to measure experimentally. It has been reported to suppress turbulent transport and is widely believed to be the main cause for the L-H transition [157, 158, 159].

To investigate its role in small ELM stability, the radial electric field  $E_r$  profiles for the three lower current  $z$ -shift discharges have been calculated from the line intensity and the poloidal and toroidal velocity measured by the AUG CXRS diagnostics using equation 2.5. The profile reconstruction for the high current discharge showed a minimum of  $E_r$  outside the separatrix, suggesting that the measurements might have been influenced by the type-I ELMs. The discharge has therefore been left out of this analysis.

The data points measured are shown in figure 6.11(a) as circles for the  $z$ -up and crosses for the  $z$ -down position. For better visibility only every fifth radial point is plotted. The experimental  $E_r$  data were fitted using Gaussian process (GP) regression within the proFit framework [160]. A squared-exponential kernel was applied together with additive Gaussian noise to represent random measurement errors (shaded areas in 6.11(a) for the  $z$ -up data). Figure 6.11(b) shows the fitted profiles for the  $z$ -shift discharges, where again solid lines denote the upper and dashed lines the lower  $z$  position. The discharge with the lowest heating power (#34879, red) has the shallowest minimum. Similar to the dominant ELM type, the  $E_r$  profile of the high  $q$  discharge (#34886, orange) remains unchanged when the  $z$ -position is shifted down, while for the medium  $q$  discharges (red and blue) the minimum becomes deeper. Figure 6.11(c) shows the radial gradient of the fitted  $E_r$  profile which is the defining quantity of  $\omega_{E \times B}$ . The gradient profiles also

have a minimum although further inside at  $\rho \sim 0.985$  which is at a similar position as the second stability region discussed in the previous section. The  $E_r$  gradients behave in a similar way to the  $E_r$  profiles. They become stronger with the  $z$ -shift for the medium  $q$  discharges and change slightly in the other direction for the high  $q$  discharge. An explanation for this behavior could be that the small ELMs flatten the pressure gradient which in turn causes a shallow  $E_r$  minimum. When the plasma is shifted down, the local shear stabilizes the steep pressure gradient region and the  $E_r$  minimum becomes deeper. The ballooning stability calculations presented in the previous section do not take the  $E \times B$  shear into account. As the  $E_r$  profiles and their gradients change significantly when comparing the clean small ELM phase with the phase where type-I ELMs reappear, the influence of the  $E \times B$  shear on small ELM stability cannot be disregarded.

## 6.5 The Connection between HFS and LFS

The JOREK simulations in figure 6.10 show a strong disconnection of the good and the bad curvature region for the high triangularity shape. The plasma shaping obviously has an effect on the connection length between the HFS and the LFS. To quantify this effect, the connection length between the midplane of the LFS and the HFS has been calculated using the IDE equilibria. This is shown in figure 6.12 for the four different discharges and two radial positions of the field line. The connection length decreases with the  $z$ -shift for all four cases. The change is largest for the high  $q$  discharge where the connection length at  $\rho = 0.99$  decreases by 23 % from 45 m at the start of the shift at 3 s to 35 m at 5 s. The relative decrease from 3 – 5 s is lower for the other cases, namely 20 % for 34879, 17 % for 34939 and only 9 % in 34862.

This decrease in connection length represents a stronger link of the good and bad curvature region at the  $z$ -down position which influences the overall stability of the pedestal and can therefore also influence the small ELM stability as well as the type-I ELM stability.

## 6.6 Chapter Summary

In summary, all three stabilizing quantities, (local) magnetic shear,  $E \times B$  shear and the connection length between good and bad curvature regions, change with the

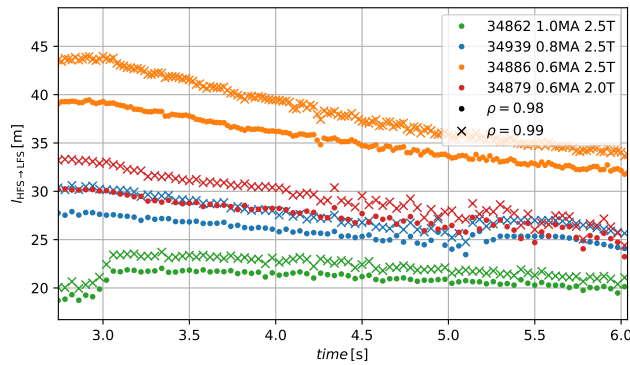


**Fig. 6.12:** Connection length from the LFS midplane to the HFS midplane. Different symbols represent different normalized poloidal radii  $\rho$ .

downward  $z$ -shift and the reappearance of the type-I ELMs, therefore none of the mechanisms can be excluded as a relevant ingredient for small ELM stability.

The key insights of this chapter are summarized as follows:

- A modulation of the plasma current influences the magnetic shear of the whole pedestal region.
- Taking current diffusion into account weakens the localized minimum in the magnetic shear.
- The  $z$ -shift discharges behave similarly for a wide range of safety factor profiles.
- Ideal ballooning stability calculations show an instability at the far plasma edge at  $\rho \approx 0.99$  and a region of increased ballooning stability where the pressure gradient is steepest.
- Calculations of the local shear show a minimum of the squared shear close to the separatrix and a peak further inside. This peak is stronger above the midplane and can explain the changes in ideal ballooning stability.
- The downward  $z$ -shift causes the operation point at different radial locations to shift away from the ballooning boundary into the second stability region.
- Preliminary small ELM simulations with the JOREK code including  $E \times B$  drifts show predominant ballooning-like fluctuations in a high triangularity shape.
- Radial electric field profiles were obtained from CXRS measurements and fitted using the Gaussian process fitting technique.  $E_r$  and its gradient change with the  $z$ -shift and might therefore influence the small ELM stability.

- The connection length between the HFS and LFS midplane changes significantly with the  $z$ -shift which can lead to a reconnection of good and bad curvature regions and therefore a reappearance of type-I ELMs.



# Small ELM Bursts and Filaments

” *From a little spark may burst a flame.*

— **Dante Alighieri**

Poet

The model proposed in chapter 4 consists of three main ingredients: the normalized pressure gradient at the separatrix  $\alpha_{\text{sep}}$ , the magnetic shear and the transport caused by the small ELM ballooning modes. The pressure at the separatrix can be influenced by changes in temperature and density. This chapter focuses on the behaviour of the small ELMs in ITER-relevant highly shaped, low  $q_{95}$ , AUG discharges with a large variation in heating power, gas fueling intensity and location and gives first insights into the resulting transport.

A set of discharges has been examined by investigating bursts in the signal of the He-Beam diagnostics that are found very close inside the separatrix. Furthermore, the magnitude of the fluctuation in divertor shunt currents signals is used as a measure for SOL transport. The dependence of the burst frequency and the divertor current fluctuations on different plasma parameters is analyzed to decide whether small ELMs are feasible for a future reactor scenario.

## 7.1 Burst Determination and Location

In the previous chapters, the region just inside the separatrix has been identified to determine whether a plasma discharge exhibits small ELMs or type-I ELMs. To influence this region experimentally, a set of 15 plasma discharges has been performed on AUG with the aim of analyzing the dependence of the small ELM regime on plasma heating and fueling. Most of the discharges were performed at ITER relevant safety factors of  $q_{95} \approx 3.6$  with a combination of 1 MA plasma current and 2.0 T toroidal field. To broaden the database, some higher safety factor discharges with either  $I_{\text{P}} = 0.8$  MA or  $B_{\text{T}} = 2.5$  T were included. The plasmas were all heated with a mix of NBI and ICRF heating and the power crossing the separatrix

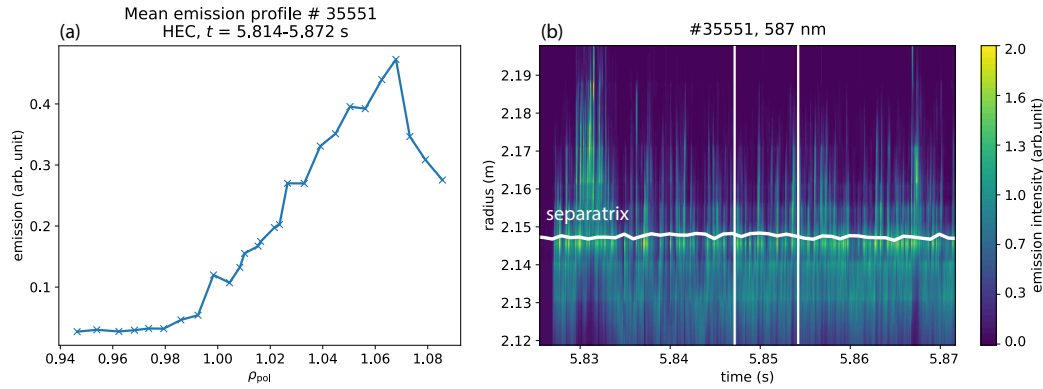


**Fig. 7.1:** (a) Mean emission profile of the helium beam between 5.814s and 5.872s (b) Time trace of emission intensity of all helium beam channels showing a maximum inside the separatrix.

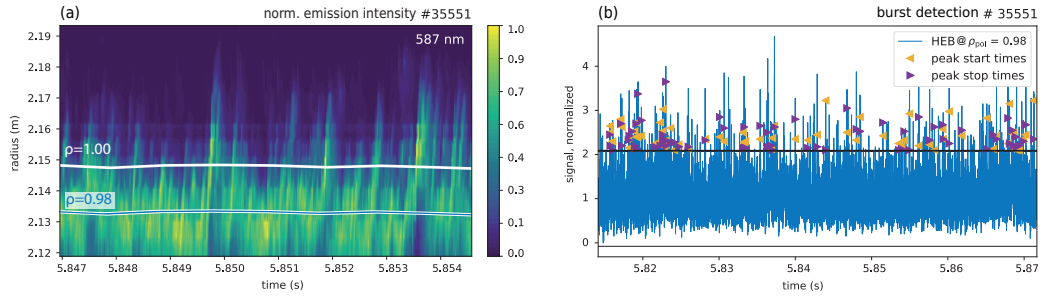
$P_{\text{sep}} = P_{\text{tot}} - P_{\text{rad}}$ <sup>1</sup> ranges from 5 – 12 MW. The large variation of gas puffing levels in the database ranges from  $0.5 - 6.0 \times 10^{22} \text{ e}^- \text{ s}^{-1}$  for the divertor valves and  $0.0 - 2.0 \times 10^{22} \text{ e}^- \text{ s}^{-1}$  using the gas valves located at the outboard midplane. All discharges were designed to have high triangularities ( $\delta_{\text{low}} \approx 0.4$  and  $\delta_{\text{up}} \approx 0.3$ ). From the 15 discharges, 35 constant 600 ms to 2 s time windows were selected in which the overall plasma parameters remained unchanged. The evaluation of the separatrix region for all 35 time windows revealed a strong fluctuation in the signals of the He-beam diagnostic located inside the separatrix. The thermal helium beam diagnostic [84], as mentioned in section 2.5.4 with its high spatial resolution of 3 mm and its high temporal resolution of close to 1 MHz, is an ideal diagnostic with which to study such bursts.

Figure 7.1(a) shows the emission profile of the 587nm spectral line of the He-Beam diagnostic averaged over a 58 ms time window. The maximum of the emission lies in the far SOL at around  $\rho_{\text{pol}} = 1.07$ . Taking a closer look at this time window, figure 7.1(b) shows a time trace of the emission profiles. The mean emission profile is strongly influenced by the SOL filaments at 5.83 s and 5.867 s, but a region of high emission also exists very close inside the separatrix as depicted with a white line.

An even closer look at the emission profiles is depicted in figure 7.2(a) where for each single radial position, the intensity is normalized revealing an outward propagation of the bursts inside the separatrix, where some even cross the separatrix.

Technically, the bursts can be detected in the signals with a widely used method in filament studies that is shown in figure 7.2(b) and works as follows: The mean

<sup>1</sup> $P_{\text{tot}}$  here represents the total coupled heating power and  $P_{\text{rad}}$  the power that is exhausted by radiation.



**Fig. 7.2:** (a) Time trace of emission intensity of all helium beam channels, each time point normalized to its maximum in the time window marked by white lines in figure 7.1(b). (b) Time trace of one helium beam signal at  $\rho = 0.98$  showing how bursts are counted. The 2.5 sigma line of the signal is shown in black. Peaks higher than the signal for longer than  $3 \mu\text{s}$  are counted as bursts if no other burst was detected one autocorrelation time before.

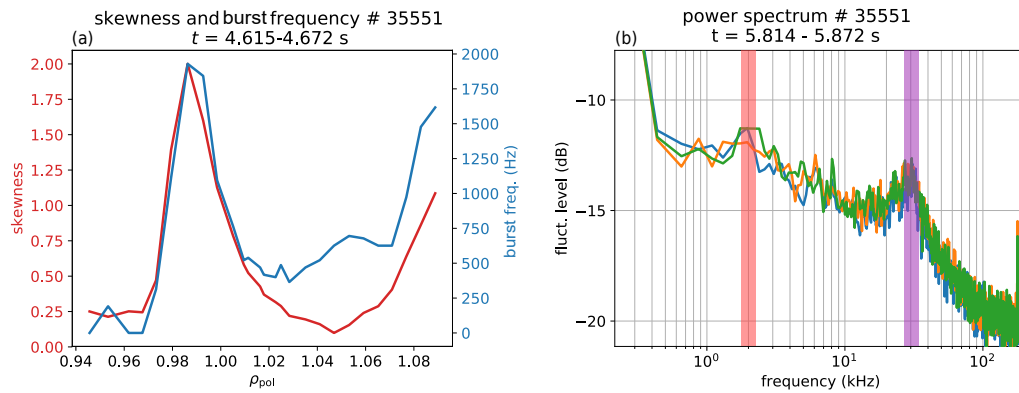


**Fig. 7.3:** (a) Radial profile of the burst frequency derived as the reciprocal of the time between bursts and the skewness of the signal. Power spectrum of three helium beam signals showing a peak at around the burst frequency and a higher intensity 30 kHz.

of the signal is normalized to 1. The standard deviation and the autocorrelation time of the signal is computed. A fluctuation of the signal is then counted as a burst when the amplitude of the signal stays above  $2.5 \times$  the standard deviation  $\sigma$  of the signal for longer than  $3 \mu\text{s}$  and no other burst was detected in the vicinity of one auto-correlation time of the peak. The  $2.5 \sigma$  line is depicted in black and the start and stop times of the bursts are marked with orange and purple triangles. The burst frequency can then be computed as the reciprocal of the waiting time between the bursts.

Performing this burst detection for every line of sight of the He-Beam leads to a radial profile of the burst frequency. Such a burst frequency profile is depicted in figure 7.3(a). The profile shows a maximum of the frequency inside but close to the separatrix and lower frequencies inside and outside of this peak. The detected

frequency increases again in the far SOL ( $\rho > 1.05$ ). In addition, the skewness of the signal is plotted in red. It is a measure of how skewed the distribution function of the signal is<sup>2</sup> and can therefore be used as a proxy for intermittency. The signal has the highest skewness/intermittency, where the maximum frequency is detected which suggests that the burst detection gives reasonable results. The frequency maximum in the 35 time windows analyzed can shift its position from  $\rho = 0.975$  up to  $\rho = 0.995$  and therefore instead of calculating the frequency only at one radial location, the whole radial frequency profile was evaluated and the maximum of the profile chosen as the burst frequency.

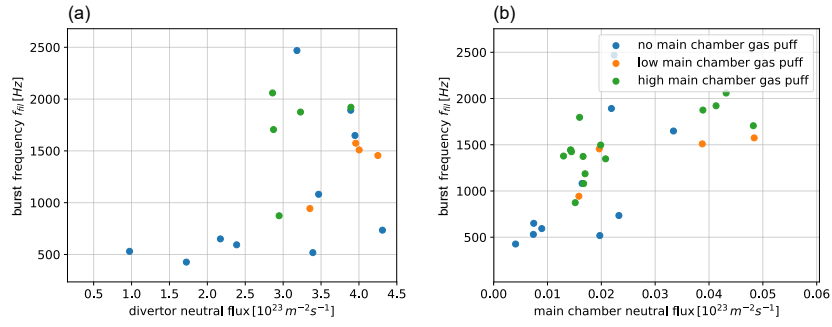
Looking at the power spectrum of the He-beam signals (figure 7.3(b)) a peak (marked by the red shaded area) in the range of 1 kHz corresponding to the determined burst frequency is visible as well. The power spectrum exhibits a second peak at around 30 kHz (marked by the purple shaded area) which is the frequency range of pedestal top modes reported in small ELM discharges in past experiments [43]. This study focuses on the lower frequency fluctuation located very close to the separatrix at the bottom of the pedestal, but the study of a correlation between the two frequencies and therefore different pedestal regions might be a worthwhile topic for future studies.

## 7.2 Parameter Dependence of the Burst Frequency

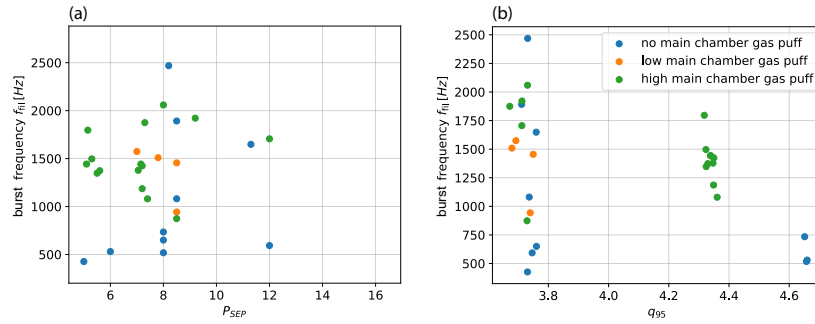
For a better physical understanding of the bursts inside the separatrix, the determined burst frequency is analyzed in the following section in relation to different plasma parameters. An influence of the amount of main chamber gas puff on the small ELMs was expected and therefore the time windows have been grouped into three categories, high main chamber fueling ( $\Gamma_{\text{main}} > 1 \times 10^{22} \text{ e}^- \text{ s}^{-1}$ , shown with green points), medium main chamber fueling ( $\Gamma_{\text{main}} < 1 \times 10^{22} \text{ e}^- \text{ s}^{-1}$ , shown with orange points) and without main chamber fueling (shown with blue points). It should be noted here that even in the high main chamber fueling cases, the flow rate from the divertor gas valves was higher in time windows by around a factor of two. Although, experience shows that fueling from the divertor is less efficient, as the valves are located in close vicinity to the cryo pump and about twice as much fueling rate is necessary to achieve the same plasma densities.

Figure 7.4 shows the determined burst frequency plotted over the neutral fluxes measured with manometers located at (a) the divertor and (b) the main chamber

<sup>2</sup>A skewness of 0 means the signal is Gaussian.



**Fig. 7.4:** Burst frequency of the database plotted over (a) the divertor neutral flux and (b) the main chamber neutral flux measured using manometers.



**Fig. 7.5:** Burst frequency of the database plotted over (a) the power crossing the separatrix  $P_{SEP}$  and (b) the edge safety factor.

(exact locations are shown in figure 2.6(a)). The burst frequency is higher for higher neutral fluxes and this positive correlation is stronger for the main chamber neutral flux. The measured fluxes are around 100 times higher in the divertor region. The medium and high main chamber gas puff points naturally show higher neutral gas fluxes and therefore also higher burst frequencies but there are some cases with no main chamber gas puff that also exhibit a high burst frequency.

In figure 7.5(a), the power crossing the separatrix shows no clear correlation to the burst frequency in the analyzed time windows, which can be interpreted as the burst frequency not being connected to the type-I / type-III ELM frequencies which scale positively / negatively with  $P_{SEP}$ . Additionally, as there is no clear correlation with  $P_{SEP}$ , this figure also shows that except for four outliers, most points with no main chamber gas puff exhibit low burst frequency while the medium and high main chamber puffed discharges scatter around 1.5 kHz.

Figure 7.5(b) shows the edge safety factor dependence of the burst frequency. The points are grouped in three areas showing the three different  $I_P$  and  $B_T$  combinations at  $q_{95} = 3.7, 4.35$  and  $4.7$ . Inside these groups the filament frequency reduces with increasing  $q$ .

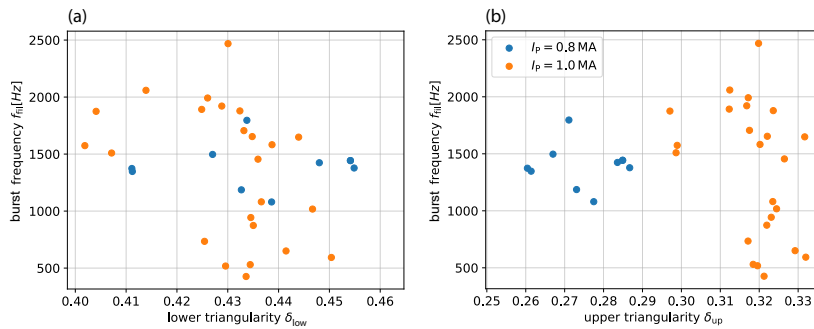


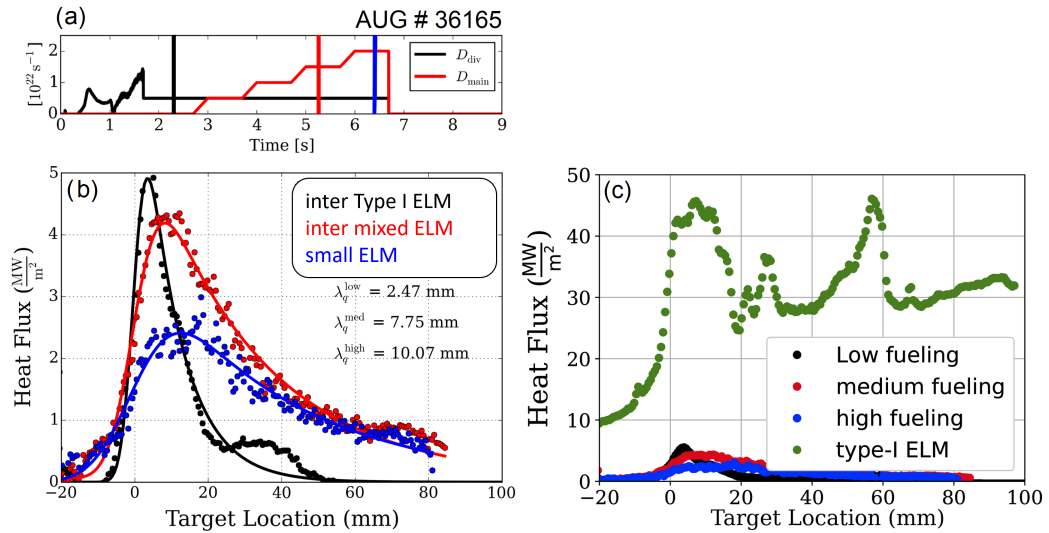
**Fig. 7.6:** Burst frequency of the database plotted over (a) the lower and (b) the upper triangularity.

The majority of points are at the lowest  $q_{95}$  which is most similar to the ITER Baseline scenario described in section 5.1. Although all discharges were planned to have similar plasma shapes the different power and fueling levels lead to a scatter in upper and lower triangularities. The dependence of the burst frequency on the triangularities is depicted in figure 7.6. While the different Shafranov shift for different currents clearly influenced the upper triangularity by increasing it for higher currents, the lower triangularity is not too much affected by the different currents. A slight correlation with lower burst frequencies at higher triangularities can be seen in the data.

In summary, the strongest correlation of the burst frequency in the dataset is found with the measured main chamber gas flux. The power crossing the separatrix shows no correlation to the burst frequency and the correlations with the safety factor and the triangularities are too weak to provide conclusive explanations. Further research should be aimed at expanding the data set with the inclusion of lower current discharges that have higher safety factors as this makes it easier to achieve small ELM regimes at different triangularities and the lower density is advantageous for most diagnostics.

### 7.3 Impact on the Divertor

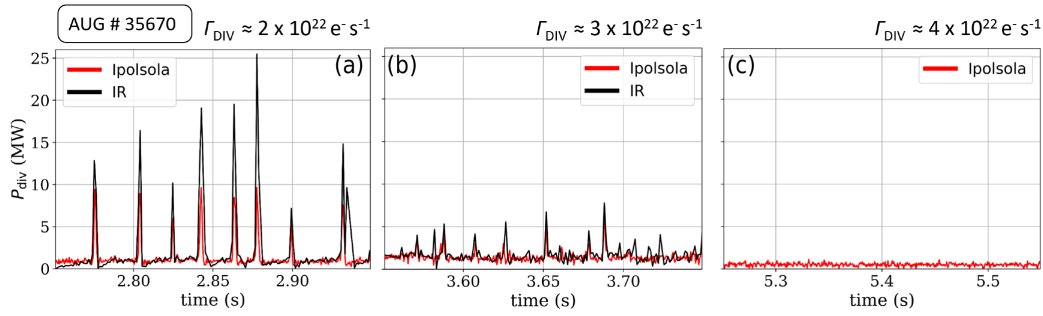
The second goal of the set of discharges described above was to better understand the power exhaust capabilities of small ELM discharges by analyzing the heat flux using infrared thermography. It was already hinted in the introduction of this thesis, that there are two challenges concerning ELM heat fluxes: First the so-called steady state heat flux between type-I ELMs (inter type-I ELM) is hard to predict for future devices. It is, therefore, common practice to compare power fall-off lengths [109].



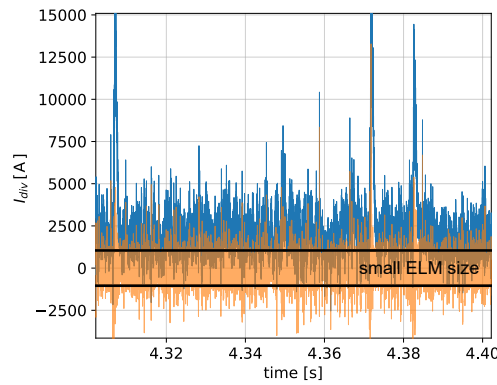
**Fig. 7.7:** (a) Time traces of the gas fueling scheme of AUG# 36165. (b) diverter heat flux profiles for the time windows shown by the colored lines in a and measured with the IR diagnostic. (c) heat flux profile during a type-I ELM.

Figure 7.7 shows a discharge with different fueling levels from the main chamber valve. Here different fueling levels lead to different ELM characteristics. While for no main chamber fueling the plasma is dominated by type-I ELMs, a medium main chamber fueling leads to a mix of type-I and small ELMs. For high main chamber fueling the plasma is dominated by small ELMs. The different fueling levels are depicted in figure 7.7(a). Figure 7.7(b) shows the heat flux profiles at the outer divertor for the three different points in time. The higher main chamber fueling not only leads to a lower peak heat flux but also to a broadening of the deposition profile and therefore a higher power fall-off length. Fitting the infrared data with the usual Eich fit formula [161], the power fall-off lengths for the low, the medium and the high fueling case can be obtained. While the low fueling case with  $\lambda_q^{\text{low}} = 2.47 \text{ mm}$  is comparable to the multi-machine database for type-I inter-ELM data [13], the medium fueled case leads to a fall-off length that is approximately three times as high  $\lambda_q^{\text{med}} = 7.75 \text{ mm}$ . In the high main chamber fueled small ELM dominant case where no type-I ELMs occur the fall-off length increases even further to  $\lambda_q^{\text{high}} = 10.07 \text{ mm}$ . This trend indicates that small ELM scenarios would be suitable for a reactor from a power exhaust point of view as broader fall-off lengths lead to a larger affected area and therefore less strain on the plasma facing materials. A detailed study of the small ELM exhaust properties is being prepared for publication [162].

The second challenge of ELM heat flux is the so-called transient heat flux arriving at the target during type-I ELMs which can lead to target temperatures high enough to degrade the divertor lifetime [20]. Figure 7.7(c), in addition to the three profiles



**Fig. 7.8:** Peak heat fluxes measured by the IR thermography system compared with the outer poloidal SOL current for three different divertor gas puff levels (a)-(c).



**Fig. 7.9:** Definition of the small ELM size as the standard deviation of the divertor current signal reduced by its running median to filter type-I ELMs.

shown in (b), depicts the heat-flux arriving at the target during a type-I ELM in the low fueling phase which is up to a factor of 10 higher than the inter-ELM heat flux. For the small ELM phases, no ELM subtraction of the signal is possible in the inter-ELM signals due to their high frequent nature meaning that for the divertor, they appear to be "quasi continuous".

A caveat of using the ASDEX Upgrade infra-red thermography to study small ELM heat fluxes is that for high gas puff values from the divertor valves the system is blinded by bremsstrahlung. In this study we therefore used the thermocurrent measured via shunts in the outer target as a proxy for the small ELM heat flux.

Figure 7.8 shows the integrated power reaching the outer divertor  $P_{\text{div}}$  and the divertor current multiplied by a constant factor ( $0.44 \times 10^1 - 3$ ) for three different divertor gas puff levels. For the lower two gas levels the divertor current is well correlated with the integrated outer divertor power obtained with the IR thermography. For the highest step the infrared data are not available due to bremsstrahlung, but the divertor current still shows the small ELM fluctuations.

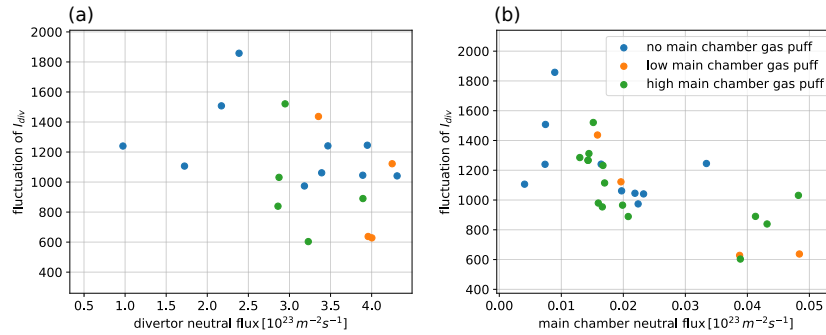


**Fig. 7.10:** Divertor current fluctuation amplitude as a proxy for small ELM size plotted over the (a) the divertor and (b) the main chamber neutral flux measured by manometers.

Most of the discharges of the dataset described in the previous chapter show mixed ELM behavior meaning that there are still some type-I ELMs left in the signal. To exclude the type-I ELM characteristics of the measured divertor currents, the running median has been subtracted from the signals. This process is explained in figure 7.9 where the blue curve depicts the original divertor current and the orange curve shows the remaining fluctuation after the subtraction of the running median. The standard deviation of the resulting signals is then defined as the small ELM size. It is a good measure for the magnitude of the signal fluctuation which always increases in discharges when small ELMs are present. The running median technique has been chosen over cutting out the type-I ELMs of the signals, as no prior knowledge of the type-I ELM starting times or duration is needed for the method and it can simply be applied to a large dataset.

## 7.4 Parameter Dependence of the small ELM Size

The small ELM size defined in section 7.3 has been calculated for the 35 time windows of the database and the following section shows how it is correlated with different plasma parameters following a similar structure as in section 7.1.

Figure 7.10 shows the small ELM size plotted over (a) the divertor and (b) the main chamber neutral flux measured with manometers. Both neutral fluxes show negative correlation with the small ELM size meaning that a higher neutral flux coincides with a smaller divertor current fluctuation. Similar to the burst frequency, the correlation is more prominent in the main chamber neutral flux data. Comparing the different colors, the magnitude of the main chamber gas puff shows only little effects on the small ELM size.

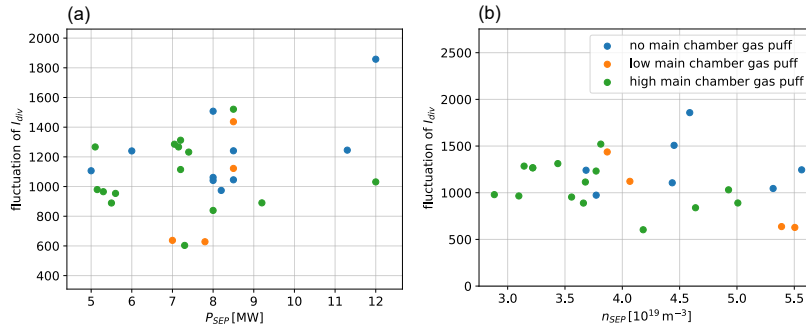


**Fig. 7.11:** Divertor current fluctuation amplitude as a proxy for small ELM size plotted over (a) the power crossing the separatrix  $P_{SEP}$  and (b) the separatrix density  $n_{SEP}$ .

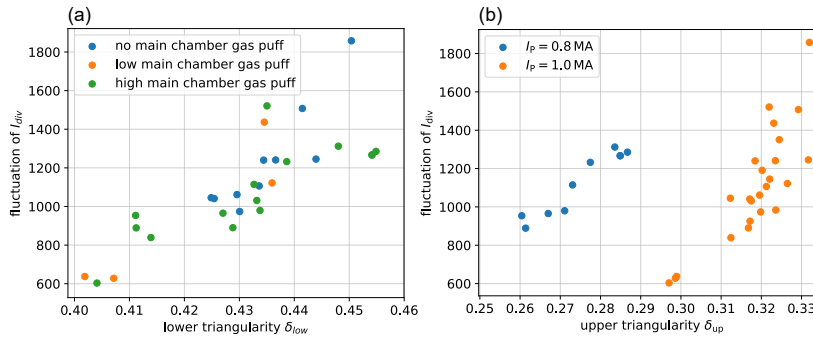


**Fig. 7.12:** Divertor current fluctuation amplitude, as a proxy for small ELM size plotted over (a) the lower and (b) the upper triangularity.

In figure 7.11(a), the small ELM size is shown in relation to the power crossing the separatrix. The data show a minor positive correlation that is independent of the magnitude of the main chamber gas fueling. Figure 7.11(b) shows that the divertor current fluctuations in the analyzed time windows do not depend on the separatrix density acquired from IDA profiles. This is in agreement with reports that the divertor conditions are the most important parameter in setting the separatrix density [163].

A strong influence on the small ELM size has been found for the small changes of plasma shape in previous chapters. Figure 7.12(a) shows, that for the small changes in lower triangularity in this database, the small ELM size increases by up to a factor of three. This increase in the divertor fluctuations is also found for increasing upper triangularity shown in (b). Here the points are again separated into two groups coming from different Shafranov shifts for the different plasma currents. A strong positive correlation is found for both plasma current subgroups of points but not for the whole dataset. As already suggested in section 7.2, further experiments at lower plasma current would make it easier to study this shape dependence in more detail.

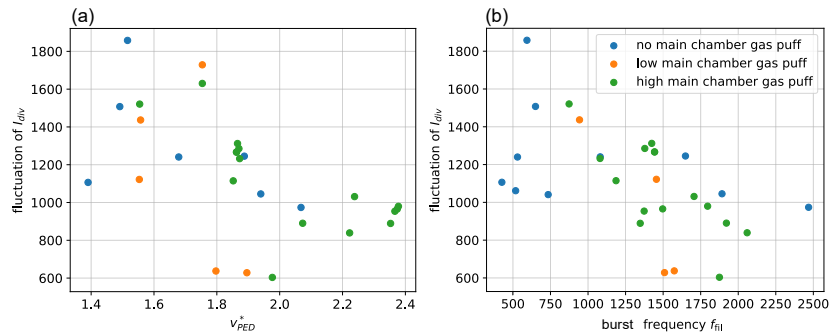


**Fig. 7.13:** Divertor current fluctuation amplitude, as a proxy for small ELM size plotted over (a) the pedestal top collisionality (b) the small ELM burst frequency determined in section 7.1.

Finally, figure 7.13 shows the small ELM size in relation to (a) the pedestal top collisionality and (b) the burst frequency defined in section 7.1. For lower pedestal top collisionalities, the small ELM size increases in a similar way to the type-I ELM data shown in the introduction. It should be noted here that, due to the high pedestal top density and relatively low temperature in these discharges, the collisionalities are still around 20 times higher than what is expected for ITER. As the small ELM size decreases for a higher frequency of the bursts inside the separatrix, it might be possible to keep the small ELMs inconsequential for the divertor if the burst frequency can be influenced by e.g. increasing the main chamber neutral flux or the plasma triangularity. The broader footprint of the ELMs, shown by the increased  $\lambda_q$ , might also help with the compatibility of the small ELMs in future machines but further research is needed.

## 7.5 Chapter Summary

In this chapter, correlations of different plasma parameters to a characteristic burst frequency inside the separatrix and to a defined small ELM size have been analyzed. The results can be summarized as follows:

- Higher neutral fluxes measured in the divertor and in the main chamber below the midplane coincide with higher burst frequencies and lower small ELM size.
- In the time windows analyzed, the power crossing the separatrix is not correlated with the burst frequency inside the separatrix and shows only a weak positive correlation to the small ELM size.

- Although the plasma shapes of the time windows compared were very similar, a weak negative correlation of the lower triangularity to the burst frequency was found. In addition, a higher triangularity (upper and lower) coincides with a larger small ELM size.
- The dataset also suggests a negative correlation of the small ELM size to the pedestal top collisionality, similar to type-I ELMs.
- A higher burst frequency inside the separatrix leads to a lower small ELM size.
- The heat flux profile widens in the small ELM dominated case leading to four times higher power fall-off lengths.

## Summary and Conclusion

” *We believe this resolves all remaining questions on this topic. No further research is needed.*

— **no one**  
ever

Small ELM regimes have in the past been ruled out when considering reactor scenarios because they coincide with a high pedestal top collisionality. The results of this work show that this exclusion might have been premature.

### 8.1 Summary

The first experiments performed in the course of this thesis managed to decouple the pedestal top from the separatrix conditions by comparing pellet fueled with gas fueled discharges. These experiments showed that a high separatrix density necessary for good plasma exhaust in a reactor, is crucial for small ELM regimes. The first hypothesis explaining this behavior was that the **origin** of the small ELMs lies at the bottom of the pedestal, very close to the separatrix and that they are excited by the high pressure gradient that coincides with a high separatrix density. This hypothesis was strengthened with predictive peeling-ballooning stability calculations showing that a flattened density gradient just inside the separatrix causes a narrower pedestal which is more stable against type-I ELMs. The experiments also showed that small ELMs and type-I ELMs can occur simultaneously and changes in the magnetic shear caused by small variations of the plasma shape can influence the balance between both ELM types. These findings suggested that the stability of type-I ELMs and small ELMs is governed by different mechanisms. A model that expands the peeling-ballooning stability diagrams by adding a critical gradient ballooning model for the separatrix conditions was proposed. In this model the small ELMs behave like ballooning modes, originating at the pedestal bottom, driven by the pressure gradient and stabilized by magnetic shear.

In order to improve the capability to extrapolate to future machines, the small ELM ballooning model was tested by means of experiments conducted on a second machine. These discharges confirmed the importance of the separatrix conditions and showed first results of the advantageous exhaust capabilities, namely a broader footprint in small ELM scenarios using thermography.

For a more detailed understanding of the physical mechanism behind the small ELMs, additional experiments with a large variation in plasma current and toroidal fields were carried out. Various mechanisms that determine plasma edge stability, namely the flux surface averaged and the local magnetic shear as well as the  $E \times B$  shear, have been compared for phases dominated by small ELMs and phases with type-I ELMs. Ideal ballooning stability calculations confirmed that plasmas dominated by small ELMs are indeed ballooning unstable close to the separatrix ( $\rho > 0.99$ ). This unstable area can be influenced by plasma shaping which is strongly coupled to the local magnetic shear and the connection length between the good and the bad curvature region of the plasma. When the small ELMs are concentrated further outside, the ideal ballooning stability of the steep gradient region ( $\rho \approx 0.98$ ) can increase. This manifests in a broader pedestal that is more peeling-ballooning unstable and therefore type-I ELMs reoccur. A fine balance between the ideal ballooning instability at the pedestal bottom and the peeling-ballooning stability of the whole pedestal region therefore determines whether the plasma edge is dominated by small ELMs or type-I ELMs.

Small ELMs have been diagnosed using the helium-beam diagnostic and appear as bursts just inside the separatrix with frequencies ranging from 500 Hz to 2.5 kHz. This burst frequency is not correlated to gas fueling location or magnitude but is strongly correlated to neutral flux measurements. An explanation for this is that a higher burst frequency leads to a higher perpendicular transport through filaments which causes more recycling from the wall and therefore a higher neutral flux. The frequency was found to be independent of the input heating power which is further evidence of the small ELM stability not being governed by the pedestal top conditions.

Finally, the **transport** of the small ELMs and therefore their impact on the divertor has been assessed. As explained before, small ELM scenarios need high gas puffing to achieve a sufficiently high separatrix density. Due to limits of the thermography system, the lowest possible gas puff settings to achieve small ELMs was used to measure heat-flux profiles during a small ELM phase. These profiles show a widening of the power fall-off length by a factor of four when compared to the multi-machine inter type-I ELM database. This is caused by the filamentary transport of the small

ELMs that is so highly frequent that for the divertor it appears to be quasi-continuous. For discharges with higher gas puffs, the fluctuations in divertor current signals were used as a proxy for the divertor impact. This small ELM size is negatively correlated to the neutral flux and the burst frequency. The increased perpendicular transport due to filaments therefore leads to a widening of the divertor footprint and consequently to a reduction of the heat flux.

## 8.2 Small ELMs as a Reactor Scenario

The results obtained in this thesis are highly promising for the implementation of small ELM scenarios in future machines. Small ELM scenarios are ballooning unstable very close to the separatrix and occur at the anticipated ITER separatrix conditions but show a significant widening of the heat-flux footprint.

Some questions still remain to be answered:

- Will the small ELM ballooning modes also be unstable in ITER and, if so, in which area of the pedestal?
- Is the middle of the pedestal also in the second stability regime such that the ballooning modes at the foot of the pedestal will not take up too much space or will they weaken the confinement and the pedestal top cannot get hot enough?
- How does this influence the peeling-ballooning limit of the ITER pedestal? Can the ballooning modes at the foot of the pedestal provide sufficient transport to prevent the occurrence of type-I ELMs?
- How does the widening of the heat-flux footprint extrapolate to ITER and is the increased perpendicular transport caused by the small ELMs beneficial for detachment?

These questions should be addressed in future research using nonlinear MHD and turbulence codes with the inclusion of drifts and the neutral particle dynamics. The development of the necessary features is an open topic in the modelling community.

## 8.3 Ideas for Future Research

Further ideas on how to expand the understanding of small ELM regimes experimentally include:

- Disentangling the impact of elongation, triangularity and closeness to double null on small ELM regimes through e.g. discharges at constant elongation with various triangularities or vice versa.
- Analyzing the impact of neutral flux in further detail by using a new manometer infrastructure and more advanced gas puff modulation techniques or divertor baffles.
- Assessing the compatibility of the small ELM regime with divertor detachment.
- Eliminating operational concerns by demonstrating a plasma start-up without type-I ELMs directly into a quasi-continuous edge transport regime.

Some of these experiments are already being prepared in the European fusion research program because the results presented in this thesis have laid the foundation for a revival of the small ELM regime as a promising exhaust scenario with good confinement in tokamak plasmas.

# Danksagung

Ich schreibe diese Zeilen acht Wochen nachdem die Doktorarbeit an die Gutachter geschickt wurde. Zu diesem Zeitpunkt habe ich noch nicht wirklich realisiert dass die Doktors Zeit jetzt ein Ende findet. Ohne der Hilfe von sehr vielen besonderen Menschen wäre es auch nie so weit gekommen. Diesen Menschen<sup>1</sup> will ich im abschließenden Kapitel danken.

Eine Doktorarbeit beginnt meist als Idee im Kopf des Betreuenden. Ich hatte das Glück gleich von zwei ausgezeichneten Wissenschaftlern unter ihre Fittiche genommen zu werden. Liebe Lisl, du warst in den letzten 5 Jahren eine großartige Mentorin. Du hast mich auf das Thema "kleine ELMs" gebracht und bist mir quasi jederzeit (am Ende sogar im Urlaub) mit Rat und Tat und konstruktiven Kommentaren zur Seite gestanden. Du hast es geschafft mich durch den Urwald an Daten zu leiten ohne mich zu oft im Dickicht zu verirren. Dankeschön! Lieber Fritz, von dir habe ich gelernt wie ein Wissenschaftlerleben funktionieren kann. Du hast es immer wieder geschafft mich auf deine eigene Art zu motivieren und alle Deadlines doch irgendwie noch einzuhalten. Dafür bin ich dir sehr dankbar.

Großer Dank gilt auch der Schiedel Stiftung und dem Eurofusion MST1 Projekt, ohne deren finanzielle Unterstützung ich mein Projekt nie hätte realisieren können. Für die Hilfe beim Organisieren meiner Forschungsaufenthalte und das jonglieren der unterschiedlichen Topics an den verschiedenen Maschinen möchte ich mich bei Lätitia und Monika sowie Hendrik, Matthias und Benoit und meinem Co-SC Michael bedanken.

Auch meinen Vorgängern Florian (der jetzt in Amerika Karriere macht) und Matthias (der mich ab und zu beim Tennis gewinnen lässt), die mit ihren ausgezeichneten Arbeiten den Weg für eine weitere Wien/Garching Doktorarbeit geebnet haben gebührt mein Dank. Ich hoffe meinen Teil dazu beigetragen zu haben, damit noch weitere Arbeiten im selben Stil zustande kommen können. No pressure Lidija ;-). Danke auch für deine Mithilfe beim Erstellen dieser Doktorarbeit auch zu etwas unkonventionellen Tageszeiten.

---

<sup>1</sup>Die folgende Aufzählung ist mit Sicherheit nicht komplett und ich entschuldige mich schon im Voraus bei denen, die ihren Namen hier vermissen.

Meinen Wiener Doktorgeschwistern Janine und Reinhard S. und unseren kleinen Space Brüdern Paul und Herbert danke ich recht herzlich für die gemeinsam verbrachten Stunden beim Kaffee und Getratsche im Malina oder kürzlich auch im #RIPZoomchat.

Nach längeren Dienstreisen fühlte sich die Rückkehr ins Freihaus nicht nur wegen der Kulinarik der Wiener Innenstadt immer ein Bisschen wie "nach Hause kommen" an. Für das familiäre Klima sorgte der ganze Atom- und Plasmaphysik Forschungsbereich, allen voran Richard und das neue Doktoranden Triple, Anna, Christian und Gabriel aber auch Daniel, Johanna und Waldemar und nicht zu vergessen Martin und Ille, die immer wieder Mal eine interessante oder lustige Geschichte auf Lager hatten.

Da ich bei den letzten Garching Besuchen meine Gästewohnung nicht mehr hatte durfte ich auf den Sofas von Alex und Pierre crashen. Das führte zu einigen Sous VideO Game, Croissant Back und VR Abenden and die ich mich gerne zurückerinnere.

Bevor ich ins I1 MST Exil geschickt wurde, durfte ich das große Doktoranden Büro mit Uli, Maxi, Ou Pan, Nikola und Monika teilen. Auch bei euch möchte ich mich für die netten, meist zu langen Abende im Büro bedanken.

Viel Zeit habe ich auch im Kontrollraum (2) mit dem LiBES Team verbracht dessen Zusammensetzung sich über die Jahre immer wieder verändert hat und damit immer interessant blieb. Danke an Gregor, Nils, Karola und Balazs.

Danke auch an all die Garchinger Kollegen und Freunden, die mir geholfen haben das ein oder andere Problem, physikalischer oder anderer Natur, zu lösen oder nach der Arbeit mit mir Brettspiele und Volleyball spielten, ins Kino oder auch einfach nur mal auf ein Bier gingen. Auf die Gefahr hin jemanden zu vergessen: Danke Michi, Angela, Branka, Mike, Felician, Wibke, Javier, Alex, Philip, Christian, Andreas, Marco, Adri, Thomas, Davide, Andres, Paula, Joaquin, Stephan, Teo, Anton, Pilar, Dominik, Klara, Lennard, Eli, Tim, Athina, Rachael, Rainer, Severin, Johannes, Martin, Thomas und Jörg.

Fiona Langthaler hat sich hier eine besondere Erwähnung mit extra vielen Beistrichen verdient, weil sie beim Korrekturlesen so viele davon weggestrichen, und an anderer Stelle, wieder eingefügt hat. Thx :-)

Ganz herzlich bedanken will ich mich auch bei meiner ganzen Familie, bei den Pinds und den Millers und meinen Langauer Freunden die immer interessiert gefragt haben wie es mir beim Schreiben geht und mich motiviert haben dran zu bleiben und das Ding fertig zu machen.

Besonderer Dank gilt auch meinen Eltern, die mich bis heute prägen und mich bei all meinen Projekten immer tatkräftig unterstützen. Danke für Alles.

Zu guter Letzt möchte ich mich noch bei meiner Magdalena bedanken. Die letzten paar Monate in denen wir Corona bedingt sehr viel mehr Zeit miteinander in Hötzelsdorf verbrachten, haben uns noch näher zusammengeschweißt. Immer wenn ich im Endspurt beim Schreiben kurz davor war den Hut draufzuhauen und ein Kapitel wegzulassen, hast du liebe Magdi mich wieder heruntergeholt, einen Zeitplan gemacht und mir den Kopf wieder zurechtgerückt. Jetzt wo dieses große Abenteuer beendet ist steht uns gleich noch ein weiteres bevor. Ich bin aber davon überzeugt, dass wir Beide auch das mit Bravour meistern werden.



# Bibliography

- [1] C.A. Horowitz. “Paris Agreement”. In: *Int. Leg. Mater.* 55.4 (Aug. 2016), pp. 740–755. DOI: [10.1017/S0020782900004253](https://doi.org/10.1017/S0020782900004253) (cit. on pp. 1, 4).
- [2] V. Smil. *Energy Transitions: Global and National Perspectives*. ABC-CLIO, LLC, 2017, p. 282 (cit. on p. 2).
- [3] S.R. Hurt. “World Development Indicators”. In: *Encycl. Gov.* (2012). DOI: [10.4135/9781412952613.n571](https://doi.org/10.4135/9781412952613.n571) (cit. on pp. 2, 3).
- [4] IEA. *Data and statistics*. 2019. DOI: <https://www.iea.org/data-and-statistics?country=WO> (cit. on p. 2).
- [5] C. Le Quéré, R.M. Andrew, P. Friedlingstein, et al. “Global Carbon Budget 2018”. In: *Earth Syst. Sci. Data* 10.4 (Dec. 2018), pp. 2141–2194. DOI: [10.5194/essd-10-2141-2018](https://doi.org/10.5194/essd-10-2141-2018) (cit. on p. 3).
- [6] S. Solomon, D. Qin, M. Manning, et al. *Climate Change 2007: The Physical Science Basis. Contribution of Working Group I to the Fourth Assessment Report of the Intergovernmental Panel on Climate Change*. Tech. rep. Cambridge, United Kingdom and New York, USA: Cambridge University Press, 2007 (cit. on p. 4).
- [7] S. Weitemeyer, D. Kleinhans, T. Vogt, and C. Agert. “Integration of Renewable Energy Sources in future power systems: The role of storage”. In: *Renew. Energy* 75 (Mar. 2015), pp. 14–20. DOI: [10.1016/j.renene.2014.09.028](https://doi.org/10.1016/j.renene.2014.09.028). arXiv: [1405.2857](https://arxiv.org/abs/1405.2857) (cit. on p. 4).
- [8] G. Audi, A.H. Wapstra, and C. Thibault. “The Ame2003 atomic mass evaluation”. In: *Nucl. Phys. A* 729.1 (Dec. 2003), pp. 337–676. DOI: [10.1016/j.nuclphysa.2003.11.003](https://doi.org/10.1016/j.nuclphysa.2003.11.003) (cit. on p. 6).
- [9] J.D. Lawson. “Some Criteria for a Power Producing Thermonuclear Reactor”. In: *Proc. Phys. Soc. Sect. B* 70.1 (Jan. 1957), pp. 6–10. DOI: [10.1088/0370-1301/70/1/303](https://doi.org/10.1088/0370-1301/70/1/303) (cit. on p. 8).
- [10] D.A. Brown, M.B. Chadwick, R. Capote, et al. “ENDF/B-VIII.0: The 8 th Major Release of the Nuclear Reaction Data Library with CIELO-project Cross Sections, New Standards and Thermal Scattering Data”. In: *Nucl. Data Sheets* 148 (Feb. 2018), pp. 1–142. DOI: [10.1016/j.nds.2018.02.001](https://doi.org/10.1016/j.nds.2018.02.001) (cit. on p. 8).
- [11] A. Köhn-Seemann. *alfkoehn/fusion\_plots: First release of the fusion\_plots package*. 2020. DOI: [10.5281/zenodo.3744715](https://doi.org/10.5281/zenodo.3744715) (cit. on p. 8).

- [12]F. Wagner, G. Becker, K. Behringer, et al. “Regime of Improved Confinement and High Beta in Neutral-Beam-Heated Divertor Discharges of the ASDEX Tokamak”. In: *Phys. Rev. Lett.* 49.19 (Nov. 1982), pp. 1408–1412. DOI: [10.1103/PhysRevLett.49.1408](https://doi.org/10.1103/PhysRevLett.49.1408) (cit. on p. 9).
- [13]T. Eich, A.W. Leonard, R.A. Pitts, et al. “Scaling of the tokamak near the scrape-off layer H-mode power width and implications for ITER”. In: *Nucl. Fusion* 53.9 (Sept. 2013), p. 093031. DOI: [10.1088/0029-5515/53/9/093031](https://doi.org/10.1088/0029-5515/53/9/093031) (cit. on pp. 11, 105).
- [14]A. Loarte, B. Lipschultz, A.S. Kukushkin, et al. “Chapter 4: Power and particle control”. In: *Nucl. Fusion* 47.6 (June 2007), S203–S263. DOI: [10.1088/0029-5515/47/6/S04](https://doi.org/10.1088/0029-5515/47/6/S04) (cit. on pp. 11, 49, 78).
- [15]B. Riccardi, R. Giniatulin, N. Klimov, V. Koidan, and A. Loarte. “Preliminary results of the experimental study of PFCs exposure to ELMs-like transient loads followed by high heat flux thermal fatigue”. In: *Fusion Eng. Des.* 86.9-11 (Oct. 2011), pp. 1665–1668. DOI: [10.1016/j.fusengdes.2011.04.069](https://doi.org/10.1016/j.fusengdes.2011.04.069) (cit. on p. 11).
- [16]Th. Loewenhoff, S. Bardin, H. Greuner, et al. “Impact of combined transient plasma/heat loads on tungsten performance below and above recrystallization temperature”. In: *Nucl. Fusion* 55.12 (Nov. 2015), p. 123004. DOI: [10.1088/0029-5515/55/12/123004](https://doi.org/10.1088/0029-5515/55/12/123004) (cit. on p. 12).
- [17]J.P. Gunn, S. Carpentier-Chouchana, F. Escourbiac, et al. “Surface heat loads on the ITER divertor vertical targets”. In: *Nucl. Fusion* 57.4 (Apr. 2017), p. 046025. DOI: [10.1088/1741-4326/aa5e2a](https://doi.org/10.1088/1741-4326/aa5e2a) (cit. on p. 12).
- [18]W. Suttrop. “The physics of large and small edge localized modes”. In: *Plasma Phys. Control. Fusion* 42.5A (May 2000), A1–A14. DOI: [10.1088/0741-3335/42/5A/301](https://doi.org/10.1088/0741-3335/42/5A/301) (cit. on p. 12).
- [19]A. Herrmann. “Overview on stationary and transient divertor heat loads”. In: *Plasma Phys. Control. Fusion* 44.6 (June 2002), pp. 883–903. DOI: [10.1088/0741-3335/44/6/318](https://doi.org/10.1088/0741-3335/44/6/318) (cit. on p. 12).
- [20]A. Loarte, G. Saibene, R. Sartori, et al. “ELM energy and particle losses and their extrapolation to burning plasma experiments”. In: *J. Nucl. Mater.* 313-316.SUPPL. (Mar. 2003), pp. 962–966. DOI: [10.1016/S0022-3115\(02\)01398-3](https://doi.org/10.1016/S0022-3115(02)01398-3) (cit. on pp. 13, 105).
- [21]E. Viezzer. “Access and sustainment of naturally ELM-free and small-ELM regimes”. In: *Nucl. Fusion* 58.11 (Nov. 2018), p. 115002. DOI: [10.1088/1741-4326/aac222](https://doi.org/10.1088/1741-4326/aac222) (cit. on pp. 13, 50, 69).
- [22]P. Gohil, M. Ali Mahdavi, L. Lao, et al. “Study of Giant Edge-Localized Modes in DIII-D and Comparison with Ballooning Theory”. In: *Phys. Rev. Lett.* 61.14 (Oct. 1988), pp. 1603–1606. DOI: [10.1103/PhysRevLett.61.1603](https://doi.org/10.1103/PhysRevLett.61.1603) (cit. on p. 12).
- [23]E.J. Doyle, R.J. Groebner, K.H. Burrell, et al. “Modifications in turbulence and edge electric fields at the L–H transition in the DIII-D tokamak”. In: *Phys. Fluids B Plasma Phys.* 3.8 (Aug. 1991), pp. 2300–2307. DOI: [10.1063/1.859597](https://doi.org/10.1063/1.859597) (cit. on pp. 12, 13).

- [24]H. Zohm. “Edge localized modes (ELMs)”. In: *Plasma Phys. Control. Fusion* 38.2 (Feb. 1996), pp. 105–128. DOI: [10.1088/0741-3335/38/2/001](https://doi.org/10.1088/0741-3335/38/2/001) (cit. on pp. 12, 13).
- [25]J.W. Connor. “A review of models for ELMs”. In: *Plasma Phys. Control. Fusion* 40.2 (Feb. 1998), pp. 191–213. DOI: [10.1088/0741-3335/40/2/003](https://doi.org/10.1088/0741-3335/40/2/003) (cit. on pp. 12, 43, 45).
- [26]P.B. Snyder, H.R. Wilson, J.R. Ferron, et al. “Edge localized modes and the pedestal: A model based on coupled peeling–ballooning modes”. In: *Phys. Plasmas* 9.5 (May 2002), pp. 2037–2043. DOI: [10.1063/1.1449463](https://doi.org/10.1063/1.1449463) (cit. on pp. 12, 45, 64).
- [27]P.T. Lang, G.D. Conway, T. Eich, et al. “ELM pace making and mitigation by pellet injection in ASDEX Upgrade”. In: *Nucl. Fusion* 44.5 (May 2004), pp. 665–677. DOI: [10.1088/0029-5515/44/5/010](https://doi.org/10.1088/0029-5515/44/5/010) (cit. on p. 13).
- [28]A.W. Degeling, Y.R. Martin, J.B. Lister, et al. “Magnetic triggering of ELMs in TCV”. In: *Plasma Phys. Control. Fusion* 45.9 (Sept. 2003), pp. 1637–1655. DOI: [10.1088/0741-3335/45/9/306](https://doi.org/10.1088/0741-3335/45/9/306) (cit. on p. 13).
- [29]S.H. Kim, M.M. Cavinato, V. Dokuka, et al. “Comparing magnetic triggering of ELMs in TCV and ASDEX Upgrade”. In: *Plasma Phys. Control. Fusion* 51.5 (May 2009), p. 055021. DOI: [10.1088/0741-3335/51/5/055021](https://doi.org/10.1088/0741-3335/51/5/055021) (cit. on p. 13).
- [30]E. de la Luna, I.T. Chapman, F. Rimini, et al. “Understanding the physics of ELM pacing via vertical kicks in JET in view of ITER”. In: *Nucl. Fusion* 56.2 (Feb. 2016), p. 026001. DOI: [10.1088/0029-5515/56/2/026001](https://doi.org/10.1088/0029-5515/56/2/026001) (cit. on p. 13).
- [31]N. Wu, S.Y. Chen, M.L. Mou, et al. “Study on edge localized mode during plasma vertical swing in HL-2A tokamak”. In: *Phys. Plasmas* 25.10 (Oct. 2018), p. 102505. DOI: [10.1063/1.5049348](https://doi.org/10.1063/1.5049348) (cit. on p. 13).
- [32]R. Nazikian, C. Paz-Soldan, J.D. Callen, et al. “Pedestal Bifurcation and Resonant Field Penetration at the Threshold of Edge-Localized Mode Suppression in the DIII-D Tokamak”. In: *Phys. Rev. Lett.* 114.10 (Mar. 2015), p. 105002. DOI: [10.1103/PhysRevLett.114.105002](https://doi.org/10.1103/PhysRevLett.114.105002) (cit. on p. 13).
- [33]W. Suttrop, A. Kirk, V. Bobkov, et al. “Experimental conditions to suppress edge localised modes by magnetic perturbations in the ASDEX Upgrade tokamak”. In: *Nucl. Fusion* 58.9 (Sept. 2018), p. 096031. DOI: [10.1088/1741-4326/aace93](https://doi.org/10.1088/1741-4326/aace93) (cit. on p. 13).
- [34]M. Willensdorfer, T.B. Cote, C.C. Hegna, et al. “Field-Line Localized Destabilization of Ballooning Modes in Three-Dimensional Tokamaks”. In: *Phys. Rev. Lett.* 119.8 (Aug. 2017), p. 085002. DOI: [10.1103/PhysRevLett.119.085002](https://doi.org/10.1103/PhysRevLett.119.085002) (cit. on pp. 13, 64).
- [35]J-K. Park, Y. Jeon, Y. In, et al. “3D field phase-space control in tokamak plasmas”. In: *Nat. Phys.* 14.12 (Dec. 2018), pp. 1223–1228. DOI: [10.1038/s41567-018-0268-8](https://doi.org/10.1038/s41567-018-0268-8) (cit. on p. 13).
- [36]T. Ozeki and M. Azumi. “Access to the Second Stability Regime near the Plasma Surface in a High- $q$ , Low-Shear Tokamak Plasma”. In: *J. Phys. Soc. Japan* 59.3 (Mar. 1990), pp. 927–933. DOI: [10.1143/JPSJ.59.927](https://doi.org/10.1143/JPSJ.59.927) (cit. on pp. 13, 69).

- [37]T. Ozeki, M.S. Chu, L.L. Lao, et al. “Plasma shaping, edge ballooning stability and ELM behaviour in DIII-D”. In: *Nucl. Fusion* 30.8 (Aug. 1990), pp. 1425–1432. DOI: [10.1088/0029-5515/30/8/003](https://doi.org/10.1088/0029-5515/30/8/003) (cit. on p. 13).
- [38]G. Saibene, P.J. Lomas, R. Sartori, et al. “Characterization of small ELM experiments in highly shaped single null and quasi-double-null plasmas in JET”. In: *Nucl. Fusion* 45.5 (May 2005), pp. 297–317. DOI: [10.1088/0029-5515/45/5/001](https://doi.org/10.1088/0029-5515/45/5/001) (cit. on p. 13).
- [39]J. Stober, P.J. Lomas, G. Saibene, et al. “Small ELM regimes with good confinement on JET and comparison to those on ASDEX Upgrade, Alcator C-mod and JT-60U”. In: *Nucl. Fusion* 45.11 (Nov. 2005), pp. 1213–1223. DOI: [10.1088/0029-5515/45/11/001](https://doi.org/10.1088/0029-5515/45/11/001) (cit. on pp. 13, 50, 59).
- [40]A. Kirk, T. O’Gorman, S. Saarelma, R. Scannell, and H.R. Wilson. “A comparison of H-mode pedestal characteristics in MAST as a function of magnetic configuration and ELM type”. In: *Plasma Phys. Control. Fusion* 51.6 (June 2009), p. 065016. DOI: [10.1088/0741-3335/51/6/065016](https://doi.org/10.1088/0741-3335/51/6/065016) (cit. on p. 13).
- [41]N. Oyama, P. Gohil, L.D. Horton, et al. “Pedestal conditions for small ELM regimes in tokamaks”. In: *Plasma Phys. Control. Fusion* 48.5A (May 2006), A171–A181. DOI: [10.1088/0741-3335/48/5A/S16](https://doi.org/10.1088/0741-3335/48/5A/S16) (cit. on pp. 13, 50, 69, 73).
- [42]A. Kirk, H.W. Muller, E. Wolfrum, et al. “Comparison of small edge-localized modes on MAST and ASDEX Upgrade”. In: *Plasma Phys. Control. Fusion* 53.9 (Sept. 2011), p. 095008. DOI: [10.1088/0741-3335/53/9/095008](https://doi.org/10.1088/0741-3335/53/9/095008) (cit. on pp. 13, 50).
- [43]E. Wolfrum, M. Bernert, J.E. Boom, et al. “Characterization of edge profiles and fluctuations in discharges with type-II and nitrogen-mitigated edge localized modes in ASDEX Upgrade”. In: *Plasma Phys. Control. Fusion* 53.8 (Aug. 2011), p. 085026. DOI: [10.1088/0741-3335/53/8/085026](https://doi.org/10.1088/0741-3335/53/8/085026) (cit. on pp. 13, 50, 59, 70, 73, 102).
- [44]T. Kass, S. Günter, M. Maraschek, et al. “Characteristics of type I and type III ELM precursors in ASDEX upgrade”. In: *Nucl. Fusion* 38.1 (Jan. 1998), pp. 111–116. DOI: [10.1088/0029-5515/38/1/310](https://doi.org/10.1088/0029-5515/38/1/310) (cit. on p. 13).
- [45]R.J. Colchin, B.A. Carreras, R. Maingi, et al. “Physics of slow L-H transitions in the DIII-D tokamak”. In: *Nucl. Fusion* 42.9 (Sept. 2002), p. 312. DOI: [10.1088/0029-5515/42/9/312](https://doi.org/10.1088/0029-5515/42/9/312) (cit. on p. 13).
- [46]G. Birkenmeier, M. Cavedon, G.D. Conway, et al. “Magnetic structure and frequency scaling of limit-cycle oscillations close to L- to H-mode transitions”. In: *Nucl. Fusion* 56.8 (Aug. 2016), p. 086009. DOI: [10.1088/0029-5515/56/8/086009](https://doi.org/10.1088/0029-5515/56/8/086009) (cit. on p. 13).
- [47]M. Bernert, M. Wischmeier, A. Huber, et al. “Power exhaust by SOL and pedestal radiation at ASDEX Upgrade and JET”. In: *Nucl. Mater. Energy* 12 (Aug. 2017), pp. 111–118. DOI: [10.1016/j.nme.2016.12.029](https://doi.org/10.1016/j.nme.2016.12.029) (cit. on p. 13).
- [48]R. Maingi, C.E. Bush, E.D. Fredrickson, et al. “H-mode pedestal, ELM and power threshold studies in NSTX”. In: *Nucl. Fusion* 45.9 (Sept. 2005), pp. 1066–1077. DOI: [10.1088/0029-5515/45/9/006](https://doi.org/10.1088/0029-5515/45/9/006) (cit. on p. 13).

- [49] K. Kamiya, M. Bakhtiari, S. Kasai, et al. “High recycling steady H-mode regime in the JFT-2M tokamak”. In: *Plasma Phys. Control. Fusion* 46.5A (May 2004), A157–A163. DOI: [10.1088/0741-3335/46/5A/017](https://doi.org/10.1088/0741-3335/46/5A/017) (cit. on p. 14).
- [50] T. Happel, P. Manz, F. Ryter, et al. “Turbulence intermittency linked to the weakly coherent mode in ASDEX Upgrade I-mode plasmas”. In: *Nucl. Fusion* 56.6 (June 2016), p. 064004. DOI: [10.1088/0029-5515/56/6/064004](https://doi.org/10.1088/0029-5515/56/6/064004) (cit. on p. 14).
- [51] K.H. Burrell, T.H. Osborne, P.B. Snyder, et al. “Quiescent H-Mode Plasmas with Strong Edge Rotation in the Cocurrent Direction”. In: *Phys. Rev. Lett.* 102.15 (Apr. 2009), p. 155003. DOI: [10.1103/PhysRevLett.102.155003](https://doi.org/10.1103/PhysRevLett.102.155003) (cit. on p. 14).
- [52] M. Greenwald, R. Boivin, P. Bonoli, et al. “Studies of EDA H-mode in Alcator C-Mod”. In: *Plasma Phys. Control. Fusion* 42.5A (May 2000), A263–A269. DOI: [10.1088/0741-3335/42/5A/331](https://doi.org/10.1088/0741-3335/42/5A/331) (cit. on p. 14).
- [53] L. Gil, C. Silva, T. Happel, et al. “Stationary ELM-free H-mode in ASDEX Upgrade”. In: *Nucl. Fusion* 60.5 (May 2020), p. 054003. DOI: [10.1088/1741-4326/ab7d1b](https://doi.org/10.1088/1741-4326/ab7d1b) (cit. on p. 14).
- [54] H. Meyer, C. Angioni, C.G. Albert, et al. “Overview of physics studies on ASDEX Upgrade”. In: *Nucl. Fusion* 59.11 (Nov. 2019), p. 112014. DOI: [10.1088/1741-4326/ab18b8](https://doi.org/10.1088/1741-4326/ab18b8) (cit. on p. 18).
- [55] R. Neu, M. Balden, V. Bobkov, et al. “Plasma wall interaction and its implication in an all tungsten divertor tokamak”. In: *Plasma Phys. Control. Fusion* 49.12B (Dec. 2007), B59–B70. DOI: [10.1088/0741-3335/49/12B/S04](https://doi.org/10.1088/0741-3335/49/12B/S04) (cit. on p. 18).
- [56] S. Coda, M. Agostini, R. Albanese, et al. “Physics research on the TCV tokamak facility: from conventional to alternative scenarios and beyond”. In: *Nucl. Fusion* 59.11 (Nov. 2019), p. 112023. DOI: [10.1088/1741-4326/ab25cb](https://doi.org/10.1088/1741-4326/ab25cb) (cit. on p. 19).
- [57] R. Neu, A. Kallenbach, and H. Zohm. “ASDEX Upgrade”. In: *Magn. Fusion Energy*. Elsevier, June 2016, pp. 93–118. DOI: [10.1016/B978-0-08-100315-2.00005-2](https://doi.org/10.1016/B978-0-08-100315-2.00005-2) (cit. on p. 19).
- [58] A. Fasoli, H. Reimerdes, S. Alberti, et al. “TCV heating and divertor upgrades”. In: *Nucl. Fusion* 60.1 (Jan. 2020), p. 016019. DOI: [10.1088/1741-4326/ab4c56](https://doi.org/10.1088/1741-4326/ab4c56) (cit. on p. 19).
- [59] J. Stober, M. Reisner, C. Angioni, et al. “Exploring fusion-reactor physics with high-power electron cyclotron resonance heating on ASDEX Upgrade”. In: *Plasma Phys. Control. Fusion* 62.2 (Feb. 2020), p. 024012. DOI: [10.1088/1361-6587/ab512b](https://doi.org/10.1088/1361-6587/ab512b) (cit. on p. 21).
- [60] S. Gnesin, J. Decker, S. Coda, et al. “3rd harmonic electron cyclotron resonant heating absorption enhancement by 2nd harmonic heating at the same frequency in a tokamak”. In: *Plasma Phys. Control. Fusion* 54.3 (Mar. 2012), p. 035002. DOI: [10.1088/0741-3335/54/3/035002](https://doi.org/10.1088/0741-3335/54/3/035002) (cit. on p. 21).
- [61] T. Härtl, V. Rohde, and V. Mertens. “Status and perspectives of the ASDEX Upgrade gas inlet system”. In: *Fusion Eng. Des.* 96-97 (Oct. 2015), pp. 265–268. DOI: [10.1016/j.fusengdes.2015.06.166](https://doi.org/10.1016/j.fusengdes.2015.06.166) (cit. on pp. 22, 23).

- [62]P.T. Lang, A. Burckhart, M. Bernert, et al. “ELM pacing and high-density operation using pellet injection in the ASDEX Upgrade all-metal-wall tokamak”. In: *Nucl. Fusion* 54.8 (Aug. 2014), p. 083009. DOI: [10.1088/0029-5515/54/8/083009](https://doi.org/10.1088/0029-5515/54/8/083009) (cit. on pp. 23, 54, 55).
- [63]B. Ploeckl, C. Day, P. Lamalle, et al. “The enhanced pellet centrifuge launcher at ASDEX Upgrade: Advanced operation and application as technology test facility for ITER and DEMO”. In: *Fusion Eng. Des.* 96-97 (Oct. 2015), pp. 155–158. DOI: [10.1016/j.fusengdes.2015.01.006](https://doi.org/10.1016/j.fusengdes.2015.01.006) (cit. on p. 22).
- [64]L.R. Baylor, N. Commaux, T.C. Jernigan, et al. “Reduction of Edge-Localized Mode Intensity Using High-Repetition-Rate Pellet Injection in Tokamak H-Mode Plasmas”. In: *Phys. Rev. Lett.* 110.24 (June 2013), p. 245001. DOI: [10.1103/PhysRevLett.110.245001](https://doi.org/10.1103/PhysRevLett.110.245001) (cit. on p. 24).
- [65]A. Mlynek, G. Schramm, H. Eixenberger, et al. “Design of a digital multiradian phase detector and its application in fusion plasma interferometry”. In: *Rev. Sci. Instrum.* 81.3 (Mar. 2010), p. 033507. DOI: [10.1063/1.3340944](https://doi.org/10.1063/1.3340944) (cit. on p. 27).
- [66]S. Barry, C. Nieswand, and S.L. Prunty. “Far-infrared polarimetry on the tcv tokamak”. In: *Proc. 8th Int. Symp. Laser-aided Plasma Diagnostics*. 1997 (cit. on p. 28).
- [67]S. Barry. “The extension of the FIR interferometer of TCV to a polarimeter and measurements of the Faraday rotation caused by the poloidal magnetic field”. PhD thesis. EPFL, 1999 (cit. on p. 28).
- [68]B. Kurzan and H.D. Murmann. “Edge and core Thomson scattering systems and their calibration on the ASDEX Upgrade tokamak”. In: *Rev. Sci. Instrum.* 82.10 (Oct. 2011), p. 103501. DOI: [10.1063/1.3643771](https://doi.org/10.1063/1.3643771) (cit. on p. 28).
- [69]J. Hawke, Y. Andrebe, R. Bertizzolo, et al. “Improving spatial and spectral resolution of TCV Thomson scattering”. In: *J. Instrum.* 12.12 (Dec. 2017), pp. C12005–C12005. DOI: [10.1088/1748-0221/12/12/C12005](https://doi.org/10.1088/1748-0221/12/12/C12005) (cit. on pp. 28, 71).
- [70]S.S. Denk, R. Fischer, H.M. Smith, et al. “Analysis of electron cyclotron emission with extended electron cyclotron forward modeling”. In: *Plasma Phys. Control. Fusion* 60.10 (Oct. 2018), p. 105010. DOI: [10.1088/1361-6587/aadb2f](https://doi.org/10.1088/1361-6587/aadb2f) (cit. on p. 29).
- [71]M. Willensdorfer, G. Birkenmeier, R. Fischer, et al. “Characterization of the Li-BES at ASDEX Upgrade”. In: *Plasma Phys. Control. Fusion* 56.2 (Feb. 2014), p. 025008. DOI: [10.1088/0741-3335/56/2/025008](https://doi.org/10.1088/0741-3335/56/2/025008) (cit. on p. 30).
- [72]R. Fischer, C.J. Fuchs, B. Kurzan, W. Suttrop, and E. Wolfrum. “Integrated Data Analysis of Profile Diagnostics at ASDEX Upgrade”. In: *Fusion Sci. Technol.* 58.2 (Oct. 2010), pp. 675–684. DOI: [10.13182/FST10-110](https://doi.org/10.13182/FST10-110) (cit. on pp. 30, 85).
- [73]E. Viezzer, T. Pütterich, G.D. Conway, et al. “High-accuracy characterization of the edge radial electric field at ASDEX Upgrade”. In: *Nucl. Fusion* 53.5 (May 2013), p. 053005. DOI: [10.1088/0029-5515/53/5/053005](https://doi.org/10.1088/0029-5515/53/5/053005) (cit. on p. 31).
- [74]C.E. Rasmussen and H. Nickisch. “Gaussian processes for machine learning (GPML) toolbox”. In: *J. Mach. Learn. Res.* (2010) (cit. on p. 31).

- [75] M.A. Chilenski, M.J. Greenwald, A.E. Hubbard, et al. “Experimentally testing the dependence of momentum transport on second derivatives using Gaussian process regression”. In: *Nucl. Fusion* 57.12 (Dec. 2017), p. 126013. DOI: [10.1088/1741-4326/aa8387](https://doi.org/10.1088/1741-4326/aa8387) (cit. on p. 31).
- [76] F.M. Laggner, S. Keerl, J. Gnisen, et al. “Divertor, scrape-off layer and pedestal particle dynamics in the ELM cycle on ASDEX Upgrade”. In: *Plasma Phys. Control. Fusion* 60.2 (Feb. 2018), p. 025002. DOI: [10.1088/1361-6587/aa90bf](https://doi.org/10.1088/1361-6587/aa90bf) (cit. on p. 32).
- [77] A. Kallenbach, A. Carlson, G. Pautasso, et al. “Electric currents in the scrape-off layer in ASDEX Upgrade”. In: *J. Nucl. Mater.* 290-293 (Mar. 2001), pp. 639–643. DOI: [10.1016/S0022-3115\(00\)00445-1](https://doi.org/10.1016/S0022-3115(00)00445-1) (cit. on p. 33).
- [78] M. Knolker, T.E. Evans, A. Wingen, et al. “Observation of divertor currents during type-I ELMs on the DIII-D tokamak”. In: *Nucl. Mater. Energy* 18 (Jan. 2019), pp. 222–226. DOI: [10.1016/j.nme.2019.01.003](https://doi.org/10.1016/j.nme.2019.01.003) (cit. on p. 33).
- [79] R.A. Pitts, P. Andrew, X. Bonnin, et al. “Edge and divertor physics with reversed toroidal field in JET”. In: *J. Nucl. Mater.* 337-339 (Mar. 2005), pp. 146–153. DOI: [10.1016/j.jnucmat.2004.10.111](https://doi.org/10.1016/j.jnucmat.2004.10.111) (cit. on p. 34).
- [80] R. Maurizio. “Investigating Scrape-Off Layer transport in alternative divertor geometries on the TCV tokamak”. eng. PhD thesis. DOI: [10.5075/epfl-thesis-9893](https://doi.org/10.5075/epfl-thesis-9893) (cit. on p. 34).
- [81] B. Sieglin, M. Faitsch, A. Herrmann, et al. “Real time capable infrared thermography for ASDEX Upgrade”. In: *Rev. Sci. Instrum.* 86.11 (Nov. 2015), p. 113502. DOI: [10.1063/1.4935580](https://doi.org/10.1063/1.4935580) (cit. on p. 34).
- [82] G. Haas and H-S. Bosch. “In vessel pressure measurement in nuclear fusion experiments with asdex gauges”. In: *Vacuum* 51.1 (Sept. 1998), pp. 39–46. DOI: [10.1016/S0042-207X\(98\)00131-6](https://doi.org/10.1016/S0042-207X(98)00131-6) (cit. on p. 35).
- [83] M. Griener, O. Schmitz, K. Bald, et al. “Fast piezoelectric valve offering controlled gas injection in magnetically confined fusion plasmas for diagnostic and fuelling purposes”. In: *Rev. Sci. Instrum.* 88.3 (Mar. 2017), p. 033509. DOI: [10.1063/1.4978629](https://doi.org/10.1063/1.4978629) (cit. on p. 36).
- [84] M. Griener, E. Wolfrum, M. Cavedon, et al. “Helium line ratio spectroscopy for high spatiotemporal resolution plasma edge profile measurements at ASDEX Upgrade (invited)”. In: *Rev. Sci. Instrum.* 89.10 (Oct. 2018), p. 10D102. DOI: [10.1063/1.5034446](https://doi.org/10.1063/1.5034446) (cit. on pp. 36, 100).
- [85] T. Happel. “Doppler Reflectometry in the TJ-II Stellarator: Design of an Optimized Doppler Reflectometer and its Application to Turbulence and Radial Electric Field Studies”. THES. Universidad Carlos III de Madrid, 2010 (cit. on p. 37).
- [86] P. Hennequin, C. Honoré, A. Truc, et al. “Fluctuation spectra and velocity profile from Doppler backscattering on Tore Supra”. In: *Nucl. Fusion* 46.9 (Sept. 2006), S771–S779. DOI: [10.1088/0029-5515/46/9/S12](https://doi.org/10.1088/0029-5515/46/9/S12) (cit. on p. 37).
- [87] H. Zohm. *Magnetohydrodynamic Stability of Tokamaks*. New York: John Wiley & Sons, 2015 (cit. on pp. 37, 40, 42, 43, 64).

- [88]J.P. Freidberg. *Ideal MHD*. Cambridge: Cambridge University Press, 2014. DOI: [10.1017/CB09780511795046](https://doi.org/10.1017/CB09780511795046) (cit. on p. 37).
- [89]P. J. McCarthy. “Analytical solutions to the Grad–Shafranov equation for tokamak equilibrium with dissimilar source functions”. In: *Phys. Plasmas* 6.9 (Sept. 1999), pp. 3554–3560. DOI: [10.1063/1.873630](https://doi.org/10.1063/1.873630) (cit. on p. 38).
- [90]P.J. McCarthy. “Identification of edge-localized moments of the current density profile in a tokamak equilibrium from external magnetic measurements”. In: *Plasma Phys. Control. Fusion* 54.1 (Jan. 2012), p. 015010. DOI: [10.1088/0741-3335/54/1/015010](https://doi.org/10.1088/0741-3335/54/1/015010) (cit. on p. 38).
- [91]J.-M. Moret, B.P. Duval, H.B. Le, et al. “Tokamak equilibrium reconstruction code LIUQE and its real time implementation”. In: *Fusion Eng. Des.* 91 (Feb. 2015), pp. 1–15. DOI: [10.1016/j.fusengdes.2014.09.019](https://doi.org/10.1016/j.fusengdes.2014.09.019) (cit. on p. 39).
- [92]R. Fischer, A. Bock, M. Dunne, et al. “Coupling of the Flux Diffusion Equation with the Equilibrium Reconstruction at ASDEX Upgrade”. In: *Fusion Sci. Technol.* 69.2 (Apr. 2016), pp. 526–536. DOI: [10.13182/FST15-185](https://doi.org/10.13182/FST15-185) (cit. on pp. 39, 85).
- [93]G.T.A. Huysmans, J.P. Goedbloed, and W. Kerner. “Isoparametric Bicubic Hermite Elements for Solution of the Grad-Shafranov Equation”. In: *Int. J. Mod. Phys. C* 02.01 (Mar. 1991), pp. 371–376. DOI: [10.1142/S0129183191000512](https://doi.org/10.1142/S0129183191000512) (cit. on pp. 40, 48).
- [94]C. Mercier. “A necessary condition for hydromagnetic stability of plasma with axial symmetry”. In: *Nucl. Fusion* 1.1 (Sept. 1960), pp. 47–53. DOI: [10.1088/0029-5515/1/1/004](https://doi.org/10.1088/0029-5515/1/1/004) (cit. on p. 41).
- [95]R.L. Miller, M.S. Chu, J.M. Greene, Y.R. Lin-Liu, and R.E. Waltz. “Noncircular, finite aspect ratio, local equilibrium model”. In: *Phys. Plasmas* 5.4 (Apr. 1998), pp. 973–978. DOI: [10.1063/1.872666](https://doi.org/10.1063/1.872666) (cit. on p. 44).
- [96]C.E. Kessel. “Bootstrap current in a tokamak”. In: *Nucl. Fusion* 34.9 (Sept. 1994), pp. 1221–1238. DOI: [10.1088/0029-5515/34/9/I04](https://doi.org/10.1088/0029-5515/34/9/I04) (cit. on p. 44).
- [97]O. Sauter, C. Angioni, and Y.R. Lin-Liu. “Neoclassical conductivity and bootstrap current formulas for general axisymmetric equilibria and arbitrary collisionality regime”. In: *Phys. Plasmas* 6.7 (July 1999), pp. 2834–2839. DOI: [10.1063/1.873240](https://doi.org/10.1063/1.873240) (cit. on pp. 44, 47).
- [98]O. Sauter, C. Angioni, and Y.R. Lin-Liu. “Erratum: “Neoclassical conductivity and bootstrap current formulas for general axisymmetric equilibria and arbitrary collisionality regime” [Phys. Plasmas 6 , 2834 (1999)]”. In: *Phys. Plasmas* 9.12 (Dec. 2002), pp. 5140–5140. DOI: [10.1063/1.1517052](https://doi.org/10.1063/1.1517052) (cit. on pp. 44, 47).
- [99]P.B. Snyder, N. Aiba, M. Beurskens, et al. “Pedestal stability comparison and ITER pedestal prediction”. In: *Nucl. Fusion* 49.8 (Aug. 2009), p. 085035. DOI: [10.1088/0029-5515/49/8/085035](https://doi.org/10.1088/0029-5515/49/8/085035) (cit. on p. 45).
- [100]M.G. Dunne, L. Frassinetti, M.N.A. Beurskens, et al. “Global performance enhancements via pedestal optimisation on ASDEX Upgrade”. In: *Plasma Phys. Control. Fusion* 59.2 (Feb. 2017), p. 025010. DOI: [10.1088/1361-6587/59/2/025010](https://doi.org/10.1088/1361-6587/59/2/025010) (cit. on pp. 46, 47, 55, 77).

- [101] A.B. Mikhailovskii, G.T.A. Huysmans, W.O.K. Kerner, and S.E. Sharapov. “Optimization of computational MHD normal-mode analysis for Tokamaks”. In: *Plasma Phys. Reports* 23.10 (Oct. 1997), pp. 844–857 (cit. on p. 46).
- [102] M.G. Dunne, S. Potzel, F. Reimold, et al. “The role of the density profile in the ASDEX-Upgrade pedestal structure”. In: *Plasma Phys. Control. Fusion* 59.1 (Jan. 2017), p. 014017. DOI: [10.1088/0741-3335/59/1/014017](https://doi.org/10.1088/0741-3335/59/1/014017) (cit. on p. 47).
- [103] G.T.A. Huysmans and O. Czarny. “MHD stability in X-point geometry: simulation of ELMs”. In: *Nucl. Fusion* 47.7 (July 2007), pp. 659–666. DOI: [10.1088/0029-5515/47/7/016](https://doi.org/10.1088/0029-5515/47/7/016) (cit. on p. 48).
- [104] A. Cathey, M. Hoelzl, K. Lackner, et al. “Non-linear magnetohydrodynamic simulations of edge-localized-mode cycles in tokamak plasmas and their underlying triggering mechanism”. In: *Submitt. to Phys. Rev. Lett.* () (cit. on pp. 48, 92).
- [105] *JOREK web page* (cit. on p. 48).
- [106] G.F. Harrer, E. Wolfrum, M.G. Dunne, et al. “Parameter dependences of small edge localized modes (ELMs)”. In: *Nucl. Fusion* 58.11 (Nov. 2018), p. 112001. DOI: [10.1088/1741-4326/aad757](https://doi.org/10.1088/1741-4326/aad757) (cit. on pp. 49, 59).
- [107] B. Labit, T. Eich, G.F. Harrer, et al. “Dependence on plasma shape and plasma fueling for small edge-localized mode regimes in TCX and ASDEX Upgrade”. In: *Nucl. Fusion* 59.8 (Aug. 2019), p. 086020. DOI: [10.1088/1741-4326/ab2211](https://doi.org/10.1088/1741-4326/ab2211) (cit. on pp. 49, 69).
- [108] N. Leuthold, W. Suttrop, R. Fischer, et al. “Parameter dependence of ELM loss reduction by magnetic perturbations at low pedestal density and collisionality in ASDEX upgrade”. In: *Plasma Phys. Control. Fusion* 59.5 (May 2017), p. 055004. DOI: [10.1088/1361-6587/aa5f70](https://doi.org/10.1088/1361-6587/aa5f70) (cit. on p. 49).
- [109] B. Sieglin, M. Faitsch, T. Eich, A. Herrmann, and W. Suttrop. “Progress in extrapolating divertor heat fluxes towards large fusion devices”. In: *Phys. Scr.* T170.T170 (Dec. 2017), p. 014071. DOI: [10.1088/1402-4896/aa9670](https://doi.org/10.1088/1402-4896/aa9670) (cit. on pp. 50, 104).
- [110] B. Sieglin, T. Eich, M. Faitsch, et al. “Assessment of divertor heat load with and without external magnetic perturbation”. In: *Nucl. Fusion* 57.6 (June 2017), p. 066045. DOI: [10.1088/1741-4326/aa6c20](https://doi.org/10.1088/1741-4326/aa6c20) (cit. on p. 50).
- [111] M. Wischmeier. “High density operation for reactor-relevant power exhaust”. In: *J. Nucl. Mater.* 463 (Aug. 2015), pp. 22–29. DOI: [10.1016/j.jnucmat.2014.12.078](https://doi.org/10.1016/j.jnucmat.2014.12.078) (cit. on p. 50).
- [112] J. Stober, M. Maraschek, G.D. Conway, et al. “Type II ELMy H modes on ASDEX Upgrade with good confinement at high density”. In: *Nucl. Fusion* 41.9 (Sept. 2001), pp. 1123–1134. DOI: [10.1088/0029-5515/41/9/301](https://doi.org/10.1088/0029-5515/41/9/301) (cit. on pp. 50, 69).
- [113] G. Saibene, R. Sartori, A. Loarte, et al. “Improved performance of ELMy H-modes at high density by plasma shaping in JET”. In: *Plasma Phys. Control. Fusion* 44.9 (Sept. 2002), pp. 1769–1799. DOI: [10.1088/0741-3335/44/9/301](https://doi.org/10.1088/0741-3335/44/9/301) (cit. on p. 50).
- [114] A.C.C. Sips, G.D. Conway, R. Dux, et al. “Progress towards steady-state advanced scenarios in ASDEX Upgrade”. In: *Plasma Phys. Control. Fusion* 44.5A (May 2002), p. 311. DOI: [10.1088/0741-3335/44/5A/311](https://doi.org/10.1088/0741-3335/44/5A/311) (cit. on p. 50).

- [115]N. Oyama, Y. Sakamoto, A. Isayama, et al. “Energy loss for grassy ELMs and effects of plasma rotation on the ELM characteristics in JT-60U”. In: *Nucl. Fusion* 45.8 (Aug. 2005), pp. 871–881. DOI: [10.1088/0029-5515/45/8/014](https://doi.org/10.1088/0029-5515/45/8/014) (cit. on p. 50).
- [116]R. Maingi, A.E. Hubbard, H. Meyer, et al. “Comparison of small ELM characteristics and regimes in Alcator C-Mod, MAST and NSTX”. In: *Nucl. Fusion* 51.6 (June 2011), p. 063036. DOI: [10.1088/0029-5515/51/6/063036](https://doi.org/10.1088/0029-5515/51/6/063036) (cit. on p. 50).
- [117]S. Saarelma, S. Günter, L.D. Horton, and the ASDEX Upgrade Team. “MHD stability analysis of type II ELMs in ASDEX Upgrade”. In: *Nucl. Fusion* 43.4 (Apr. 2003), pp. 262–267. DOI: [10.1088/0029-5515/43/4/307](https://doi.org/10.1088/0029-5515/43/4/307) (cit. on p. 50).
- [118]S. Saarelma, A. Alfier, M.N.A. Beurskens, et al. “MHD stability analysis of small ELM regimes in JET”. In: *Plasma Phys. Control. Fusion* 51.3 (Mar. 2009), p. 035001. DOI: [10.1088/0741-3335/51/3/035001](https://doi.org/10.1088/0741-3335/51/3/035001) (cit. on pp. 50, 62).
- [119]D. Dickinson, C.M. Roach, J.M. Skipp, and H.R. Wilson. “Structure of micro-instabilities in tokamak plasmas: Stiff transport or plasma eruptions?” In: *Phys. Plasmas* 21.1 (Jan. 2014), p. 010702. DOI: [10.1063/1.4861628](https://doi.org/10.1063/1.4861628) (cit. on p. 50).
- [120]A. Bokshi, D. Dickinson, C. M. Roach, and H. R. Wilson. “The response of toroidal drift modes to profile evolution: a model for small-ELMs in tokamak plasmas?” In: *Plasma Phys. Control. Fusion* 58.7 (July 2016), p. 075011. DOI: [10.1088/0741-3335/58/7/075011](https://doi.org/10.1088/0741-3335/58/7/075011) (cit. on p. 50).
- [121]H. Meyer, T. Eich, M. Beurskens, et al. “Overview of progress in European medium sized tokamaks towards an integrated plasma-edge/wall solution”. In: *Nucl. Fusion* 57.10 (Oct. 2017), p. 102014. DOI: [10.1088/1741-4326/aa6084](https://doi.org/10.1088/1741-4326/aa6084) (cit. on p. 50).
- [122]B. Kurzan, H. Murmann, and H. Salzmann. “Improvements in the evaluation of Thomson scattering data on ASDEX upgrade”. In: *Rev. Sci. Instrum.* 72.1 (Jan. 2001), pp. 1111–1114. DOI: [10.1063/1.1321747](https://doi.org/10.1063/1.1321747) (cit. on p. 51).
- [123]M. Cavedon, T. Pütterich, E. Viezzer, et al. “A fast edge charge exchange recombination spectroscopy system at the ASDEX Upgrade tokamak”. In: *Rev. Sci. Instrum.* 88.4 (Apr. 2017), p. 043103. DOI: [10.1063/1.4979801](https://doi.org/10.1063/1.4979801) (cit. on pp. 51, 53).
- [124]R.M. McDermott, A. Lebschy, B. Geiger, et al. “Extensions to the charge exchange recombination spectroscopy diagnostic suite at ASDEX Upgrade”. In: *Rev. Sci. Instrum.* 88.7 (July 2017), p. 073508. DOI: [10.1063/1.4993131](https://doi.org/10.1063/1.4993131) (cit. on p. 51).
- [125]A. Kallenbach. “Overview of ASDEX Upgrade results”. In: *Nucl. Fusion* 57.10 (Oct. 2017), p. 102015. DOI: [10.1088/1741-4326/aa64f6](https://doi.org/10.1088/1741-4326/aa64f6) (cit. on p. 51).
- [126]P.T. Lang, T.C. Blanken, M. Dunne, et al. “Feedback controlled, reactor relevant, high-density, high-confinement scenarios at ASDEX Upgrade”. In: *Nucl. Fusion* 58.3 (Mar. 2018), p. 036001. DOI: [10.1088/1741-4326/aaa339](https://doi.org/10.1088/1741-4326/aaa339) (cit. on p. 51).
- [127]R.J. Groebner and T.H. Osborne. “Scaling studies of the high mode pedestal”. In: *Phys. Plasmas* 5.5 (May 1998), pp. 1800–1806. DOI: [10.1063/1.872849](https://doi.org/10.1063/1.872849) (cit. on p. 52).
- [128]D. Carralero, S. Artene, M. Bernert, et al. “On the role of filaments in perpendicular heat transport at the scrape-off layer”. In: *Nucl. Fusion* 58.9 (Sept. 2018), p. 096015. DOI: [10.1088/1741-4326/aacb04](https://doi.org/10.1088/1741-4326/aacb04) (cit. on p. 53).

- [129]H.J. Sun, E. Wolfrum, T. Eich, et al. “Study of near scrape-off layer (SOL) temperature and density gradient lengths with Thomson scattering”. In: *Plasma Phys. Control. Fusion* 57.12 (Dec. 2015), p. 125011. DOI: [10.1088/0741-3335/57/12/125011](https://doi.org/10.1088/0741-3335/57/12/125011) (cit. on p. 53).
- [130]A. Kirk, A. Herrmann, B. Ayed, et al. “Comparison of the filament behaviour observed during type I ELMs in ASDEX upgrade and MAST”. In: *J. Phys. Conf. Ser.* 123.1 (July 2008), p. 012012. DOI: [10.1088/1742-6596/123/1/012012](https://doi.org/10.1088/1742-6596/123/1/012012) (cit. on p. 54).
- [131]P. Hennequin, F. Laggner, F. Mink, et al. “Inter-ELM Fluctuations and Flows and their evolution when approaching the density limit in the ASDEX Upgrade tokamak”. In: *44th EPS Conf. Plasma Physics, EPS 2017 P1.167* (2017) (cit. on p. 55).
- [132]M.G. Dunne. “Impact of impurity seeding and divertor conditions on transitions, pedestal structure and ELMs”. In: *Nucl. Fusion* 57.2 (Feb. 2017), p. 025002. DOI: [10.1088/0029-5515/57/2/025002](https://doi.org/10.1088/0029-5515/57/2/025002) (cit. on pp. 62, 73).
- [133]M.G. Dunne, S. Rathgeber, A. Burckhart, et al. “Impact of T e and n e on edge current density profiles in ELM mitigated regimes on ASDEX Upgrade”. In: *Nucl. Fusion* 55.1 (Jan. 2015), p. 013013. DOI: [10.1088/0029-5515/55/1/013013](https://doi.org/10.1088/0029-5515/55/1/013013) (cit. on p. 62).
- [134]T. Eich, R.J. Goldston, A. Kallenbach, B. Sieglin, and H.J. Sun. “Correlation of the tokamak H-mode density limit with ballooning stability at the separatrix”. In: *Nucl. Fusion* 58.3 (Mar. 2018), p. 034001. DOI: [10.1088/1741-4326/aaa340](https://doi.org/10.1088/1741-4326/aaa340) (cit. on p. 63).
- [135]P.J. Mc Carthy. “Practical expressions for local magnetic shear, normal and geodesic curvatures in an axisymmetric plasma equilibrium of arbitrary cross-section”. In: *Plasma Phys. Control. Fusion* 55.8 (Aug. 2013), p. 085011. DOI: [10.1088/0741-3335/55/8/085011](https://doi.org/10.1088/0741-3335/55/8/085011) (cit. on pp. 64, 81, 89).
- [136]D. Dickinson, S. Saarelma, R. Scannell, et al. “Towards the construction of a model to describe the inter-ELM evolution of the pedestal on MAST”. In: *Plasma Phys. Control. Fusion* 53.11 (Nov. 2011), p. 115010. DOI: [10.1088/0741-3335/53/11/115010](https://doi.org/10.1088/0741-3335/53/11/115010). arXiv: [1107.3109](https://arxiv.org/abs/1107.3109) (cit. on p. 64).
- [137]D. Dickinson, C.M. Roach, S. Saarelma, et al. “Kinetic Instabilities that Limit beta in the Edge of a Tokamak Plasma: A Picture of an H-Mode Pedestal”. In: *Phys. Rev. Lett.* 108.13 (Mar. 2012), p. 135002. DOI: [10.1103/PhysRevLett.108.135002](https://doi.org/10.1103/PhysRevLett.108.135002) (cit. on p. 64).
- [138]B.D. Scott. “Three-dimensional computation of drift Alfvén turbulence”. In: *Plasma Phys. Control. Fusion* 39.10 (Oct. 1997), pp. 1635–1668. DOI: [10.1088/0741-3335/39/10/010](https://doi.org/10.1088/0741-3335/39/10/010) (cit. on p. 64).
- [139]A.C.C. Sips, J. Schweinzer, T.C. Luce, et al. “Assessment of the baseline scenario at q 95 3 for ITER”. In: *Nucl. Fusion* 58.12 (Dec. 2018), p. 126010. DOI: [10.1088/1741-4326/aade57](https://doi.org/10.1088/1741-4326/aade57) (cit. on p. 69).
- [140]R.J. Groebner, D.R. Baker, K.H. Burrell, et al. “Progress in quantifying the edge physics of the H mode regime in DIII-D”. In: *Nucl. Fusion* 41.12 (Dec. 2001), pp. 1789–1802. DOI: [10.1088/0029-5515/41/12/306](https://doi.org/10.1088/0029-5515/41/12/306) (cit. on pp. 71, 77).

- [141]U.A. Sheikh, M. Dunne, L. Frassinetti, et al. “Pedestal structure and energy confinement studies on TCV”. In: *Plasma Phys. Control. Fusion* 61.1 (Jan. 2019), p. 014002. DOI: [10.1088/1361-6587/aae7bd](https://doi.org/10.1088/1361-6587/aae7bd) (cit. on pp. 71–73).
- [142]L. Frassinetti, M.G. Dunne, U. Sheikh, et al. “Role of the pedestal position on the pedestal performance in AUG, JET-ILW and TCV and implications for ITER”. In: *Nucl. Fusion* 59.7 (July 2019), p. 076038. DOI: [10.1088/1741-4326/ab1eb9](https://doi.org/10.1088/1741-4326/ab1eb9) (cit. on p. 71).
- [143]H. Reimerdes, S. Alberti, P. Blanchard, et al. “TCV divertor upgrade for alternative magnetic configurations”. In: *Nucl. Mater. Energy* 12 (Aug. 2017), pp. 1106–1111. DOI: [10.1016/j.nme.2017.02.013](https://doi.org/10.1016/j.nme.2017.02.013) (cit. on p. 73).
- [144]Y. Kamada, T. Oikawa, L. Lao, et al. “Disappearance of giant ELMs and appearance of minute grassy ELMs in JT-60U high-triangularity discharges”. In: *Plasma Phys. Control. Fusion* 42.5A (May 2000), A247–A253. DOI: [10.1088/0741-3335/42/5A/329](https://doi.org/10.1088/0741-3335/42/5A/329) (cit. on p. 73).
- [145]J. Stober, O. Gruber, A. Kallenbach, et al. “Effects of triangularity on confinement, density limit and profile stiffness of H-modes on ASDEX upgrade”. In: *Plasma Phys. Control. Fusion* 42.5A (May 2000), A211–A216. DOI: [10.1088/0741-3335/42/5A/324](https://doi.org/10.1088/0741-3335/42/5A/324) (cit. on p. 73).
- [146]R. Maurizio, S. Elmore, N. Fedorczak, et al. “Divertor power load studies for attached L-mode single-null plasmas in TCV”. In: *Nucl. Fusion* 58.1 (Jan. 2018), p. 016052. DOI: [10.1088/1741-4326/aa986b](https://doi.org/10.1088/1741-4326/aa986b) (cit. on p. 76).
- [147]A. Merle, O. Sauter, and S.Yu Medvedev. “Pedestal properties of H-modes with negative triangularity using the EPED-CH model”. In: *Plasma Phys. Control. Fusion* 59.10 (Oct. 2017), p. 104001. DOI: [10.1088/1361-6587/aa7ac0](https://doi.org/10.1088/1361-6587/aa7ac0) (cit. on p. 76).
- [148]A. Kallenbach, N. Asakura, A. Kirk, et al. “Multi-machine comparisons of H-mode separatrix densities and edge profile behaviour in the ITPA SOL and Divertor Physics Topical Group”. In: *J. Nucl. Mater.* 337-339.1-3 SPEC. ISS. (Mar. 2005), pp. 381–385. DOI: [10.1016/j.jnucmat.2004.10.099](https://doi.org/10.1016/j.jnucmat.2004.10.099) (cit. on p. 77).
- [149]P.C. Stangeby. “The Plasma Boundary of Magnetic Fusion Devices”. In: *Bristol Inst. Phys. Publ.* (2000) (cit. on p. 77).
- [150]H. Lütjens, A. Bondeson, and O. Sauter. “The CHEASE code for toroidal MHD equilibria”. In: *Comput. Phys. Commun.* 97.3 (Sept. 1996), pp. 219–260. DOI: [10.1016/0010-4655\(96\)00046-X](https://doi.org/10.1016/0010-4655(96)00046-X) (cit. on p. 78).
- [151]F.D. Halpern, S. Jolliet, J. Loizu, A. Masetto, and P. Ricci. “Ideal ballooning modes in the tokamak scrape-off layer”. In: *Phys. Plasmas* 20.5 (May 2013), p. 052306. DOI: [10.1063/1.4807333](https://doi.org/10.1063/1.4807333) (cit. on p. 78).
- [152]B.N. Rogers, J.F. Drake, and A. Zeiler. “Phase Space of Tokamak Edge Turbulence, the L-H Transition, and the Formation of the Edge Pedestal”. In: *Phys. Rev. Lett.* 81.20 (Nov. 1998), pp. 4396–4399. DOI: [10.1103/PhysRevLett.81.4396](https://doi.org/10.1103/PhysRevLett.81.4396) (cit. on p. 78).
- [153]A.S. Kukushkin, H.D. Pacher, V. Kotov, G.W. Pacher, and D. Reiter. “Finalizing the ITER divertor design: The key role of SOLPS modeling”. In: *Fusion Eng. Des.* 86.12 (Dec. 2011), pp. 2865–2873. DOI: [10.1016/j.fusengdes.2011.06.009](https://doi.org/10.1016/j.fusengdes.2011.06.009) (cit. on p. 78).

- [154]R.L. Miller, F.L. Waelbroeck, A.B. Hassam, and R.E. Waltz. “Stabilization of ballooning modes with sheared toroidal rotation”. In: *Phys. Plasmas* 2.10 (Oct. 1995), pp. 3676–3684. DOI: [10.1063/1.871067](https://doi.org/10.1063/1.871067) (cit. on p. 83).
- [155]R.M.O. Galvão and J. Rem. “Application of the suydam method to the ballooning stability problem”. In: *Comput. Phys. Commun.* 22.4 (May 1981), pp. 399–402. DOI: [10.1016/0010-4655\(81\)90136-3](https://doi.org/10.1016/0010-4655(81)90136-3) (cit. on p. 86).
- [156]F. Orain, M. Bécoulet, G.T.A. Huijsmans, et al. “Resistive Reduced MHD Modeling of Multi-Edge-Localized-Mode Cycles in Tokamak X -Point Plasmas”. In: *Phys. Rev. Lett.* 114.3 (Jan. 2015), p. 035001. DOI: [10.1103/PhysRevLett.114.035001](https://doi.org/10.1103/PhysRevLett.114.035001) (cit. on p. 92).
- [157]K.H. Burrell, T.N. Carlstrom, E.J. Doyle, et al. “Physics of the L-mode to H-mode transition in tokamaks”. In: *Plasma Phys. Control. Fusion* 34.13 (Dec. 1992), pp. 1859–1869. DOI: [10.1088/0741-3335/34/13/014](https://doi.org/10.1088/0741-3335/34/13/014) (cit. on p. 94).
- [158]F. Wagner. “A quarter-century of H-mode studies”. In: *Plasma Phys. Control. Fusion* 49.12B (Dec. 2007), B1–B33. DOI: [10.1088/0741-3335/49/12B/S01](https://doi.org/10.1088/0741-3335/49/12B/S01) (cit. on p. 94).
- [159]M. Cavedon, G. Birkenmeier, T. Pütterich, et al. “Connecting the global H-mode power threshold to the local radial electric field at ASDEX Upgrade”. In: *Nucl. Fusion* (Apr. 2020). DOI: [10.1088/1741-4326/ab8777](https://doi.org/10.1088/1741-4326/ab8777) (cit. on p. 94).
- [160]C. Albert, R. Hofmeister, and RedMod Team. *proFit: Probabilistic response model fitting with interactive tools*. 2019. DOI: [10.5281/zenodo.3580488](https://doi.org/10.5281/zenodo.3580488) (cit. on p. 94).
- [161]T. Eich, B. Sieglin, A. Scarabosio, et al. “Inter-ELM Power Decay Length for JET and ASDEX Upgrade: Measurement and Comparison with Heuristic Drift-Based Model”. In: *Phys. Rev. Lett.* 107.21 (Nov. 2011), p. 215001. DOI: [10.1103/PhysRevLett.107.215001](https://doi.org/10.1103/PhysRevLett.107.215001) (cit. on p. 105).
- [162]M. Faitsch, G.F. Harrer, T. Eich, et al. “Power exhaust in small ELM regimes at high separatrix density”. In: *Plasma Phys. Control. Fusion, to be Submitt.* (2020), p. 85748 (cit. on p. 105).
- [163]A. Kallenbach, H.J. Sun, T. Eich, et al. “Parameter dependences of the separatrix density in nitrogen seeded ASDEX Upgrade H-mode discharges”. In: *Plasma Phys. Control. Fusion* 60.4 (Apr. 2018), p. 045006. DOI: [10.1088/1361-6587/aaab21](https://doi.org/10.1088/1361-6587/aaab21) (cit. on p. 108).



# Declaration

I declare that this thesis has been composed solely by myself and that it has not been submitted, in whole or in part, in any previous application for a degree. Except where stated otherwise by reference or acknowledgement, the work presented is entirely my own.

*Wien, June 22, 2020*



---

Georg Friedrich Harrer

